THE ROLE OF STRESS CONCENTRATIONS IN STRUCTURAL FATIGUE

By

John H. Crews, Jr.

Dissertation submitted to the Graduate Faculty of the

Virginia Polytechnic Institute

in partial fulfillment of the requirements for the degree of

DOCTOR OF PHILOSOPHY

in

Engineering Mechanics

May 1969

THE ROLE OF STRESS CONCENTRATIONS IN STRUCTURAL FATIGUE

By

John H. Crews, Jr.

ABSTRACT

This dissertation deals with an analysis of fatigue behavior at stress-concentration sites under cyclic loading. Specifically, the study treats sheet specimens containing a central hole under remote uniaxial cyclic loading. This investigation was conducted in three phases: an analysis of local cyclic stress-strain conditions at the stress-concentration site, an investigation of fatigue crack initiation, and a study of the initial stage of crack propagation for cracks growing from the stress-concentration site.

Because fatigue cracks in structures originate at stress concentrations, rational methods for estimating crack initiation must be based upon cyclic stress-strain conditions at typical stress-concentration sites. For the specimen configuration considered in the present study, this point of maximum stress and strain was on the boundary of the hole and consequently was in a uniaxial stress state. Cyclic stress and strain were estimated for this point by cycling uniaxial coupons between calculated limits for the local stress and strain. The adequacy of this "analytical-control" procedure was demonstrated by a comparison of calculated results with experimental results obtained on a companion specimen. Comparisons were made for constant-amplitude, two-level, and random loading.

The first level of the two-level loading was designed to produce residual stresses that altered local fatigue damage accumulation for the second loading level. This nominal stress interaction was typical of those experienced in structures. To obtain estimates of crack initiation that accounted for this stress interaction, the analytical-control tests from the first phase were continued until the uniaxial coupons failed by fatigue. The accuracy of this procedure was illustrated by comparison of estimated and observed crack-initiation periods.

To complete this study of the role of stress concentrations in fatigue, the initial stage of crack propagation from a stress-concentration site was investigated. Short cracks emanating from stress-concentration zones are influenced by the local stress field corresponding to the stress concentration. Through the use of a Westergaard stress function for concentrated loads on a crack surface together with a boundary-collocation technique, a general procedure was developed for calculating stress-intensity factors for cracks growing from a hole in a sheet specimen. Stress-intensity factors were used together with a "master curve" characterizing crack growth for the sheet material to calculate crack-growth curves for cracks growing from the hole. These calculations were made for local stress fields corresponding to the constant-amplitude and two-level loading of the first two phases of the study. The crack-initiation tests of the second phase were continued to obtain experimental crack propagation results. Reasonable correlation was found between the calculated and experimental crack-growth curves.

The generally close correlation between calculated and observed results throughout this study demonstrated the utility of local stress analyses in the prediction of fatigue behavior for structural components containing stress concentrations. The procedures used herein are expected to be generally applicable for fatigue analyses involving more complicated configurations and loading than those considered in this investigation.

THE ROLE OF STRESS CONCENTRATIONS IN STRUCTURAL FATIGUE

by

John H. Crews, Jr.

Thesis submitted to the Graduate Faculty of the

Virginia Polytechnic Institute

in partial fulfillment of the requirements for the degree of

DOCTOR OF PHILOSOPHY

in

Engineering Mechanics

APPROVED:

H. F. Brinson

Chairman, Prof. H. F. Brinson

Daniel Frederick

Prof. D. Frederick

Robert A. Heller

Prof. R. A. Heller

Jack L. Lytton

Prof. J. L. Lytton

R. P. McNitt

Prof. R. P. McNitt

C. W. Smith

Prof. C. W. Smith

May 1969

Blacksburg, Virginia

TABLE OF CONTENTS

ACKNOWLEDGMENTS

The author wishes to acknowledge that research for this dissertation was conducted at Langley Research Center, National Aeronautics and Space Administration, as part of the author's work assignment. The author is grateful to Dr. H. F. Brinson for his helpful criticisms and suggestions. The author also wishes to express his appreciation to Nancy H. White for programing the numerical analyses, Joe C. Woolsey for assistance in the experimental phase of this study, and Richard L. Shearer for figure preparation. Finally, the author wishes to thank his wife, Ellen, for her assistance and encouragement.

LIST OF TABLES AND FIGURES

LIST OF SYMBOLS

A	material constant, in.
A_n, B_n	arbitrary constants
E	Young's modulus, ksi
E_s	secant modulus corresponding to local stress, ksi
E_{s_i}	secant modulus corresponding to ΔS_i, ksi
F	square root of ratio of elastic strain range to total strain range
$F(\tau)$	strain function
K_f	fatigue notch factor, the ratio of fatigue limits for unnotched and notched specimens for same R
K_N	Neuber stress-concentration factor
K_T	theoretical elastic stress-concentration factor
K_ϵ, K_σ	strain- and stress-concentration factors
L	crack length, in.
M	limit for index
N	number of cycles
$N(\tau)$	leading function
N_{cp}	number of cycles during crack propagation phase
N_f	total fatigue life, cycles
N_i	fatigue life for ith stress level, cycles
N_o	number of cycles during crack-initiation phase
P	concentrated force, lb
R	ratio of minimum to maximum stress
S	net nominal stress, ksi

S_2	amplitude of nominal stress, ksi
ΔS	range for nominal stress, ksi
ΔS_i	range of nominal stress for ith load excursion, ksi
W	width of notched specimen, in.
$Z_1(z)$	Westergaard stress function
a	crack length, in.
Δa	increment of crack length, in.
b	dimension locating concentrated force on crack boundary, in.
Δb	distance between concentrated forces, in.
e	nominal strain
Δe	range of nominal strain
i	index
k	stress-intensity factor, ksi $\sqrt{\text{in.}}$
n	index
n_i	number of cycles applied at ith stress level
r	radial coordinate, in.
t	thickness, in.
w	flank angle of notch, rad
x,y	Cartesian coordinates, in.
z	complex number
$\bar{z}$	complex conjugate of z
$\Phi(z), \Psi(z), \Omega(z), \phi(z), \psi(z)$	Muskhelishvili stress functions
ϵ	local strain
$\Delta\epsilon$	range of local strain

$\Delta\epsilon_e, \Delta\epsilon_t$	elastic strain range, total strain range
$\Delta\epsilon_i$	range of local strain corresponding to ΔS_i
θ	cylindrical coordinate, rad
ρ	notch root radius, in.
σ	local stress, ksi
$\sigma(x)$	stress distribution along x-axis, ksi
σ_g	gross nominal stress, ksi
$\sigma_{rr}, \sigma_{rr_o}$	normal stress and elastic normal stress in r-direction, ksi
$\sigma_{\theta\theta}, \sigma_{\theta\theta_o}$	normal stress and elastic normal stress in θ-direction, ksi
$\Delta\sigma, \Delta\sigma_o$	range of local stress and range of elastic local stress, ksi
$\Delta\sigma_i$	range of local stress corresponding to ΔS_i, ksi
τ	local shear stress, ksi
τ_N	nominal shear stress, ksi

1. INTRODUCTION

1.1 General

The importance of fatigue considerations in the design and use of structures has been well recognized for many years. However, in spite of intense efforts to develop analytical methods for predicting structural fatigue, most fatigue evaluations must be based upon ad hoc tests of prototype structures. These tests are usually time consuming and may result in expensive design changes. Analytical predictions of structural fatigue would be preferred at an early design stage of a new structure.

One of the primary deterrents to the analysis of structural fatigue has been the problem of local stress analysis. Virtually all structures contain fasteners, fillets, or other such abrupt changes in configuration that act as stress raisers during service loading. The material at each of these stress-concentration sites is highly stressed (often into the plastic range) during the cyclic loading and, consequently, these sites become fatigue critical areas. Fatigue cracks originate at and propagate from these critical zones. To predict the initiation of fatigue cracks, stress-strain conditions within these zones must be determined. Moreover, during the early stages of crack propagation, a crack is under the influence of the local stress field. Consequently, the problem of local stress analysis may also complicate the analysis of fatigue crack propagation.

1.2 Specific Objectives

The present study was undertaken to investigate typical effects of stress concentrations on the fatigue behavior of sheet specimens. This study was conducted in three phases: a study of local cyclic stress-strain conditions at the stress-concentration site, an investigation of crack initiation, and an analysis of the initial stage of crack propagation at this site.

Because fatigue cracks originate at the most highly stressed zone of a stress-concentration site, attention was restricted to this zone during the first phase of the study. As a further simplification, thin specimens containing a central hole with inplane loading were considered. For this type of specimen, the vicinity of the stress raiser is in a state of plane stress and the fatigue critical zone on the stress-free boundary of the hole is under simple uniaxial stress. Conditions at this critical point were referred to as "local" conditions. As a result of this uniaxial stress state, local conditions were investigated by simulating local cyclic stress-strain behavior in unnotched uniaxial specimens. This simulation was performed by cycling the unnotched specimens between prescribed local elastoplastic stress-strain limits. An equation relating local stress- and strain-concentration factors for nonlinear material behavior was used to calculate these limits. For an evaluation of this "analytical-control" procedure, local cyclic stress-strain conditions were also determined experimentally using a "companion-specimen" method. The calculated and experimental results were compared for constant and variable-amplitude fatigue loading.

To demonstrate the importance of analyzing fatigue crack initiation from a local cyclic stress-strain approach, loading levels and sequences were selected to produce stress interactions. These stress interactions were caused by residual stresses and damage acceleration at the stress-concentration site and were typical of those found in service. Fatigue crack-initiation periods for the notched specimens were estimated by continuing the analytical-control tests from the first phase until cracks appeared in the unnotched specimens. The adequacy of this prediction method was assessed by comparing estimated results and observed crack-initiation periods in notched specimens.

The effect of the stress concentration on fatigue exists beyond the initiation of a fatigue crack at the stress-concentration site. The high stresses in the immediate vicinity of a stress raiser increase the crack propagation rates for small cracks originating at the critical site. In addition, for variable-amplitude loading involving local plasticity, residual stresses may exist in the vicinity of the stress concentration that alter crack-growth behavior. Consequently, a third phase of this study investigated the effects of stress raisers during the initial stage of crack propagation.

Through the use of a Westergaard stress function for concentrated loads on a free crack together with a boundary-collocation procedure, a general procedure was developed for calculating stress-intensity factors for cracks growing from a central hole in sheet specimens. Stress-intensity factors for cracks propagating through residual stress fields were determined with the aid of elastic and approximate elastoplastic analyses of stresses near the circular hole. These stress

intensity factors were used together with a "master curve," characterizing the crack-growth behavior for the specimen material, to calculate crack-growth curves for several types of constant and variable-amplitude loading considered in the first two phases of this study. The accuracy of the estimates of stress-interaction effects on initial crack propagation behavior was determined by comparing estimated crack-growth curves with test results.

The correlation between calculated and experimental results demonstrated in this study illustrates the utility of local stress analyses for the prediction of fatigue lives for structural components containing stress concentrations. The procedures used in this study to estimate fatigue behavior are expected to be generally applicable in fatigue analyses involving more complicated configurations and loading sequences than those considered in this investigation.

2. LITERATURE REVIEW

2.1 General

Fatigue failures in machine and structural components characteristically originate at stress concentrations such as bolt holes, fillets, or other abrupt changes in configuration. Because of this localized nature of fatigue crack initiation, rational methods for predicting fatigue must be based upon analyses of local stress and strain at the stress-concentration sites. In weight-critical structures, because of the high design stresses, local conditions often extend into the plastic range. This literature review will briefly survey the problem area of elastoplastic analysis of cyclic stress-strain conditions at stress concentrations. In addition, methods for predicting fatigue crack-initiation periods based on local stress are reviewed in the second part of this literature survey. To complete the review of the effects of stress concentrations on fatigue, the third part of this review deals with the initial stage of crack propagation for cracks growing from stress-concentration sites.

2.2 Local Cyclic Stress-Strain Studies

The analysis of local elastoplastic stress-strain behavior at a stress-concentration site is quite complicated even for monotonic loading. For cyclic loading, the local stress and strain depend also upon the loading sequence which severely complicates theoretical analyses. Furthermore, many materials exhibit stress-strain properties that are altered by cycling. As a result of these complicating factors,

numerical or approximate techniques have been used to analyze local conditions for cyclic loading.

2.2.1 Numerical Analyses

Several numerical analyses have been conducted for plane specimens under cyclic loading. Denke [1] used a finite-element approach to obtain a numerical solution for the elastoplastic stress distribution near a central hole in a plate during one cycle of loading. Material behavior was assumed to be elastoplastic during loading and entirely elastic during unloading. From this solution residual stress distributions were determined and used to estimate fatigue behavior.

Ibrahim, McCallion, and Dudley [2] also investigated the elastoplastic deformation around a circular hole under one cycle of loading. A finite-difference approach together with a relaxation method were used to obtain a plane-strain solution. Reasonable correlation was shown between this solution and test results on a sheet containing a central hole in plane stress. The elastoplastic analysis was conducted for both loading and unloading to account for the reversed yielding associated with unloading.

Isakson, Armen, and Pifko [3] applied a finite-element analysis throughout three cycles of reversed loading of an edge-notched sheet specimen. Specimen configuration, material behavior, and loading levels were identical to those used by Crews [4] in an experimental study of local behavior and a close correlation was found between numerical and experimental results.

A finite-element technique developed by Jordan [5] was applied by Mowbray and Slot [6] to investigate stress and strain redistribution

in notched specimens during cyclic loading. Mowbray and Slot selected the specimen dimensions, material, and loading used by Blatherwick and Olson [7] in an experimental analysis of strain distribution. Cyclic stress-strain diagrams were used as effective stress-strain curves to determine stress and strain redistributions resulting from the cyclic strain softening exhibited by the specimen material. The numerical results were found to correlate well with measured strains reported by Blatherwick and Olson.

2.2.2 Stress- and Strain-Concentration Studies

From a fatigue point of view, attention can be restricted to the most highly stressed zone of a stress-concentration site without seriously affecting the usefulness of stress-concentration studies. This zone becomes the fatigue critical site of the specimen for cyclic loading. If fatigue cracks develop, they will originate in this zone. In this study attention was consequently limited to this most critical location. Conditions at this site were referred to as "local" conditions. Furthermore, for the case of plane stress considered in this investigation, the critical zone reduces to a point and the behavior at this location can be conveniently described in terms of stress- and strain-concentration factors.

In the second part of this literature survey several fatigue prediction methods based on the use of stress- or strain-concentration factors are reviewed. All of these methods are based upon either the modified Stowell [8] or the Neuber [9] equations for elastoplastic stress- and strain-concentration factors.

Stowell investigated the problem of elastoplastic behavior of a sheet with a circular hole and with uniform loading at infinity. To account for local plasticity, Stowell introduced the ratio E_s/E_∞ into the elastic solution where E_s is the secant modulus at the critical location and E_∞ is the secant modulus corresponding to the uniform stress remote from the hole. This formulation led to the stress-concentration factor for elastoplastic behavior of

$$K_\sigma = 1 + 2\frac{E_s}{E_\infty} \tag{1}$$

The corresponding strain-concentration factor was found to be

$$K_\epsilon = \left[1 + 2\frac{E_s}{E_\infty}\right]\frac{E_\infty}{E_s} \tag{2}$$

Stowell compared his results with the experimental data obtained by Griffith [10] for wide 2024-T3 aluminum alloy sheets also with a circular hole under remote uniform tension. Excellent correlation was found for stress-concentration factors. However, theoretical strain-concentration factors were noticeably smaller than the experimental results.

Hardrath and Ohman [11] generalized the stress-concentration factor equation (1) by presenting the following expression in terms of the elastic stress-concentration factor K_T

$$K_\sigma = \frac{\sigma}{S} = 1 + (K_T - 1)\frac{E_s}{E} \tag{3}$$

where σ is the maximum local stress and S is the nominal stress at a remote location. This equation was used to calculate stress-concentration factors for sheet specimens containing notches and fillets, and results were compared with experimental data for 2024-T3 aluminum alloy. In addition, Hardrath and Ohman compared calculated results with experimental stress-concentration factors determined by Box [12]. In general, equation (3) correlated very closely with experimental results.

Crews [13] and Crews and Hardrath [14] considered the application of the generalized Stowell equation (3) for cyclic loading conditions. The nominal stress sequence was divided into monotonic excursions and equation (3) was applied for each excursion. The initial stress-strain state for each monotonic excursion was taken as the final state from the previous excursion. A generalization of the Stowell equation used in this procedure can be written as

$$K_{\sigma_i} = \frac{\Delta\sigma_i}{\Delta S_i} = 1 + (K_T - 1)\frac{E_{si}}{E} \tag{4}$$

where the subscript "i" refers to the ith monotonic nominal stress excursion ΔS_i. Results from equation (4) agreed closely with experimental results in [13] and [14] for 2024-T3 aluminum alloy specimens under one cycle of loading.

Equation (4) was rewritten by this author [15] as

$$\Delta\sigma_i = \frac{\Delta\epsilon_i \, \Delta S_i}{\Delta\epsilon_i - (K_T - 1)\frac{\Delta S_i}{E}} \tag{5}$$

where $\Delta\sigma_i$ and $\Delta\epsilon_i$ are the independent variables. For given values of K_T and E this equation was used to establish the extreme values of local stress and strain for each nominal stress excursion ΔS_i. These extreme conditions for local behavior were used to control the cyclic loading of unnotched specimens. The local stress-strain curves found by this procedure were compared with experimental results for sheet aluminum and steel specimens with stress-concentration factors of 2, 4, and 6 throughout one cycle of completely reversed loading.

Neuber [9] presents a general theory relating stress and strain-concentration factors for shear-strained prismatical bodies and arbitrary stress-strain laws. Starting from the observation that

$$K_\epsilon > K_T > K_\sigma \tag{6}$$

Neuber postulated the existence of a function, which was neither stress or strain, but a certain combination of both with the characteristic that its concentration factor had the same value for all stress-strain laws and therefore was equal to K_T. This function was called the "leading function" $N(\tau)$ and was defined by

$$\frac{N(\tau)}{N(\tau_N)} = K_T \tag{7}$$

where τ and τ_N are local and nominal shear stresses, respectively.

The leading function was determined from the assumption that the curvature of the notch root remained unchanged for both elastic and general stress-strain behavior. This approach resulted in

$$N(\tau) = \sqrt{\tau F(\tau)} \tag{8}$$

where $F(\tau)$ was a strain function. From equation (7) and the definitions

$$K_\sigma = \frac{\tau_{max}}{\tau_N}$$

$$K_\epsilon = \frac{F(\tau_{max})}{F(\tau_N)}$$

Neuber rewrote (8) as

$$K_T = \sqrt{K_\sigma K_\epsilon} \tag{9}$$

For an evaluation of the leading-function method Neuber [16] applied equation (8) to determine stress-concentration factors for sharp notches in pure shear and compared these results with an exact solution. Satisfactory agreement was shown.

Neuber extended the leading-function method to cases of plane stress in [17] through the use of the deformation theory of Nadai [18] to express the strain function for shear by the strain function for tension. To demonstrate the accuracy of the leading function procedure for plane stress, Neuber applied this method to determine stress-concentration factors at a circular hole in a sheet subjected to uniform radial tension. For comparison, Neuber followed the approach of Budiansky and Mangasarian [19] to obtain an exact solution for this problem corresponding to several levels of strain hardening. For all

cases, the values obtained by the leading-function method were very near to those obtained for the exact theory, demonstrating the accuracy of the leading-function procedure for plane stress.

The Neuber equation (9) was first applied in cyclic loading by Peterson [20] and later by Dolan [21]. These authors as well as Manson and Hirschberg [22], Topper, Wetzel, and Morrow [23] and Wetzel [24] have used the Neuber equation in fatigue studies of notched specimens. These papers will be discussed in the literature review of fatigue prediction methods, and are listed here to demonstrate the wide use of equation (9) in applications with cyclic loading.

Crews [15] rewrote equation (9) in terms of local stress and strain as

$$\Delta\sigma_i = \frac{(K_T\ \Delta S_i)^2}{\Delta\epsilon_i\ E} \tag{10}$$

where $\Delta\sigma_i$ and $\Delta\epsilon_i$ are the local stress and strain excursions corresponding to the ith nominal stress excursion ΔS_i. Equation (10) was used to calculate limiting conditions for each cycle of local stress and strain, and unnotched specimens were cycled between these limits to determine the local stress-strain curves. This procedure will be described in detail in Chapter 3.

Dixon and Stannigan [25] and Dixon [26] experimentally investigated the elastoplastic conditions around crack tips for loading and unloading using a photoelastic coating technique. As a result of these studies, they constructed expressions for stress and strain around the

crack tip during the first load cycles. For the case of notched specimens

$$\Delta\sigma = \sqrt{\frac{E_S}{E}}\,\Delta\sigma_o \tag{11}$$

would be given, where $\Delta\sigma_o$ is the stress excursion corresponding to completely elastic behavior. Since

$$\Delta\sigma_o = K_T\,\Delta S$$

and

$$E_S = \frac{\Delta\sigma}{\Delta\epsilon}$$

equation (11) can be rewritten as

$$\Delta\sigma = \frac{(K_T\,\Delta S)^2}{\Delta\epsilon\,E}$$

Although developed by an entirely different approach, this expression is identical to equation (10), developed from the Neuber equation. The close correlation found in [25] and [26] for results obtained by equation (11) and by photoelastic methods further demonstrated the accuracy of the Neuber equation.

2.3 Methods for Predicting Crack Initiation in Notched Specimens

2.3.1 General

Fatigue prediction methods for notched specimens can be classified into two general categories. The first of these is based upon constant

stress amplitude tests to generate a series of S-N curves for specimens with various stress-concentration factors. To estimate the fatigue behavior for a given specimen configuration, the stress-concentration factor must be calculated or determined experimentally and a constant stress amplitude fatigue life is obtained from the family of S-N curves by interpolating for the desired K_T value. The second basic approach is based on the assumption that a stress-concentration site and an unnotched tensile specimen experience fatigue cracks in the same number of cycles, if they are each cycled through the same stress-strain history. Thus, once local cyclic stress-strain conditions are determined for a stress-concentration site, unnotched specimens can be used to estimate the fatigue crack-initiation period for the stress raiser. The fatigue behavior of unnotched specimens can be characterized by a family of S-N curves.

The fatigue tests for the various K_T levels required by the first approach may be quite expensive and time consuming in contrast to simple laboratory tests of unnotched specimens used in the second approach. Furthermore, loading sequences in variable-amplitude tests affect fatigue behavior of notched specimens and, as a result, a family of S-N curves for various K_T values, in general, apply only for a single loading sequence. On the other hand, the effects of loading sequence could be incorporated in the analysis of local stress and a single family of S-N curves for unnotched specimens could be used for all types of loading. For these reasons the local stress analysis approach will be followed in this study and will be reviewed in the following sections.

Because of simplifying approximations that can be made for local conditions corresponding to tension-tension and completely reversed loading, the following fatigue prediction methods are grouped according to type of loading.

2.3.2 Prediction Methods for Tension-Tension Loading

Gunn [27] applied the modified Stowell equation (3) together with a monotonic stress-strain curve to estimate the maximum stress at a stress raiser. Gunn assumed that the local stress range was elastic after the first cycle, that is, $\Delta\sigma = K_T \Delta S$. From the estimates of maximum local stress and $\Delta\sigma$, Gunn predicted the manner in which yielding lowered the local mean stress for cases of tension-tension loading. By these estimates of local stress behavior, Gunn predicted alternating-mean fatigue diagrams for notched specimens from similar diagrams for unnotched specimens. Although no provisions were made to account for reversed yielding or variations in cyclic material behavior, qualitative agreement was found between predicted and experimental fatigue lives.

Independently, Smith [28] developed a similar method for considering the effect of plasticity on life predictions. Smith assumed that the strain at the concentration site was proportional to nominal stress and calculated the strain from $\epsilon = K_T S/E$. The corresponding notch-root stresses were found from a monotonic stress-strain curve. Residual stress was taken as the difference between the maximum local stress and the elastic local stress range, as in [27]. However, to produce agreement with life predictions based on these results, the

residual stresses were multiplied by an assumed ratio between plastically and elastically deformed material. Local stresses found by this procedure were used together with an S-N curve for unnotched specimens to predict fatigue lives of notched specimens under several levels of reversed (R = -1.0) loading. Miner's linear cumulative damage theory [29] was used to combine these estimated lives for predictions of fatigue behavior under two-level loading. In addition, Smith [30] applied the linear strain theory from [28] to predict fatigue lives for notched specimens under repeated (R = 0) block loading and demonstrated that the highest load level in the spectrum determines the magnitude of the residual stress to be used in estimating the fatigue lives at all other load levels.

Ripp, Gomza, and Adee [31] presented a procedure similar to those of Gunn and Smith, however, the Neuber stress-concentration factor K_N [32] was used instead of K_T.

$$K_N = 1 + \frac{K_T - 1}{1 + \frac{\pi}{\pi - w}\sqrt{\frac{A}{\rho}}} \qquad (12)$$

where A is a material constant, ρ is the notch-root radius, and w is the flank angle of the notch. Because $K_N \leq K_T$, the notch-root strains estimated by Ripp et al. were lower than those obtained by either Smith or Gunn. The comparisons of predicted and observed fatigue lives in [32] reflected the large errors in strain based upon equation (12), especially for the low-life range.

Each of the preceding methods is based upon the assumption of elastic cyclic behavior at the notch root for cycles beyond the first. For $R > 0$ and for low nominal stresses this assumption is justified. However, for $R = 0$ and moderately high nominal stresses, reversed yielding occurs upon unloading (see [15]). Consequently, the fatigue prediction procedures for tension-tension loading must be restricted to low nominal stress ranges for best results.

2.3.3 Prediction Methods for Completely Reversed Loading

Peterson [20] modified the generalized Stowell equation (3) for the fatigue problem by replacing K_T by K_f

$$K_\sigma = 1 + (K_f - 1)\frac{E_s}{E} \tag{13}$$

where K_f is the fatigue notch factor, obtained as the ratio of fatigue limits for unnotched and notched specimens. Peterson used equation (13) together with a cyclic stress-strain curve to estimate local stresses corresponding to specific levels of reversed ($R = -1$) nominal loading. Starting with an S-N curve for unnotched specimens under reversed loading, Peterson constructed an S-N curve for notched specimens in the following manner. The fatigue life was found for each calculated σ (where σ is local stress) from the S-N curve for unnotched specimens and the S used to calculate σ was plotted at this new fatigue life. The procedure was repeated for a range of S to obtain the S-N curve for notched specimens. The procedure was applied for edge-notched sheet specimens of SAE 4130 (normalized)

steel with elastic stress-concentration factors of 2 and 4. Close correlation was found between calculated diagrams and the observed S-N curves in [33].

Dolan [21] suggested a procedure for estimating fatigue lives for notched members based on the Neuber equation (9). Dolan rewrote equation (9) in terms of cyclic amplitude of elastic strain as

$$\frac{K_T \Delta S}{E} = \left[\Delta\epsilon_e \, \Delta\epsilon_t\right]^{1/2} = \Delta\epsilon_t \sqrt{\frac{\Delta\epsilon_e}{\Delta\epsilon_t}} = \Delta\epsilon_t \, F \qquad (14)$$

where $\Delta\epsilon_e$ and $\Delta\epsilon_t$ are, respectively, the elastic and total ranges of local strain and $F = \sqrt{\Delta\epsilon_e/\Delta\epsilon_t}$. For given K_T and ΔS the left side of equation (14) can be evaluated. The right side of equation (14) can be found by successive approximations from a hysteresis loop for the material. The estimate of fatigue life corresponding to $\Delta\epsilon_t$ can be found from a strain-life fatigue diagram for unnotched specimens. Dolan did not investigate the accuracy of this procedure in [21].

Manson and Hirschberg [22] presented an approximate analysis to estimate the number of cycles required to initiate a crack and the number of cycles required to propagate the crack to failure for notched specimens. Cracks were assumed to occur at the root of a notch after a certain number of cycles dependent only on the localized surface strain as in the previously described methods. After the crack reached an "engineering size" it was assumed to propagate in a manner similar to those in unnotched specimens. The number of cycles

to initiate a crack was designated N_o and was calculated for unnotched specimens using

$$N_o = N_f - 4N_f^{0.6} \tag{15}$$

from [34], where N_f is the total life to fracture. Manson and Hirschberg estimated the local strain range using the Stowell equation in the form suggested by Peterson equation (13) and Neuber's equation (9) after replacing K_T by K_f.

$$K_f = \sqrt{K_\sigma K_\epsilon} \tag{16}$$

Local strain estimates were used for establishing predictions of crack initiation at stress concentrations. Life estimates for crack propagation were also made with the assumption that crack growth depended only on the nominal strain range and not on the strain-concentration factor for the notch. Total fatigue life of a notched specimen was the sum of the crack-initiation period and the propagation period. To evaluate this procedure Manson and Hirschberg calculated crack-initiation and propagation periods using equation (16) and compared their results with the observed behavior of 7075-T6 aluminum alloy and AISI 4130 steel specimens having stress-concentration factors of 2 and 3. Close correlation was found between calculated and observed results.

Topper, Wetzel, and Morrow [23] wrote equation (16) in the form

$$K_f(\Delta S\ \Delta e\ E)^{1/2} = (\Delta\sigma\ \Delta\epsilon\ E)^{1/2} \tag{17}$$

where Δe is the nominal strain range. Equation (17) relates the nominal cyclic stress-strain behavior of notched specimens to the local cyclic stress-strain behavior. For completely reversed constant-amplitude tests detectable cracks were assumed to form in notched and unnotched specimens in the same number of cycles provided $K_f(\Delta S\ \Delta e\ E)^{1/2}$ for the notched specimens was equal to $(\Delta\sigma\ \Delta\epsilon\ E)^{1/2}$ for the unnotched specimens. To apply this assumption, Topper et al. used unnotched specimens to produce a "master curve" relating $(\Delta\sigma\ \Delta\epsilon\ E)^{1/2}$ and fatigue lives for unnotched specimens. The life (initiation phase) can be predicted for a notched specimen by entering the master plot at the value of $(\Delta\sigma\ \Delta\epsilon\ E)^{1/2}$ equal to $K_T(\Delta S\ \Delta e\ E)^{1/2}$ for the notched specimen test condition. Life predictions were made by this procedure and compared with observed fatigue lives for edge-notched 7075-T6 aluminum alloy specimens reported in [33]. The close correlation indicates that for this material the crack propagation phase can be neglected.

All four of the preceding methods apply, in general, only to constant-amplitude completely reversed loading. For this special type of loading, local stresses and strains can also be assumed (see [15]) to experience complete reversals and, as a result, local mean stresses are zero. Because of this simplification, maximum and minimum values of local stress and strain can be calculated directly from a cyclic stress-strain curve (generated also by reversed loading) by either the modified Stowell or the Neuber equation. Although not mentioned in [21], this assumption was implicit in the procedure suggested by Dolan.

2.3.4 Prediction Methods for Arbitrary Loading

To predict fatigue of notched specimens under arbitrary types of loading using the local stress analysis approach, local cyclic stresses and strains must be determined, in general, for each loading cycle. This procedure is complicated by the inherent history dependence of local plasticity and by cyclic variations in stress-strain properties. Efforts to simplify this complex problem have led to the approximate analyses and experimental studies reviewed in this section.

The Ranalli method was described in [35] by Silverman, Hooson, and Saleme. This procedure is an extension of Peterson's method [20] to the case of nonfully reversed loading and is based upon semi-empirical methods for determining the strain amplitude and mean stress at the notch root. An equivalent fully reversed strain amplitude giving the same fatigue damage was determined and a fatigue life estimate was obtained for the equivalent strain amplitude from fully reversed constant strain amplitude fatigue curves.

The Ranalli method was applied to estimate fatigue lives for constant-amplitude tests and for simple spectrum loading. The linear damage theory (Miner's Rule) was used for the spectrum loading tests to account for fatigue damage at each stress level. Although based upon semi-empirical methods for analyzing local behavior, the Ranalli method was generally concluded to be of considerable value as a practical fatigue design method.

Wetzel [24] applied equation (9) to calculate control conditions under which unnotched specimens were made to simulate fatigue behavior

of material at a notch root. This procedure was similar to that used by Crews [15]. However, Wetzel replaced K_T by K_f in the Neuber equation to calculate the control conditions. This substitution improves the fatigue-prediction results for constant-amplitude loading, but could result in large errors for local stress-strain calculations, especially for high K_T values where K_T and K_f are usually quite different. Endpoint conditions for each half-cycle of local stress-strain behavior were calculated from equation (9) and an unnotched specimen was successively cycled between the limits. This procedure can be applied for complicated types of loading, since each half-cycle of loading is handled separately. Wetzel applied the procedure to simulate local fatigue behavior for $R = 0$ loading, and close correlation was found between calculated and observed results.

In [1], local stress conditions were determined by a numerical elastoplastic analysis but, in addition, experimental methods were used to find local stresses for constant-amplitude $R = 0$ loading. Unnotched specimens were cycled between these experimental limits and the resulting fatigue lives were compared with lives found from fatigue tests of notched specimens. For the two test conditions considered, close correlation was found.

A more extensive experimental study of local stress behavior was presented in [13]. Local strains were measured while notched specimens were loaded cyclically and these measured strains were reproduced in tests of unnotched specimens to determine the corresponding local stress histories. For the 2024-T3 aluminum alloy investigated, local stresses

were found to reach stabilized levels. Fatigue lives for notched specimens were estimated from these stabilized local stresses and fatigue data for unnotched specimens.

2.4 Analysis of Crack Propagation Near Stress Concentrations

Crack initiation may occur in the early stages of fatigue life with the result that the crack propagation phase must be considered for accurate estimates of total fatigue life. Fatigue cracks initiate at areas of high stress concentration and grow away from these areas as cyclic loading is continued. The initial stage of this crack propagation is influenced by the stress field due to the stress raiser, but as the crack grows it gradually escapes this influence and propagates solely under the influence of the applied nominal stress. The behavior of fatigue cracks under applied nominal stress has received much attention in the literature (for example, [36], [37], and [38]) and, as a result, was not dealt with here. On the other hand, fatigue crack growth near stress concentrations has received only limited attention.

Manson and Hirschberg [22] discussed the transition period between crack initiation and crack propagation under nominal stress. This period was included in their analysis by defining N_o, not as the number of cycles to form a microcrack, but rather as the number of cycles to form an engineering size crack according to the equation (15). While Manson and Hirschberg recognized that this simplification was highly questionably, the results associated with this assumption were compared with observed behavior to assess its validity. In general, the comparisons made in [22] supported their simplifying assumption,

however, the validity of this approach is contingent upon the appropriate selection of the engineering size crack.

Because this transition phase of crack growth depends upon the stress distribution around the stress concentration, loading sequences that alter this stress distribution through the creation of residual stresses also influence this initial phase of crack growth. While several studies have been conducted to establish the effects of prior loading on fatigue crack initiation or total fatigue life (for example, [39] and [49]), the effects of this loading on crack propagation have not been analyzed. Taira and Murakami [41] measured crack growth from V notches in plates that had been statically loaded in tension prior to fatigue testing.

Prior tensile loading was found to suppress the initial stage of crack growth. This decrease in crack growth rate was attributed to compressive residual stresses produced by the prior loading. However, no analysis of this effect was presented.

In summary, although several investigators have mentioned the transition phase of crack growth from a stress raiser, no deliberate study has been made of this phase of fatigue. For some applications this phase may represent a significant part of the fatigue life, and, as a result, should be considered in fatigue predictions.

3. ANALYSIS OF LOCAL CYCLIC STRESS AND STRAIN

3.1 General

The present study of local stress and strain was undertaken to demonstrate a procedure for estimating local conditions and to establish the adequacy of this procedure by comparison of calculated and experimental results. In addition, the local stress-strain results developed in this study were used in the next chapter, which deals with crack-initiation behavior at stress-concentration sites.

The present interest in the analysis of local stress and strain stems from the fact that fatigue is a very localized process. Without adequate procedures for calculating the local conditions at the fatigue critical sites of a structure, predictions of fatigue life are impossible. For weight critical structures, the analysis of local cyclic behavior is quite complicated. The history dependence of local plasticity combined with the cyclic strain hardening or softening experienced by most materials virtually preclude exact solutions for local stress and strain beyond the first few loading cycles.

For the purposes of this study the problem of local stress analysis was simplified by considering the specimen configuration shown in figure 3.1. (This specimen will be referred to herein as the "notched" specimen.) Because this specimen was thin and was stressed by inplane loading, a plane stress condition existed. The elastic stress distribution [42] on the transverse axis is shown in figure 3.2 for the specimen dimensions given in figure 3.3. The fatigue critical points for this configuration lie on the boundary of the hole at

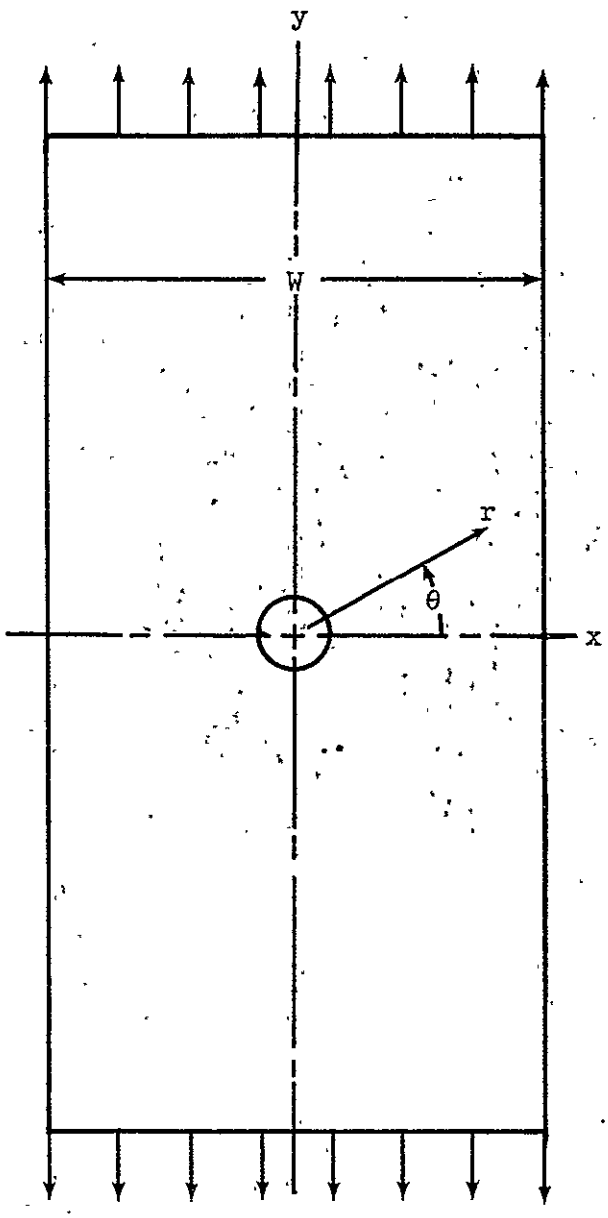

Figure 3.1 – Notched specimen configuration, loading, and coordinate system.

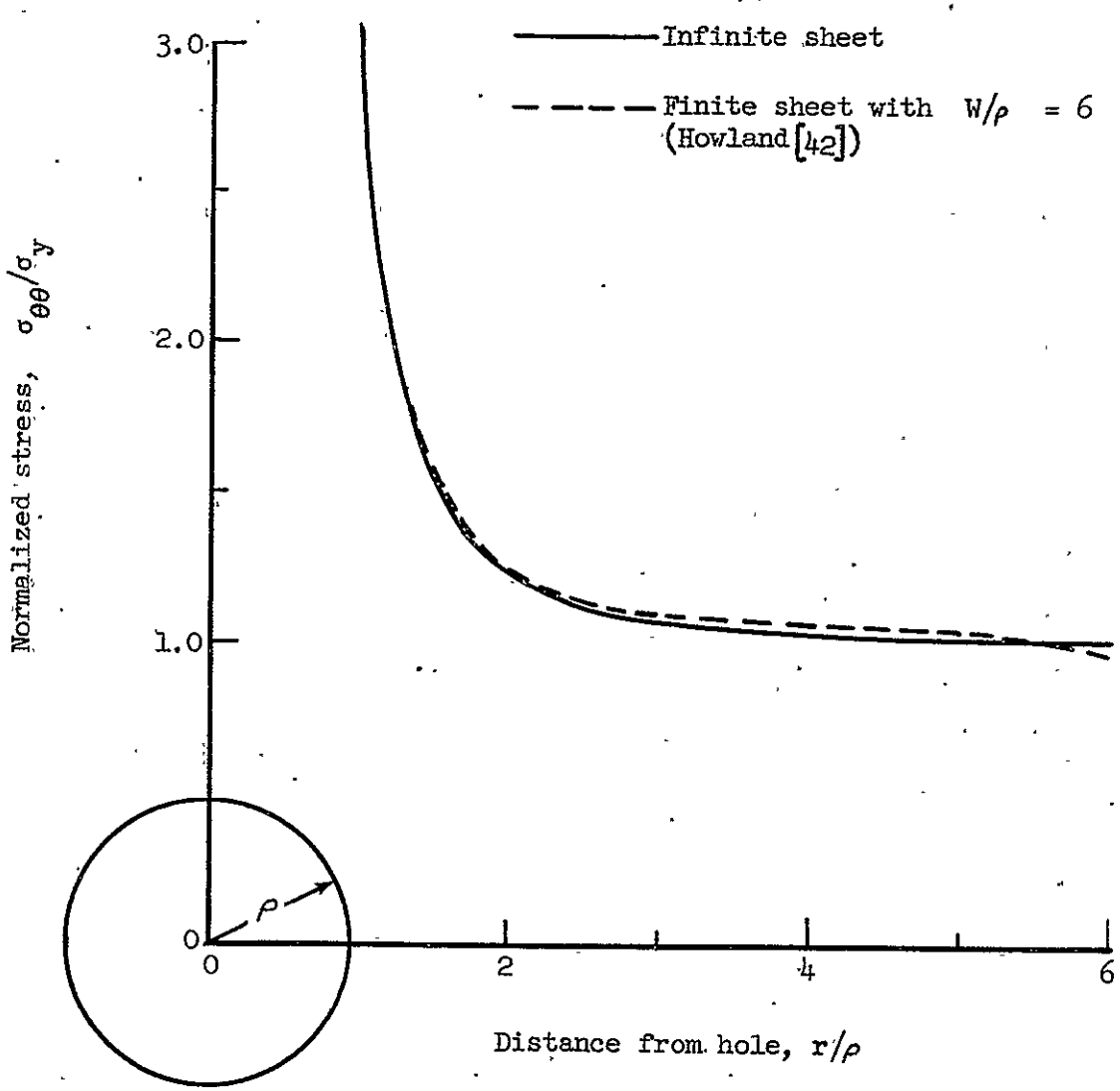

Figure 3.2 – Elastic stress distributions on transverse axis.

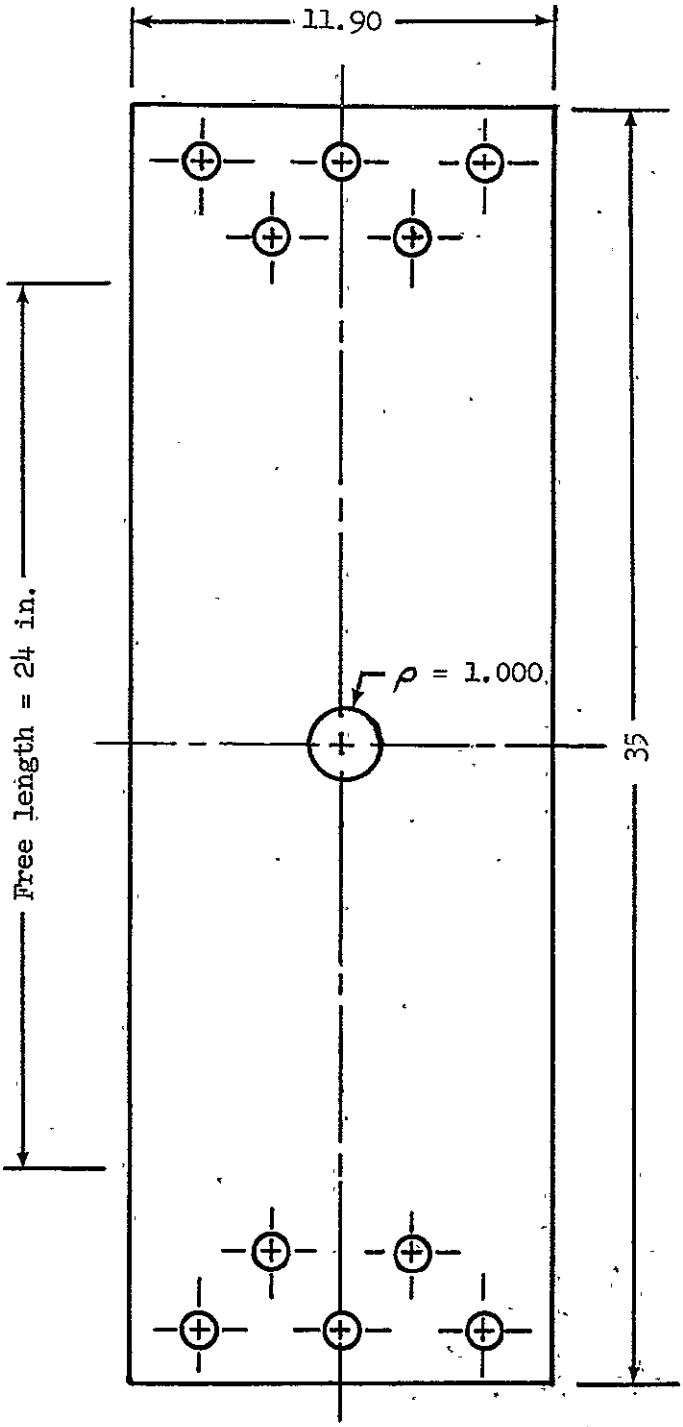

Material: 2024–T3
Thickness: 0.156 in.

Figure 3.3 – Notched test specimen dimensions.

$\theta = 0$ and π. Because these points were on the stress-free boundary of the hole, they were in a uniaxial state of stress which leads to significant simplifications in this study of cyclic behavior. Throughout the remainder of this chapter, attention will be restricted to these points and conditions at these critical points will be referred to as "local" conditions. Based on net-section nominal stress, the elastic stress-concentration factor for these points is 2.57 [42]. In addition, the comparison in figure 3.2 illustrates no effect on local conditions by the finite specimen width shown in figure 3.2.

As a result of the uniaxial stress state at the local points, the local cyclic conditions can be simulated in simple unnotched uniaxial specimens. Local behavior was determined using this procedure. Two methods were used to control the simulation. In the first method, referred to here as analytical-control method, limiting conditions involving local stress and strain were calculated and the unnotched uniaxial specimens were cycled between these limits. The second method was entirely experimental in nature, and was used to establish the accuracy of the analytical-control method. This experimental method, called the companion-specimen method, was based upon the experimental determination of local cyclic strain limits and the cyclic testing of unnotched companion specimens between these limits.

Two types of cyclic loading were considered in this investigation. To demonstrate the variations in local stress and strain due to cyclic strain hardening and to establish the ability of the analytical-control method to account for this material behavior, tests and analysis were

conducted for constant-amplitude cyclic loading. The effects of loading sequences on local behavior were studied for several simple cases of variable-amplitude loading.

Details of procedures and apparatus are presented in the following sections. Discussions and comparisons are made between the calculated and experimental results for an evaluation of the analytical-control procedure.

3.2 Analytical-Control Method

The procedure described in this section is based upon the simulation of local behavior in unnotched specimens. Because the fatigue critical points for the notched specimen configuration considered in this study experienced only uniaxial stress, unnotched specimens under simple uniaxial loading were used for the simulation of local stress and strain. These plain specimens were cycled between calculated limits, involving local stress and strain, to perform the simulation.

Two equations are currently available for calculating the limiting conditions for local stress and strain. These are the generalized Stowell and the Neuber equations.

The Stowell relationship given in the literature review as equation (4)

$$K_\sigma = \frac{\Delta\sigma_i}{\Delta S_i} = 1 + (K_T - 1)\frac{E_{s_i}}{E} \qquad (4)$$

was rewritten in terms of $\Delta\sigma_i$ and $\Delta\epsilon_i$ as

$$\Delta\sigma_i = \frac{\Delta\epsilon_i \, \Delta S_i}{\Delta\epsilon_i - (K_T - 1)\frac{\Delta S_i}{E}} \tag{5}$$

Similarly the Neuber equation was written as

$$\Delta\sigma_i = \frac{(K_T \, \Delta S_i)^2}{E \, \Delta\epsilon_i} \tag{10}$$

For the purpose of establishing the extreme values of local stress and strain for the analytical-control method, either equation (5) or equation (10) could have been used. However, based upon the simplicity of equation (10) and upon the evaluation of the analytical-control procedure for constant-amplitude loading performed by the author in [15], equation (10) was selected for this study.

The cycle-by-cycle procedure for applying the analytical-control method can be explained with the aid of figure 3.4. An arbitrary nominal stress cycle has been divided into monotonic excursions in figure 3.4(a), and the corresponding estimates for the local stress-strain behavior are presented in figure 3.4(b). To illustrate the procedure, equation (10) has been evaluated for a given K_T and E and plotted in the first quadrant of figure 3.4(b) for ΔS_i. This curve for equation (10) represents the locus of maximum values of local stress and strain for ΔS_i. An unnotched specimen was loaded in uniaxial tension to obtain the stress-strain curve 0A. Point A corresponds to the intersection of the curve for equation (10) and the stress-strain curve, and, as a result, represents the only solution ($\Delta\sigma_1$ and $\Delta\epsilon_1$) of equation (10) consistent with the material

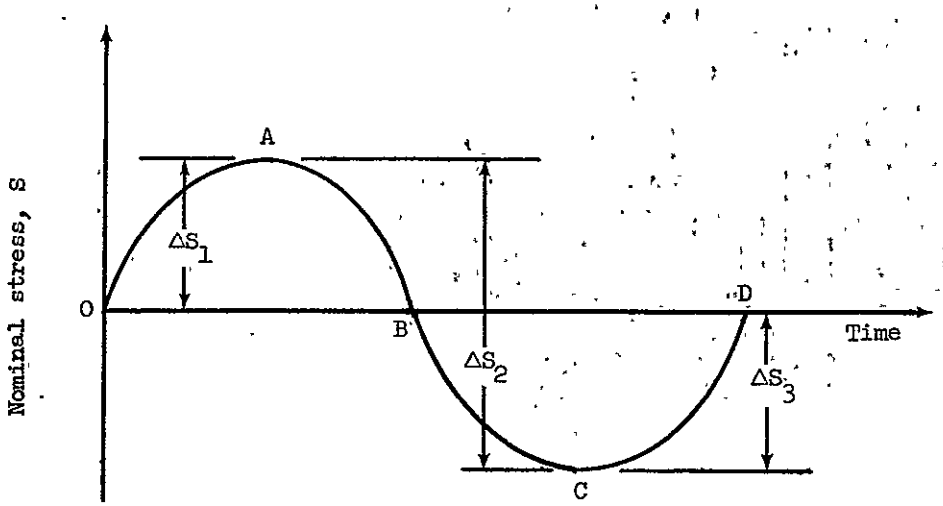

(a) Nominal stress cycle

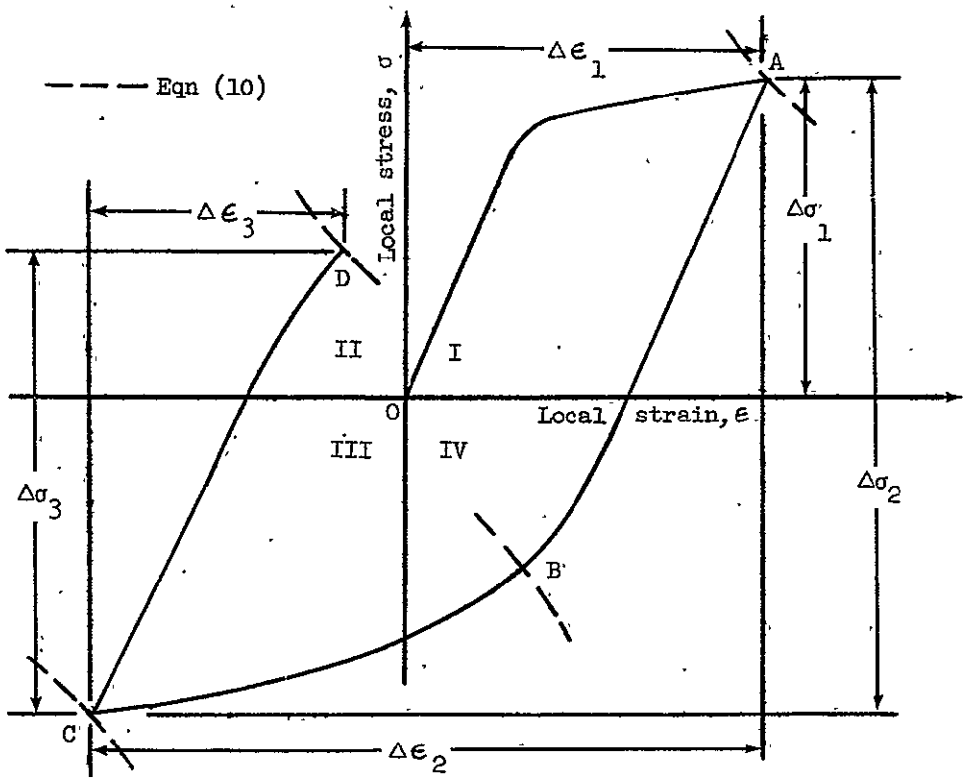

(b) Estimated local stress–strain curve

Figure 3.4 – Nominal stress cycle and estimated local stress–strain curve.

stress-strain behavior OA. Thus point A represents the estimated maximum values for local stress and strain during the first quarter cycle.

For the second excursion of nominal stress ΔS_2 point A was taken on the initial state. Correspondingly, equation (10) was plotted relative to point A for ΔS_2. This curve for equation (10) lies in the third quadrant. The unnotched specimen was unloaded from point A and loaded into compression until the resulting stress-strain curve intersected the limiting curve for ΔS_2. This intersection point C represents the estimate for the minimum values of local stress and strain for this cycle of nominal stress.

Point B in figure 4(b) represents the half-cycle residual stress-strain state and was found by plotting equation (10) relative to A for the removal of ΔS_1 from the specimen. Point D, representing the full-cycle residual condition, was found in a similar manner.

The local stress-strain curves for cycling beyond the first cycle were found by repeatedly applying the procedure used to find the extreme points A and C.

Because this procedure was applied in a continuous cycle-by-cycle manner, the history dependence of local behavior was automatically simulated in these tests with unnotched specimens. In addition, the influence of the cyclic strain-hardening behavior for the material used in this study was inherently incorporated into the local stress-strain results.

The unnotched specimen configuration shown in figure 3.5 was used throughout this study. These specimens were made from 2024-T3 aluminum

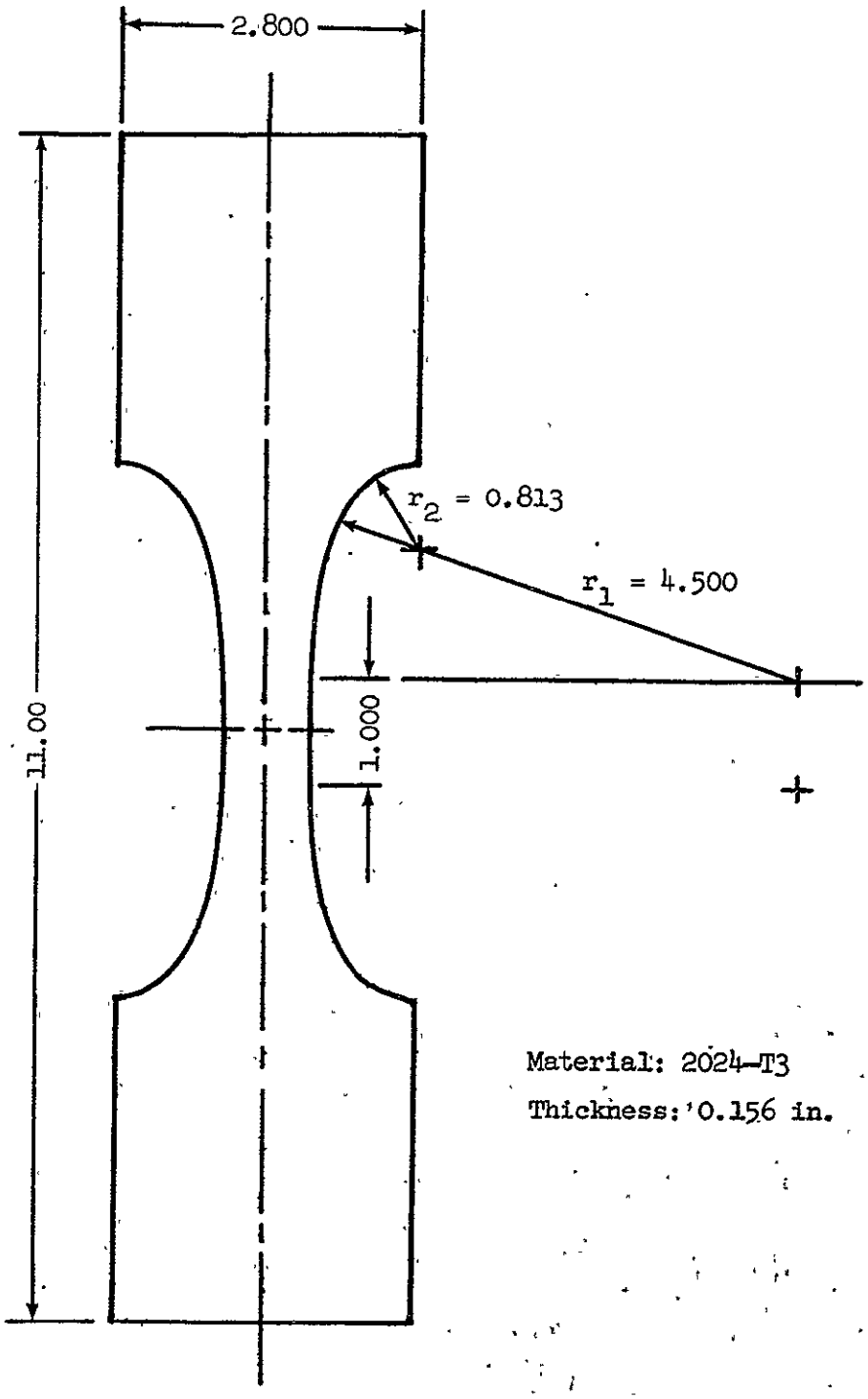

Figure 3.5 – Unnotched specimen configuration and dimensions.

alloy sheet, and were all oriented such that their longitudinal axes were parallel to the rolling direction of the sheet stock.

The hydraulic closed-loop, servo-control testing system shown in figures 3.6 and 3.7 was used for cycling the unnotched specimens between the calculated limits for local stress and strain. While this system was capable of controlling either load or strain, neither control mode was used for this phase of the study. Flow control valves were adjusted to limit the strain rates in the specimens, and the loading controls were first set for capacity tensile loading. Because of a limited strain rate, the stress-strain curve was slowly generated. When this curve intersected the limiting curve for maximum local stress and strain (see fig. 3.4) the loading controls were manually reversed. Similarly the loading controls were manually reversed when the stress-strain curve intersected the limiting curve for minimum local conditions. This procedure was repeated for each half-cycle throughout the analytical control test. Guideplates shown in figure 3.8 were used to prevent buckling during the compressive loading.

The stress-strain curves obtained in this phase of the study were recorded using an x-y recorder shown in figure 3.7. The load (stress) input to this recorder was taken from the dynamometer shown in figure 3.7. The strain input was provided by the strain-gage extensiometers also shown in this figure. The pair of extensiometers, shown again in figure 3.8, were used to determine the average strain over the 1-inch test section of the specimen. In addition, to reduce strain errors due to bending, an average output from the two extensiometers was used.

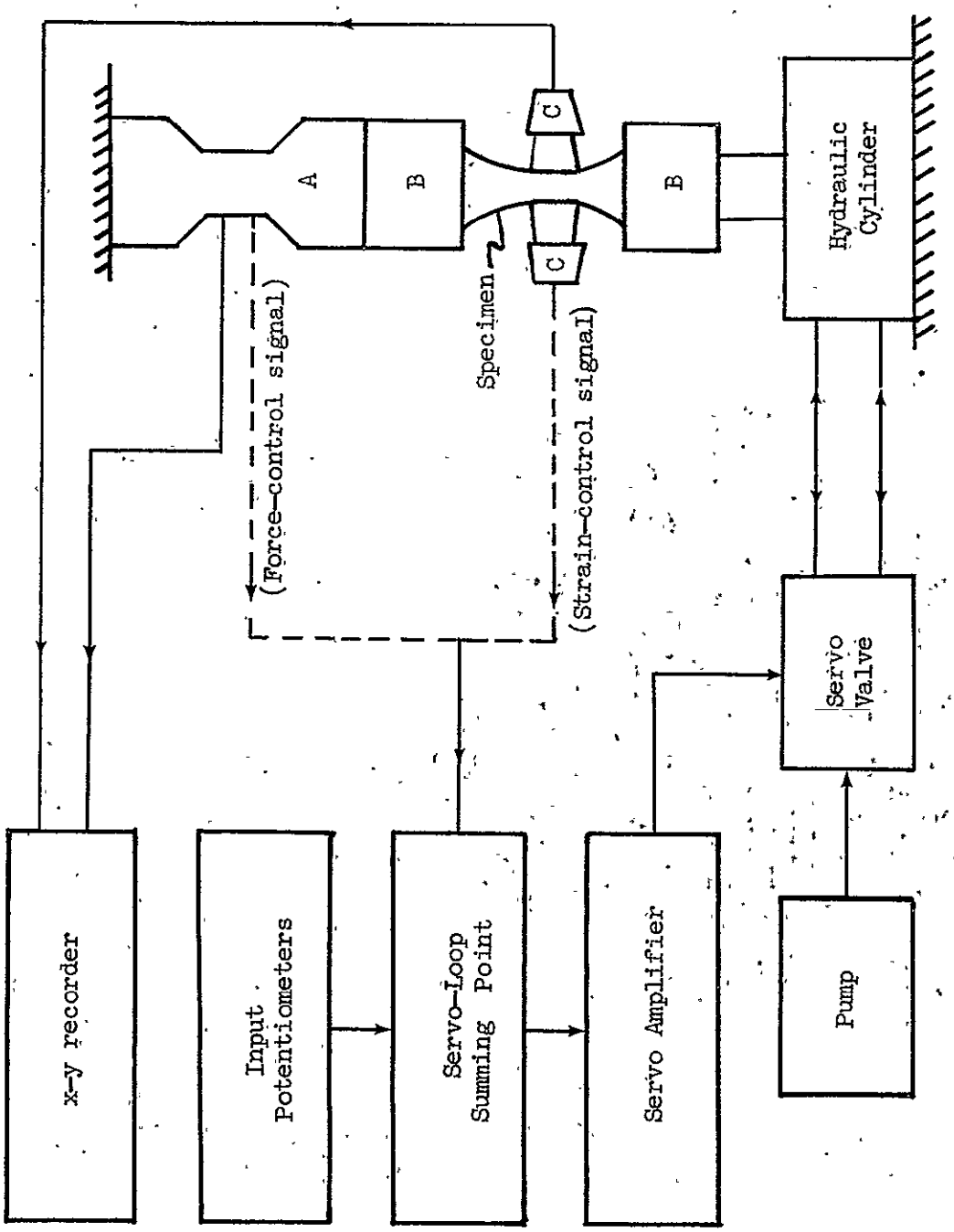

A — Dynamometer. B— Specimen grips C — Extensometers

Figure 3.6 — Block diagram for hydraulic servo-control testing system.

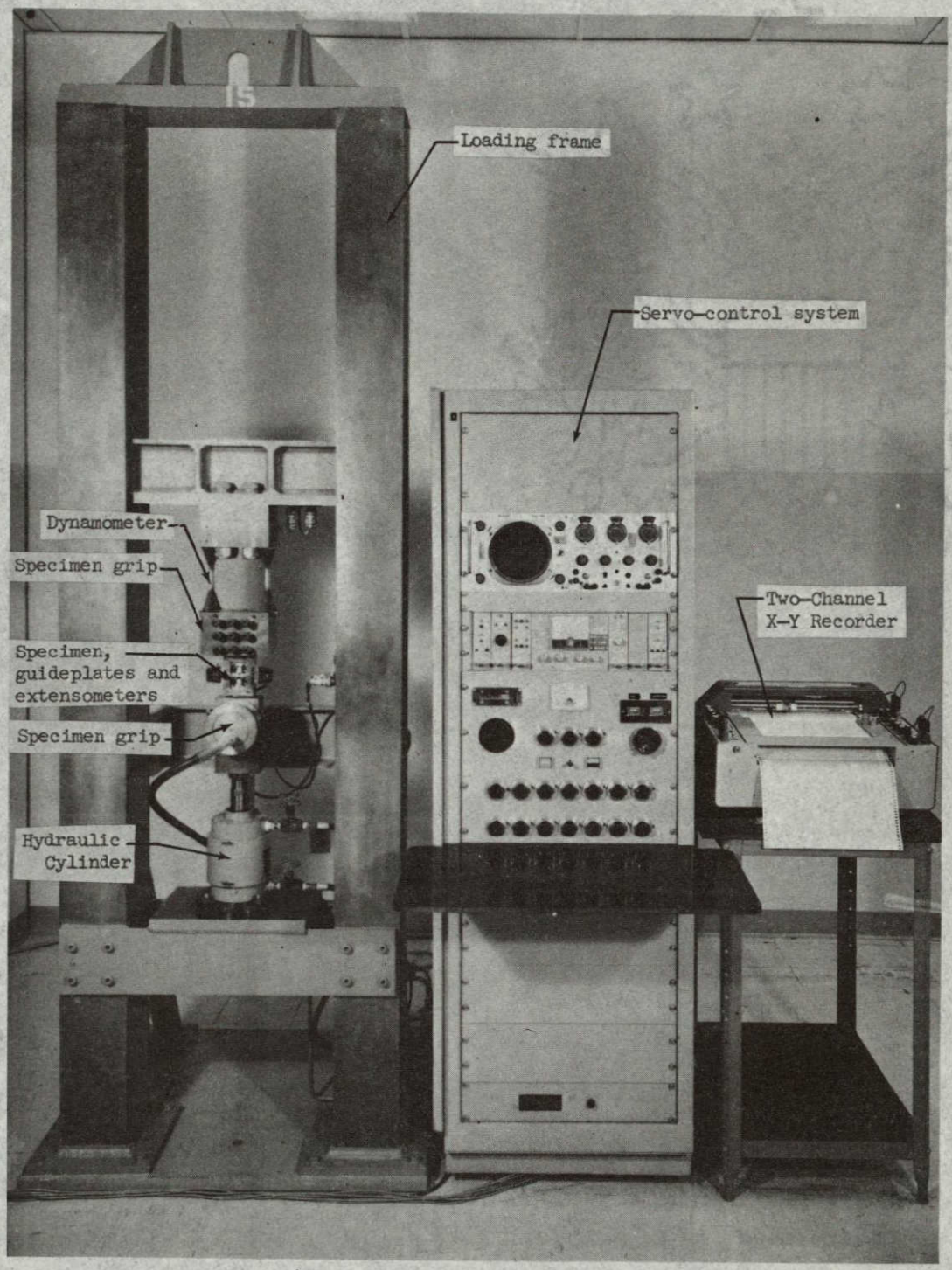

Figure 3.7 – Photograph of apparatus used for analytical-control tests.

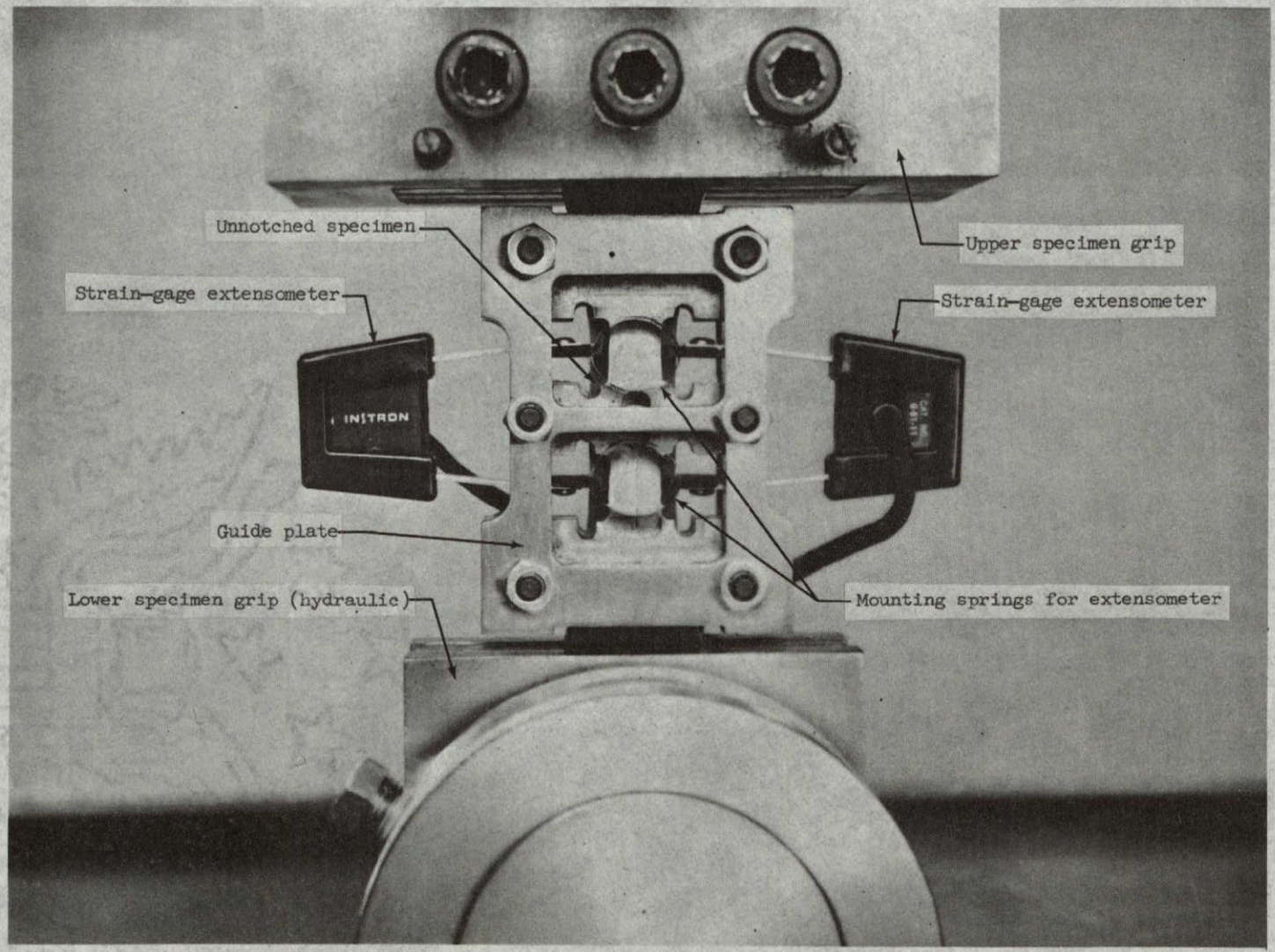

Figure 3.8 – Photograph of unnotched specimen in test machine.

3.3 Companion-Specimen Method

To evaluate the accuracy of the analytical-control procedure, local stress and strain were determined experimentally by a companion-specimen method. Local strain limits are found experimentally for each loading cycle on the notched specimen and, these limits are used to control the cyclic simulation of local behavior with unnotched companion specimens.

The notched specimens tested in this phase of the study were the sheet aluminum specimen containing a central hole, as shown in figure 3.3. The unnotched specimen configuration shown in figure 3.5 was used for the companion specimens.

To synchronize the notched specimen and the corresponding companion-specimen tests, the control system shown in figure 3.9 was developed. Loading on the notched specimen was controlled by a closed-loop servo-control system also presented in figure 3.9.

As the notched specimen was loaded, the averaged output from two small strain gages mounted at the local points and outputs from two similar strain gages on the companion specimen were compared at the servo-loop summing point. The difference between these two signals served as an input to a second servo-control system that controlled the loading on the unnotched specimen. This second control system maintained the strain in the companion specimens equal to that experienced at the local point. A dual-channel x-y recorder was used to simultaneously record the loads on both specimens and the common local strain. Photographs of the loading system and the servo controls are shown in figure 3.10.

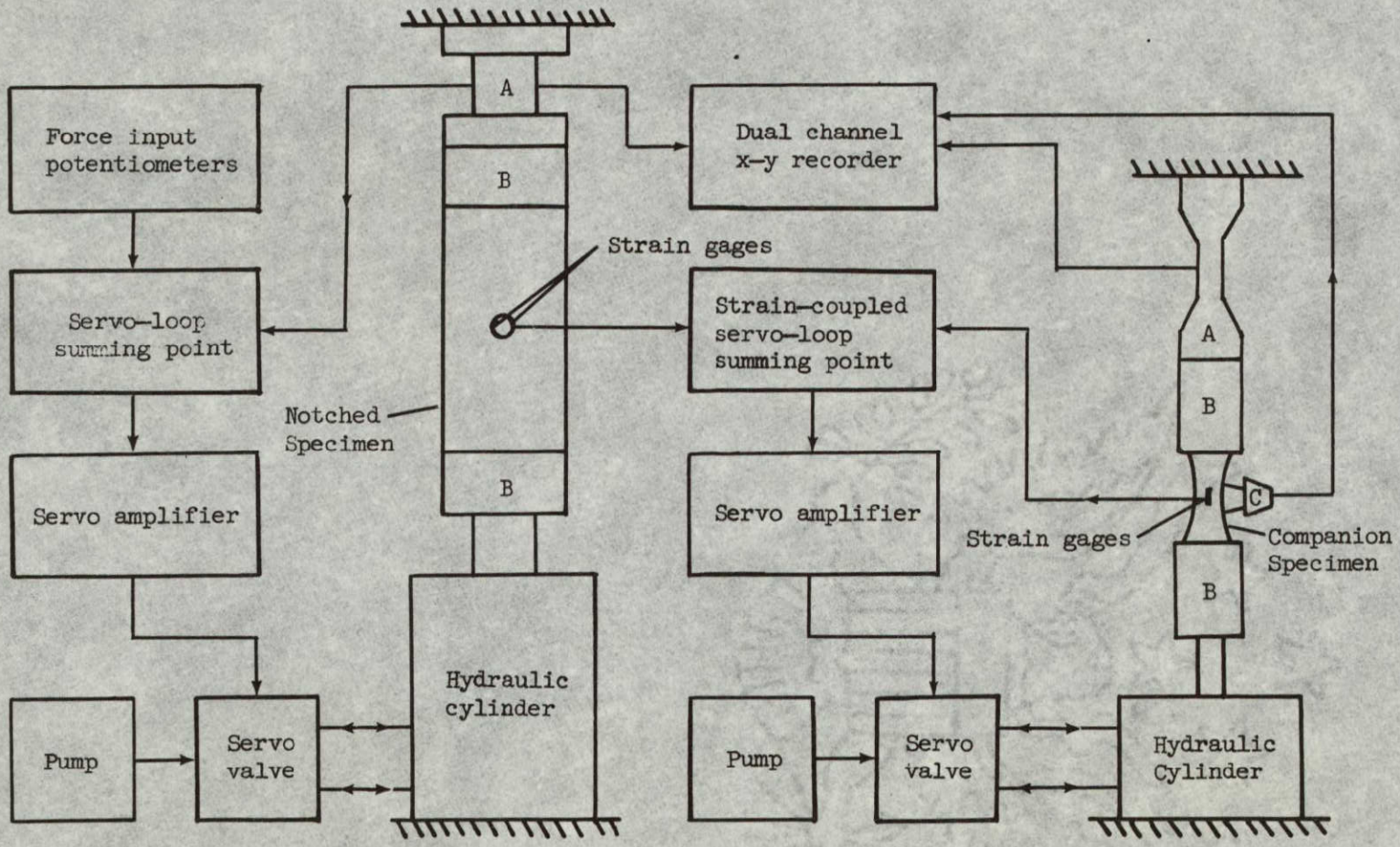

A – Dynamometer B– Specimen grips C– Extensometer

Figure 3.9 – Block diagram of strain–coupled servo–control system.

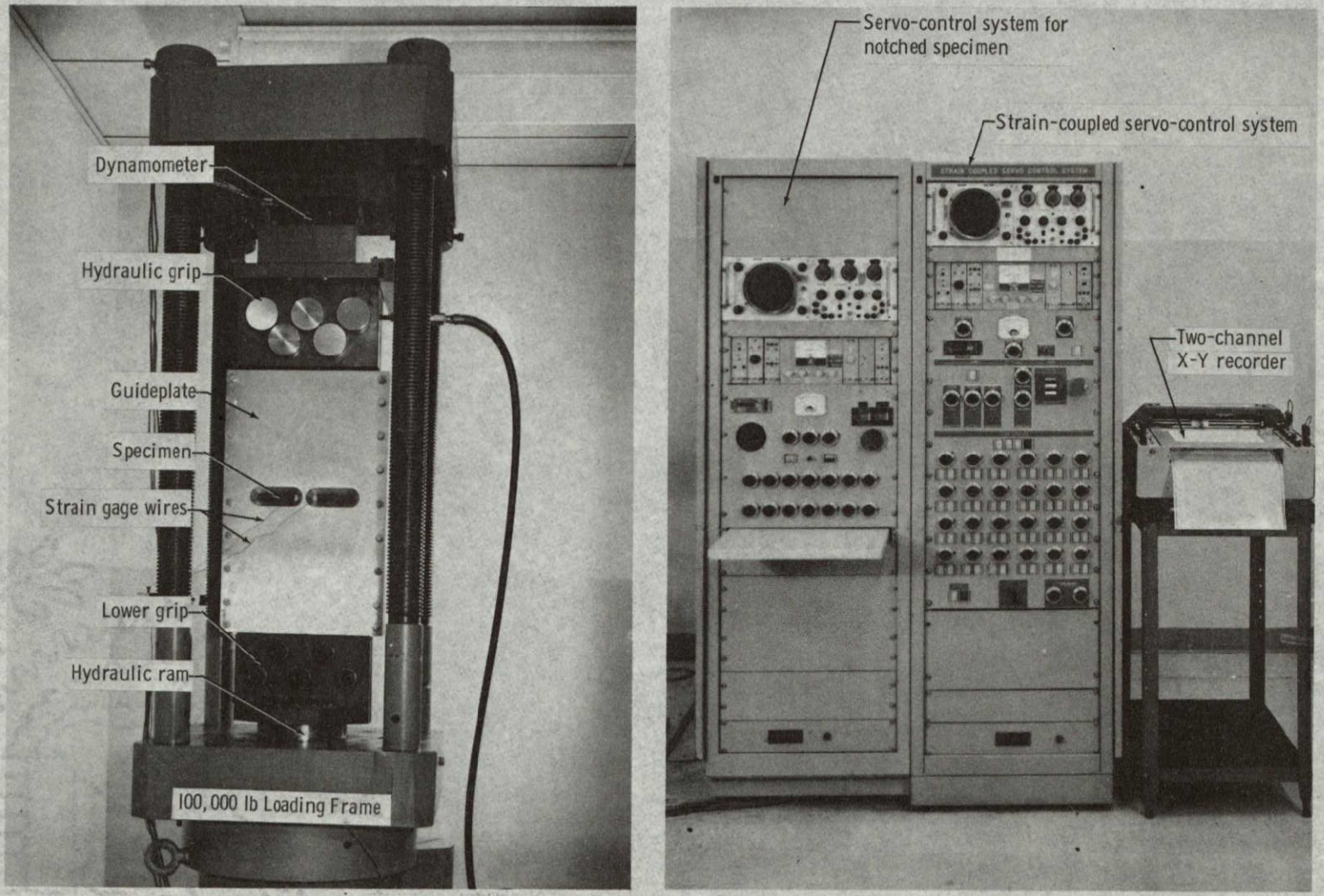

Figure 3.10 – Photograph of apparatus for companion-specimen (strain-coupled) tests.

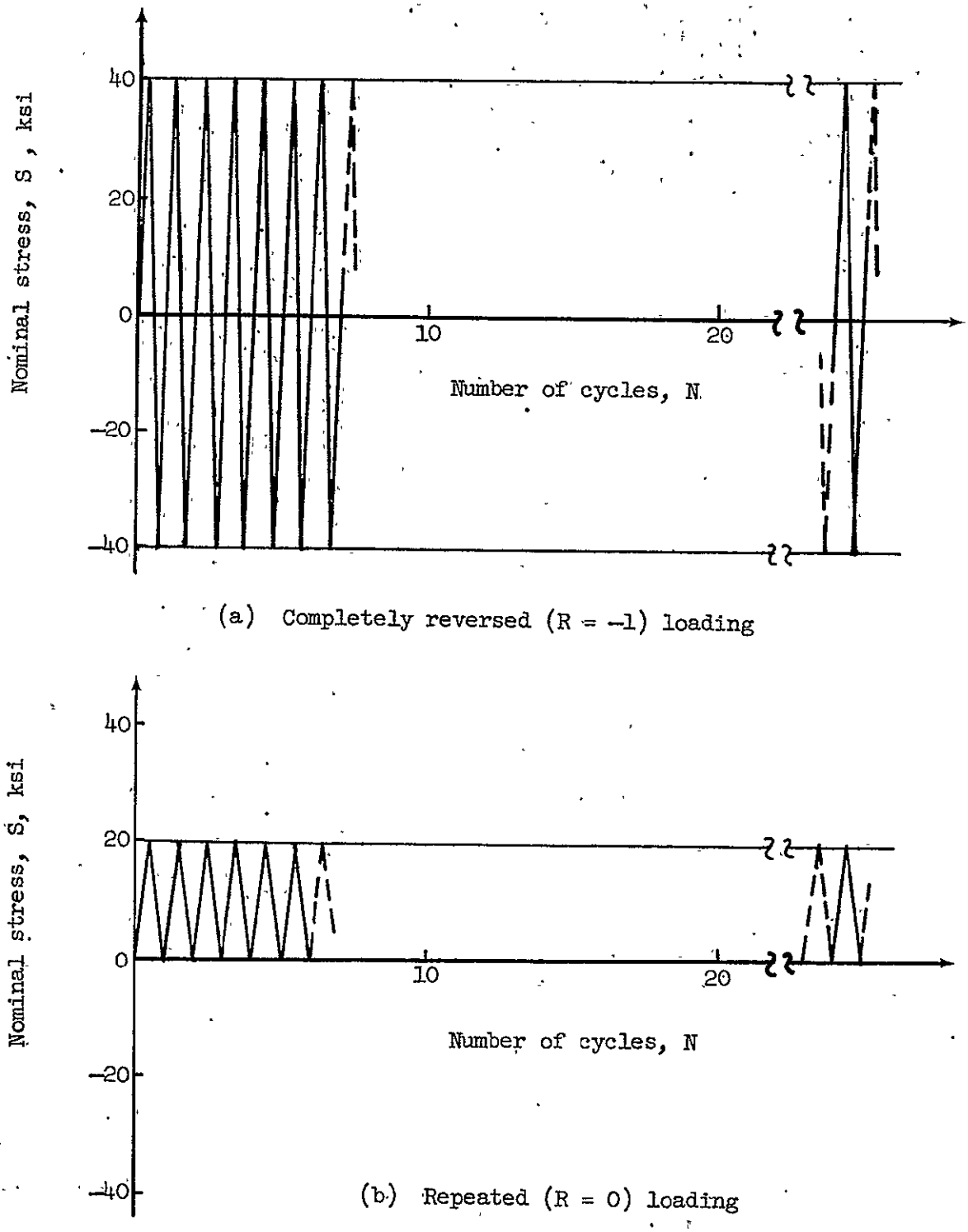

Figure 3.11 – Constant-amplitude nominal stress conditions.

2

Guideplates shown in this figure were used to prevent specimen buckling under compressive loads.

3.4 Test Program

As previously mentioned, the objective of the local stress-strain phase of this study was twofold. An evaluation of the analytical-control technique was sought, and, in addition, the local stress-strain results from this evaluation were to be used in the analysis of crack-initiation lives. Loading sequences were selected with these objectives in mind.

To investigate the adequacy of the analytical-control method in accounting for cyclic strain hardening, two types of constant-amplitude loading were considered. Simple two-level loading and a random sequence of loading were selected as examples of variable-amplitude loading. To demonstrate the use of local stress and strain for analysis of crack initiation, the loading sequences and magnitudes were selected to produce effects on initiation behavior due to local residual stresses. Details of these loading conditions follow.

3.4.1 Constant-Amplitude Loading

Two types of constant-amplitude loading were studied. The first of these, shown in figure 3.11(a), was completely reversed (R = -1) loading. For the notched specimen configuration and materials investigated, this loading produced local inelastic behavior for both tensile and compressive loading. The repeated (R = 0) loading shown in figure 3.11(b), created only elastic stresses throughout the notched specimen. As a result, this loading condition was of little interest

in this phase of the study but played an important role in the fatigue crack-initiation study and therefore was included here for completeness.

3.4.2 Variable-Amplitude Loading

The above mentioned two types of loading were combined in two-level loading sequences shown in figure 3.12. For these conditions residual stresses are produced during load reversal. These residual stresses affect the fatigue resistance of the notched specimen during the second level of loading.

The fatigue behavior corresponding to these two types of loading will be discussed in the next chapter. In this chapter these loading sequences were used to demonstrate the role of high stresses in creating local residual stresses that alter subsequent local stress-strain conditions and to demonstrate the accuracy of the analytical-control method for calculating these effects. The random stress sequence in figure 3.13 was also investigated to illustrate the adequacy of the analytical-control method for arbitrary loading sequences and magnitudes.

Local stresses and strain were found for each of the loading conditions in figures 3.11, 3.12, and 3.13 by both the analytical-control and the companion-specimen methods. These results are presented and discussed in the following section.

3.5 Experimental Results

The strain-coupled servo-control system was used to conduct companion-specimen tests for each loading condition. A typical recording from the dual channel x-y recorder is shown in figure 3.14. Local stesss and strain are plotted in figure 3.14(a) corresponding to

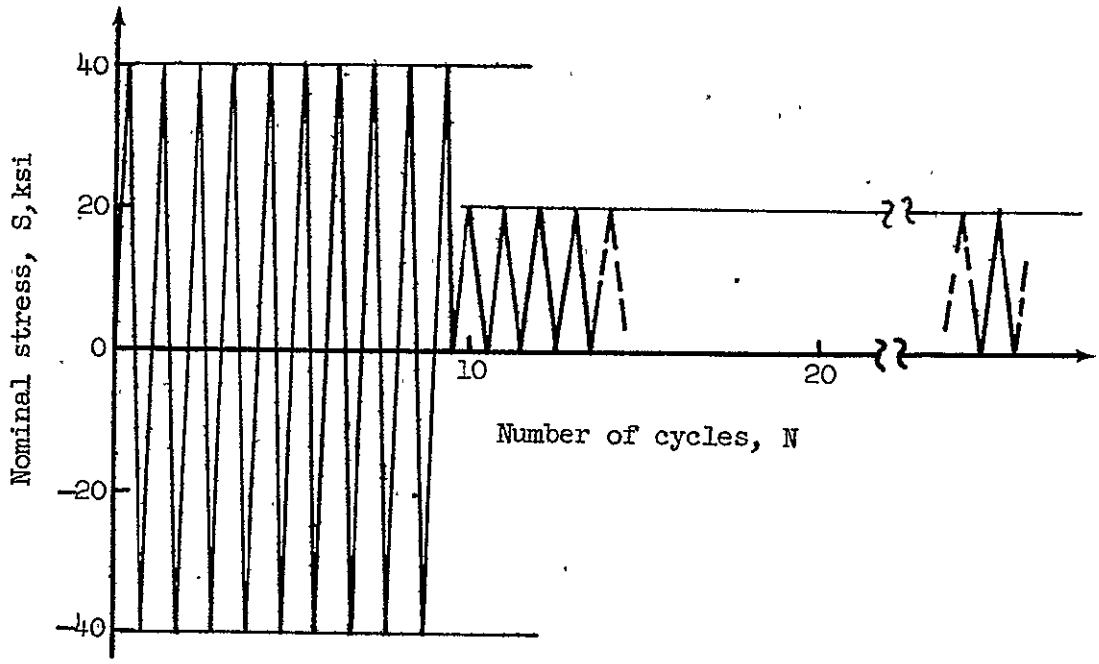

(a) Beneficial prior loading

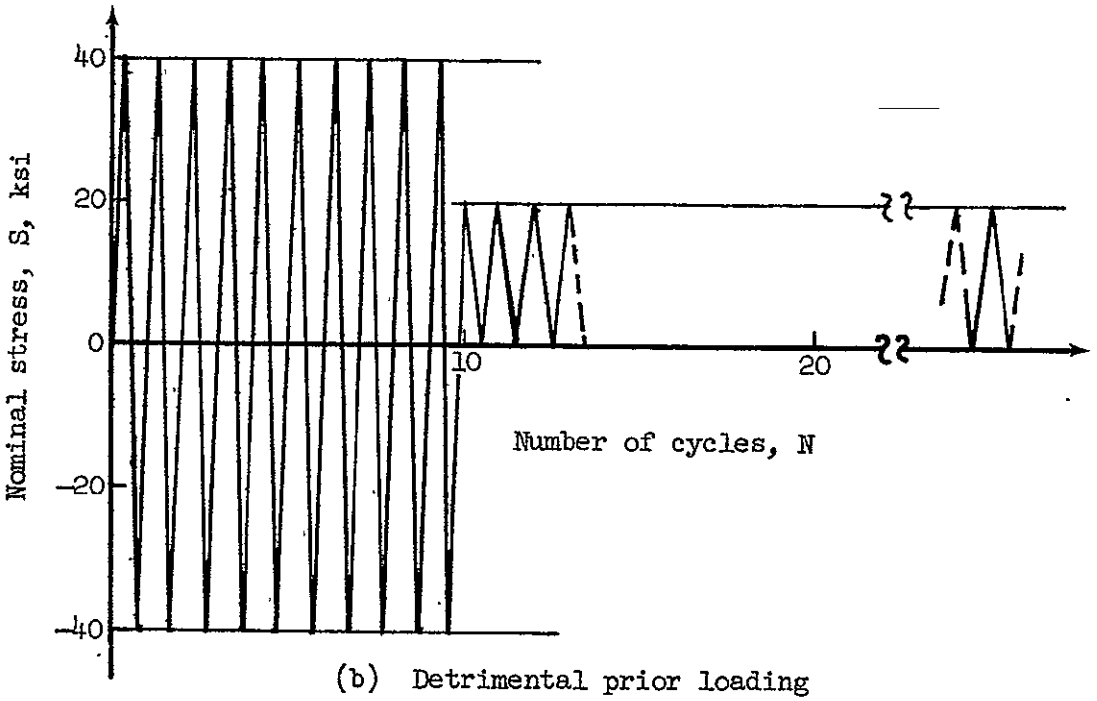

(b) Detrimental prior loading

Figure 3.12 – Two-level nominal stress sequences.

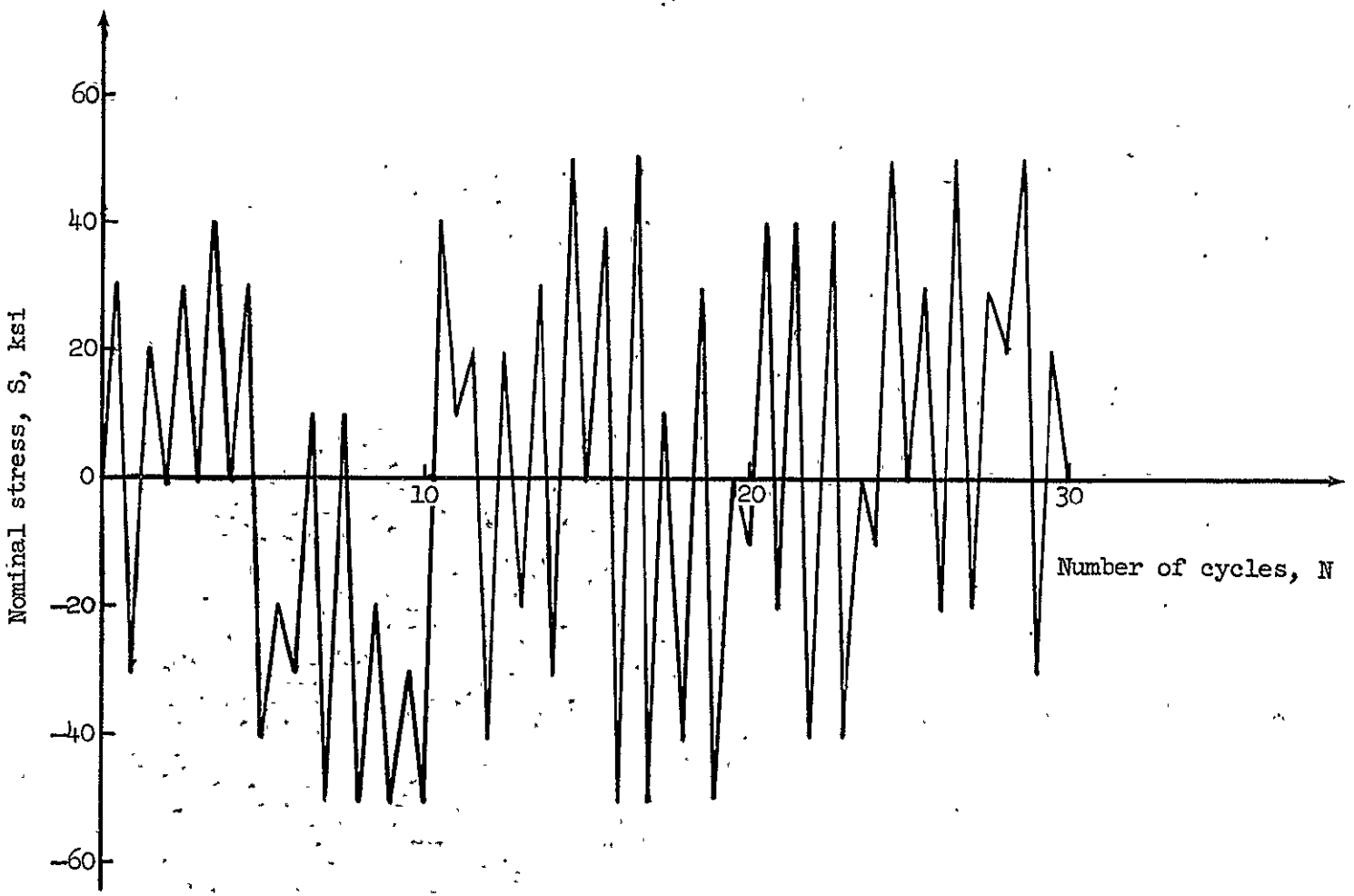

Figure 3.13 – Sequence of random nominal stress levels.

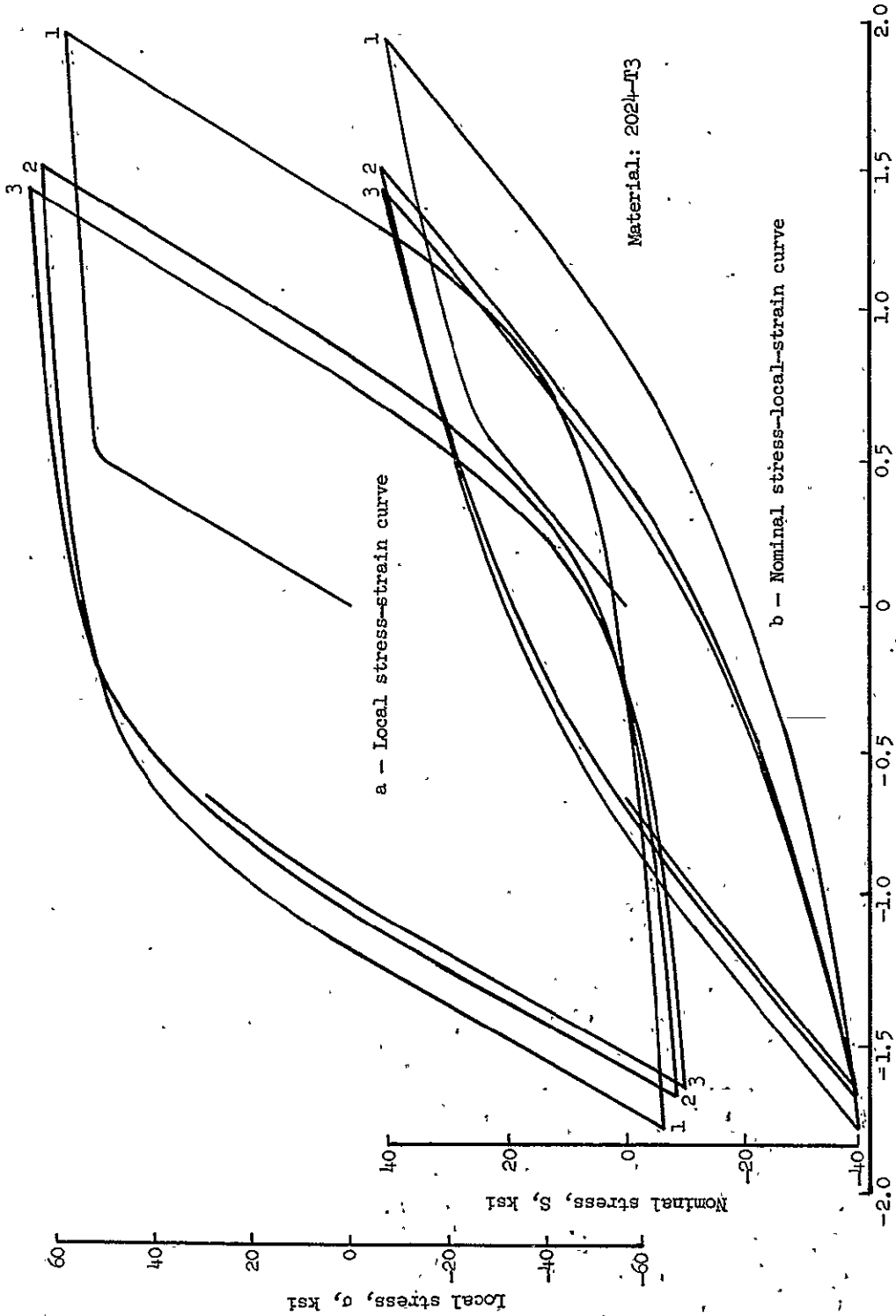

Figure 3.14 – Typical recording from companion-specimen tests.

the nominal stress and local strain in figure 3.14(b). Recordings were made throughout the first 50 load cycles. Maximum, minimum, and residual stresses and strains were determined from these recordings for each type of loading. These salient local stresses and strains were plotted for 50 cycles of loading and will be discussed in the following sections.

In addition, elastic stress-concentration factors were determined experimentally for each test specimen. Prior to the strain-coupled operation, strain-gage readings were taken at each of 10 nominal stress levels, as each notched specimen was loaded to 80 percent of the local yield stress. The experimental elastic stress-concentration factor K_{exp} for each specimen was the average of the 10 values found for each case. These average values based on net nominal stress varied from 2.54 to 2.59 with an overall average value of 2.57 which agreed with the value given by Howland [42] for this specimen configuration (fig. 3.3).

3.5.1 Constant-Amplitude Loading

Maximum, minimum, and residual stresses and strains for the two cases of constant-amplitude loading are presented in figures 3.15, 3.17, 3.18, and 3.19. The dashed curves also shown on these figures will be discussed later.

The local stress of 51 ksi shown in figure 3.15 for S = 20 ksi equals the monotonic yield stress for 2024-T3 aluminum alloy as illustrated in figure 3.16. Consequently the local stress-strain behavior was initially elastic for this loading condition.

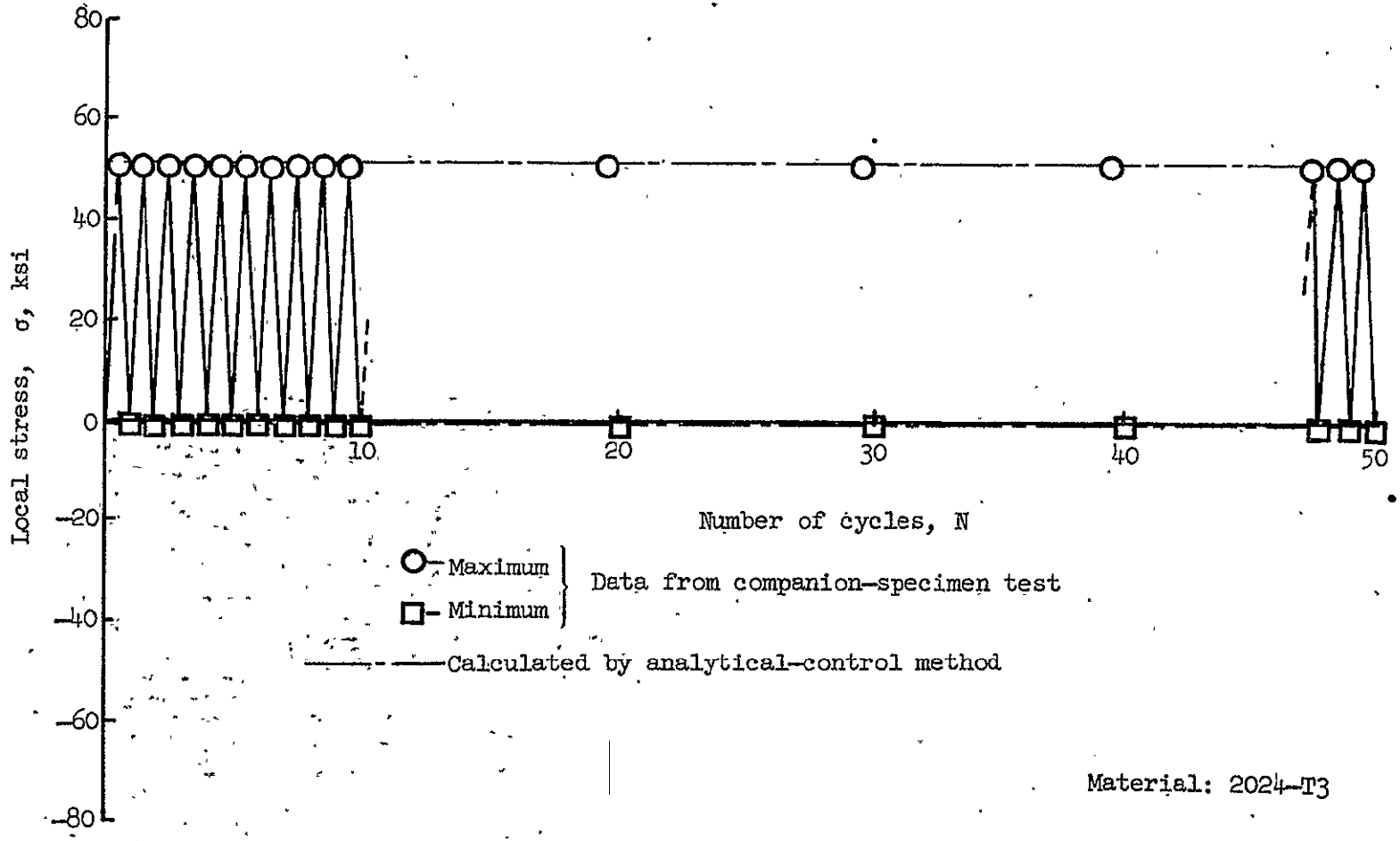

Figure 3.15 – Local stress history for constant-amplitude loading with S = 20 ksi and R = 0.

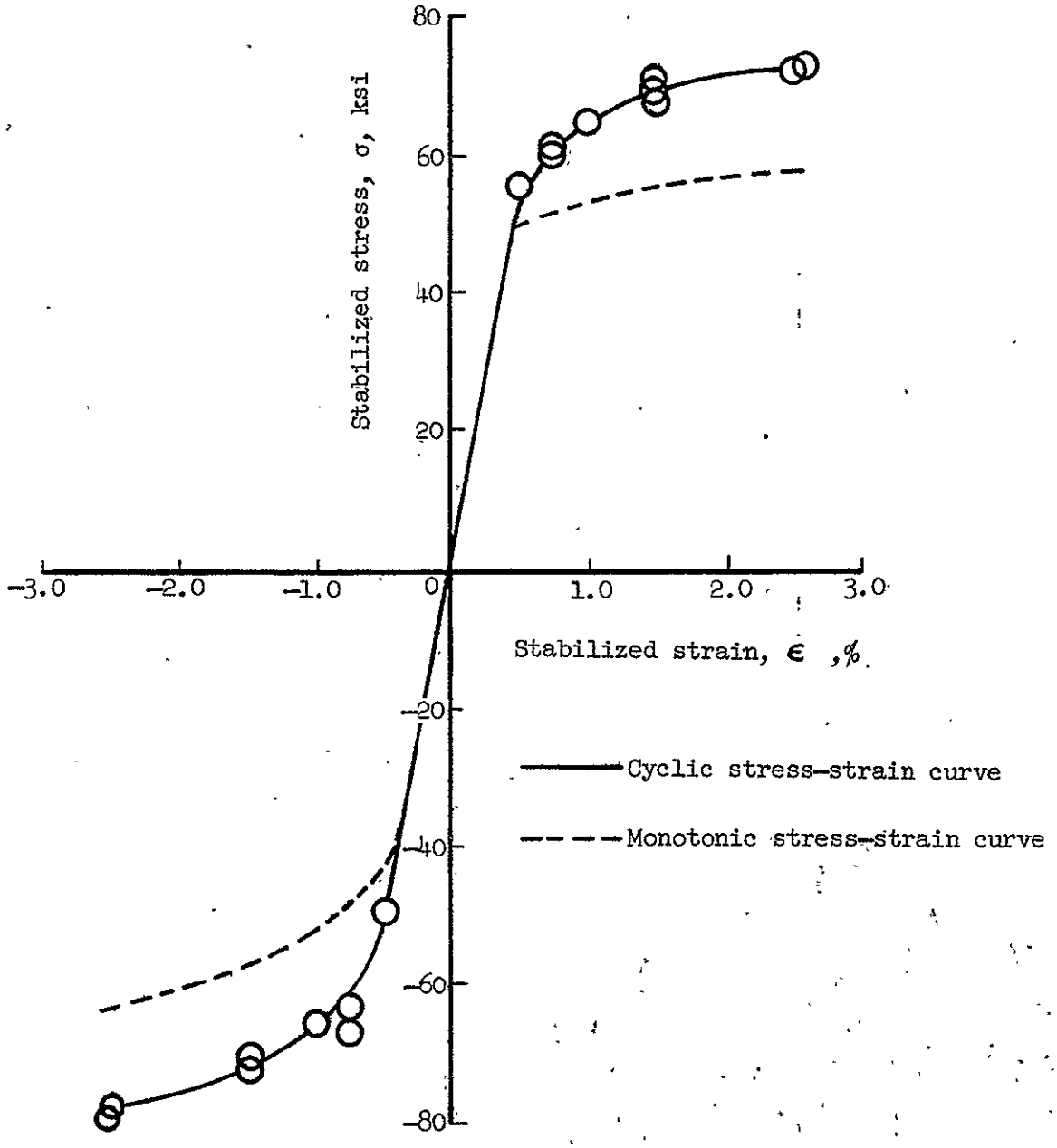

Figure 3.16 – Cyclic and monotonic stress–strain curves for 2024–T3 aluminum alloy.

Furthermore, the cyclic stress-strain curve, also presented in figure 3.16 (from [15]) indicated this local behavior to be stable for repeated cycling, which agrees with the results presented in figure 3.15. These results could have been calculated directly from figure 3.16. However, the companion-specimen test was conducted in the interest of completeness and also to assess the performance of the strain-coupled servo-control system. In addition, this local stress history for $S = 20$ ksi will be used as a reference in subsequent sections to describe the local effects of prior high loading on subsequent load cycling at $S = 20$ ksi. The local effects will in turn be used to explain the crack-initiation behavior during fatigue tests of the notched specimens.

The application of $S = 40$ ksi produced local reversed plasticity during each cycle as shown in figure 3.17. The cyclic strain-hardening behavior shown in figure 3.16 for 2024-T3 aluminum alloy was also evident in figure 3.17. The maximum and minimum local stresses increased initially with cycling but stabilized in about 10 cycles. Residual stresses decreased in magnitude corresponding to the increases in maximum and minimum stresses.

The strain history in figure 3.18 again illustrates that the local behavior for $S = 20$ ksi was both elastic and stabilized. The strain range in figure 3.19 for $S = 40$ ksi, however, decreased rapidly for the first few cycles before approaching a stabilized condition in about 10 cycles.

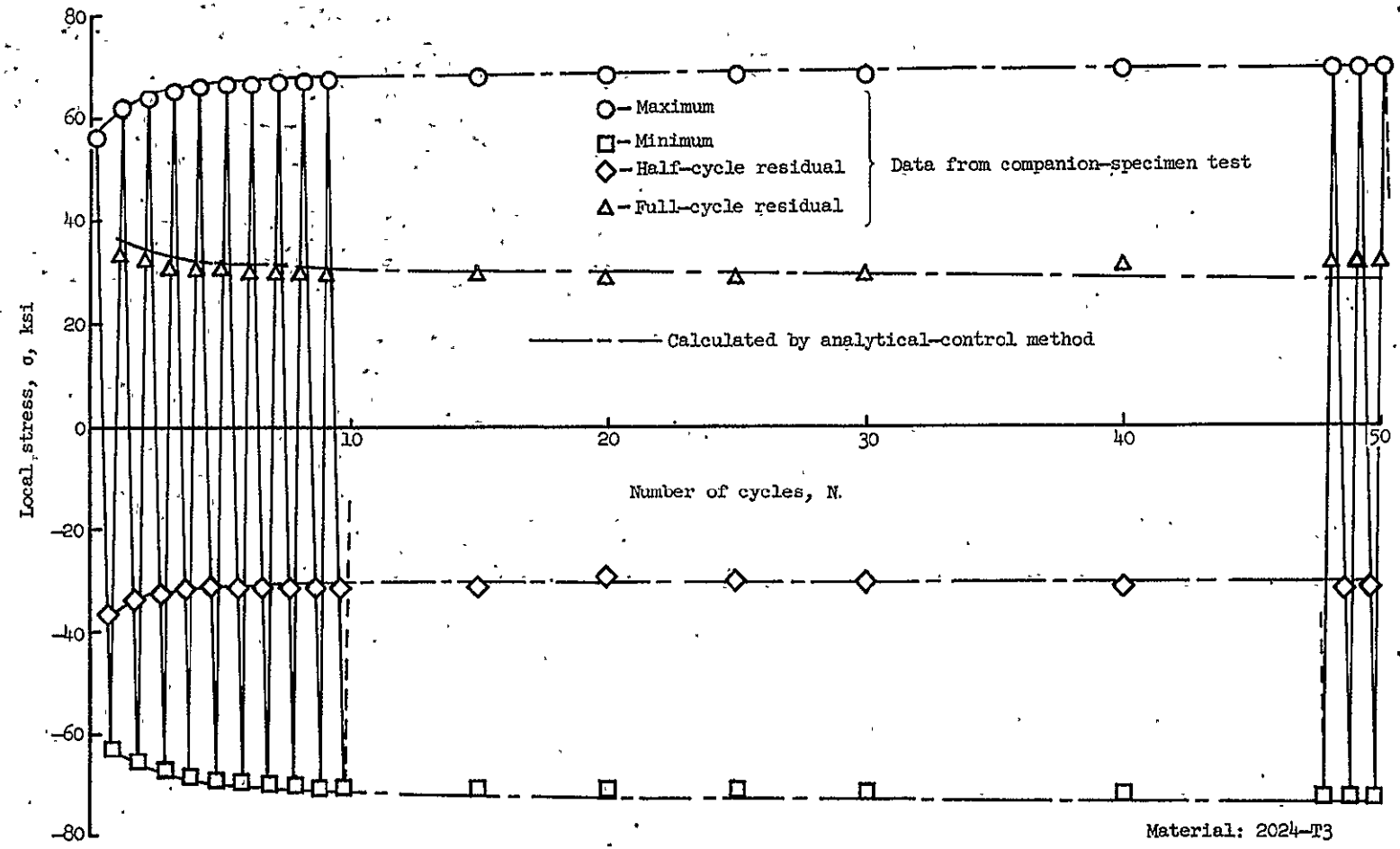

Figure 3.17 – Local stress history for constant-amplitude loading with S = 40 ksi and R = -1.

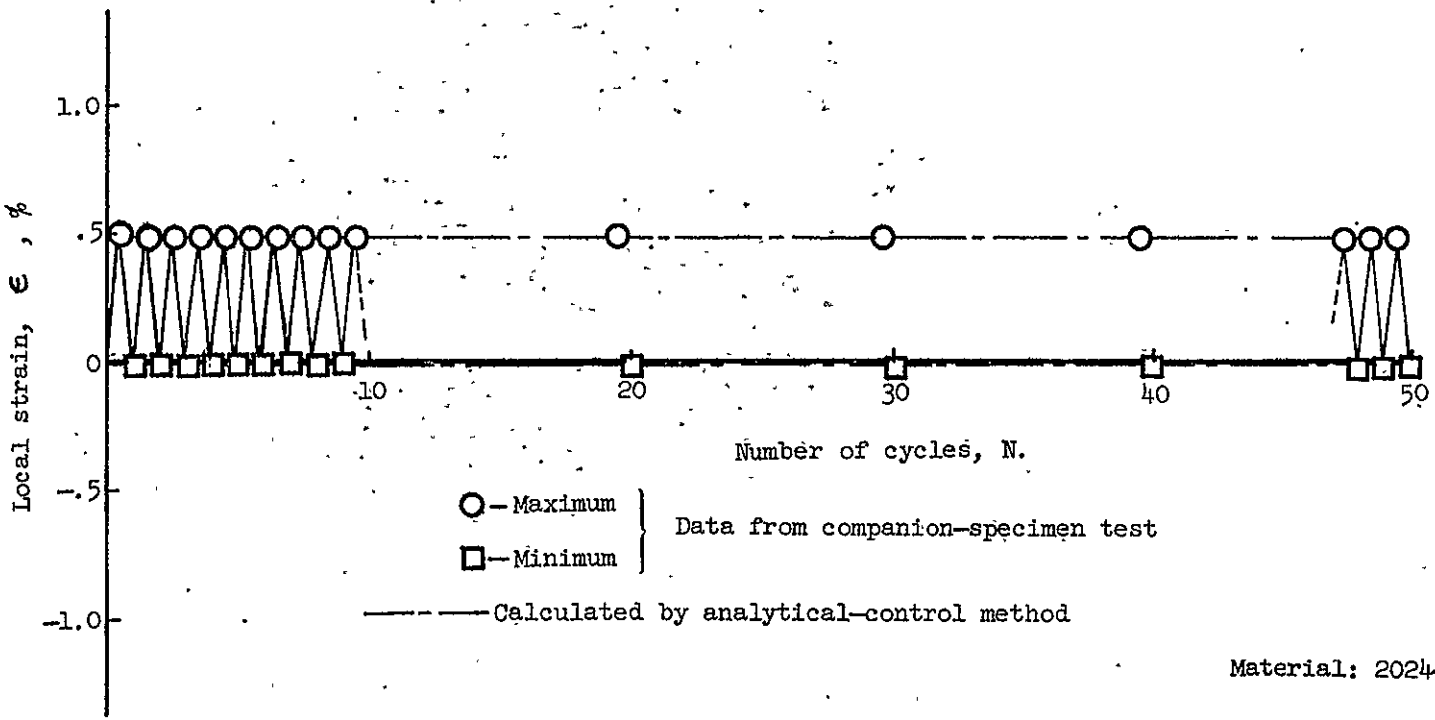

Figure 3.18 – Local strain history for constant-amplitude loading with S = 20 ksi and R = 0.

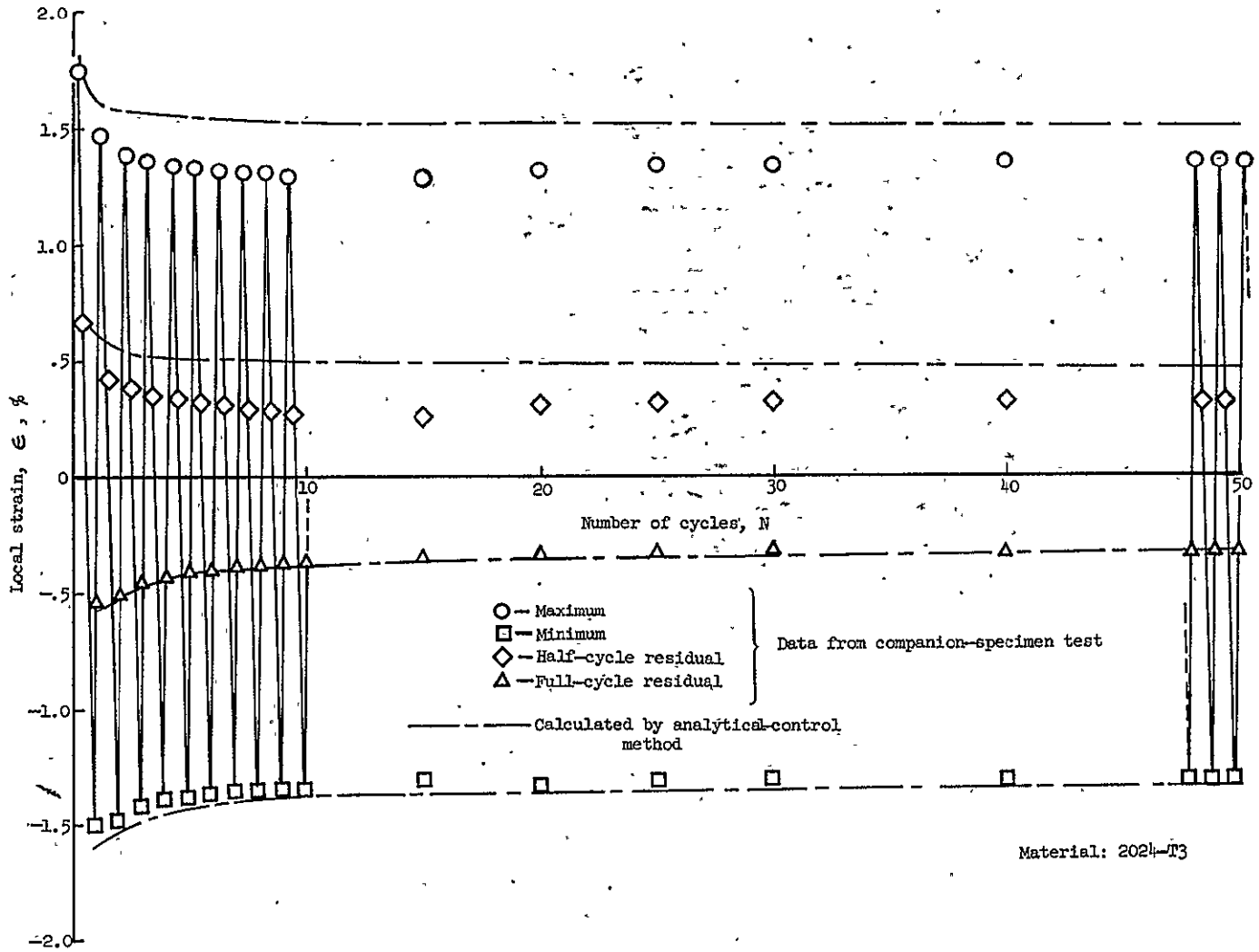

Figure 3.19 – Local strain history for constant-amplitude loading with S = 40 ksi and R = -1.

3.5.2 Variable Amplitude Loading

As previously mentioned in the discussion of the test program, the two constant-amplitude conditions were combined to form two distinct types of two-level loading. The high loading (S = 40 ksi) was applied first and was followed by load cycling at S = 20 ksi. The local plasticity produced by the high load cycling resulted in the creation of residual stresses that altered the local stress-strain conditions for subsequent low load cycling. The high loading was applied for 10 cycles and ended on both tensile and compressive half-cycles to produce, respectively, beneficial (compressive) and detrimental (tensile) residual stresses.

For the case of beneficial two-level loading a compressive residual stress of 30 ksi was left at the end of the high loading phase, figure 3.20. This residual stress acted as the minimum local stress during the second phase of loading, and decreased slightly during the first 40 cycles of loading at the low stress level. The maximum local stress corresponding to the loading at S = 20 ksi was initially 22 ksi, but also decreased slightly as the cycling was continued. This decrease in maximum and minimum stress shown in figure 3.20 was believed to be the result of strain-gage zero shift, and thought not to be representative of actual local stress behavior. This will be further discussed later in this report.

A tensile residual stress is shown in figure 3.21 for high loading ending in compression. For this case the minimum local stress was 7 ksi and the maximum local stress was 58 ksi for the cyclic loading at S = 20 ksi. Again for this case, a slight decrease occurred in extreme stresses as the cycling continued.

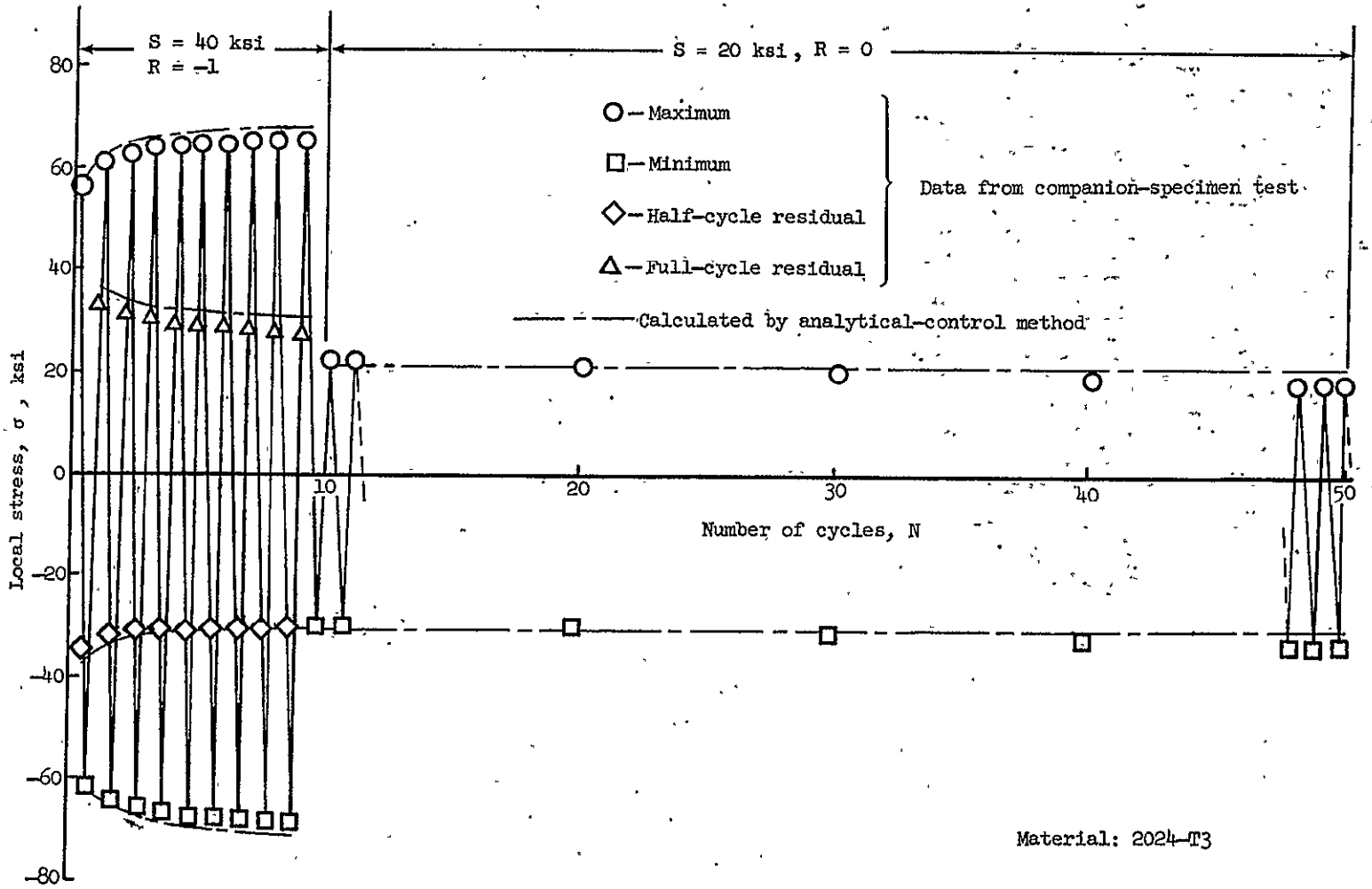

Figure 3.20 — Local stress history for beneficial prior loading.

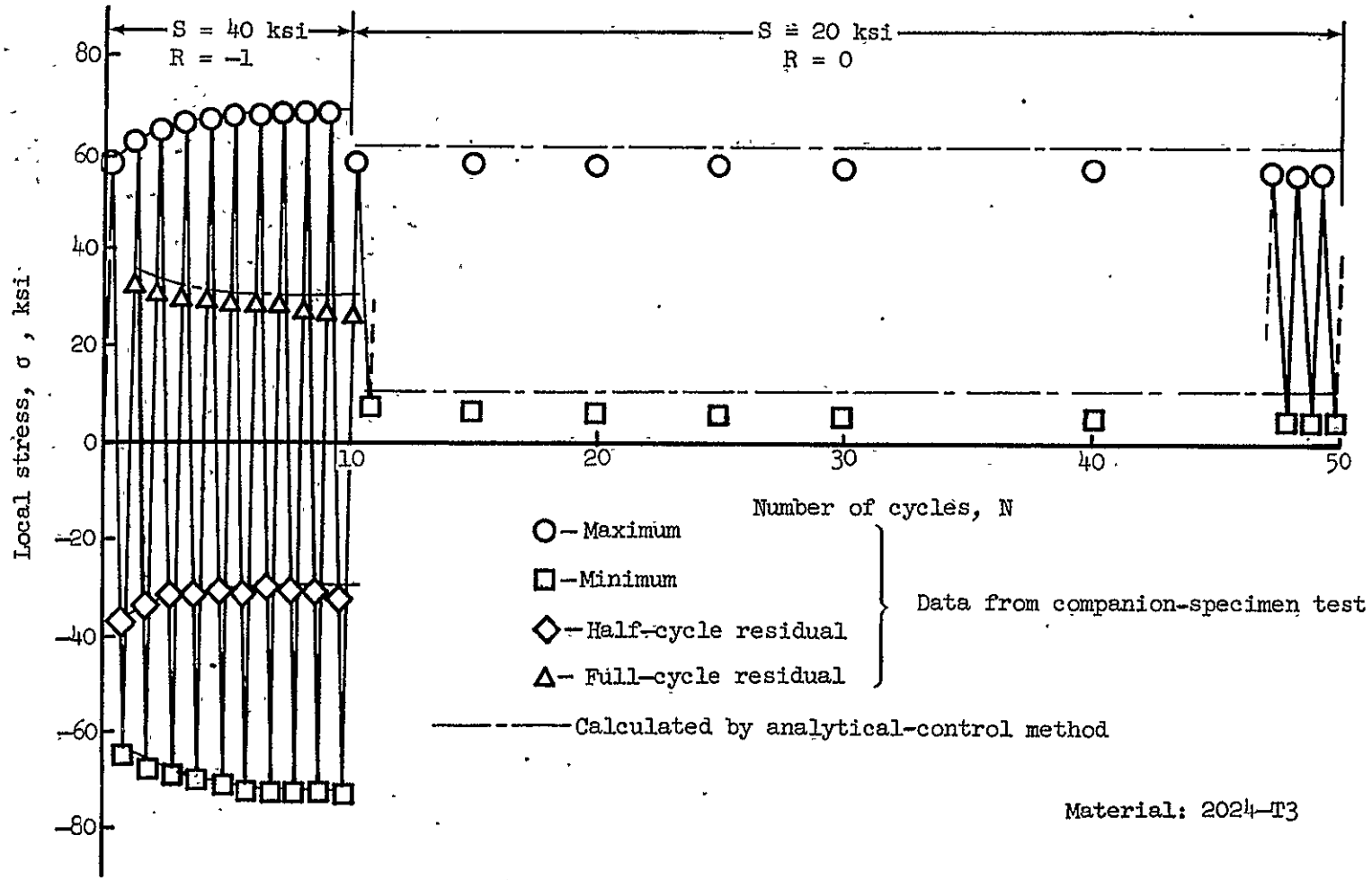

Figure 3.21 – Local stress history for detrimental prior loading.

The local strain histories for the two types of two-level loading are presented in figures 3.22 and 3.23. The local strain ranges decreased during the 10 cycles of high loading, but remained virtually unchanged for load cycling at the low stress level. The tensile residual strain at the end of 10 cycles in figure 3.22 produced the compressive residual stress shown in figure 3.20. Correspondingly, the compressive residual strain from figure 3.23 caused the tensile residual stress in figure 3.21.

Maximum and minimum local stresses and strains for the random stress sequence in figure 3.13 were determined by the companion-specimen method and are presented in figure 3.24. The notched specimen buckled under the first application of -50 ksi, in spite of the guide plates. For this reason the stress and strain histories were terminated after six cycles. Nevertheless, these experimental results are presented and will be used in the next section to assess the accuracy of the analytical-control method for random loadings.

3.6 Comparison of Calculated and Experimental Results

For an evaluation of the analytical-control method, this method was applied for each previously discussed loading condition to calculate the local stress-strain behavior from unnotched specimens. A typical recording of local stress-strain curves obtained by this approach are shown in figure 3.25. The calculations of local behavior by analytical control were continued for 50 cycles as in the companion-specimen tests. The calculated results are presented as local maximum, minimum, and residual stresses and strains for comparison with similar experimental data. The analytical-control results are represented by the dashed

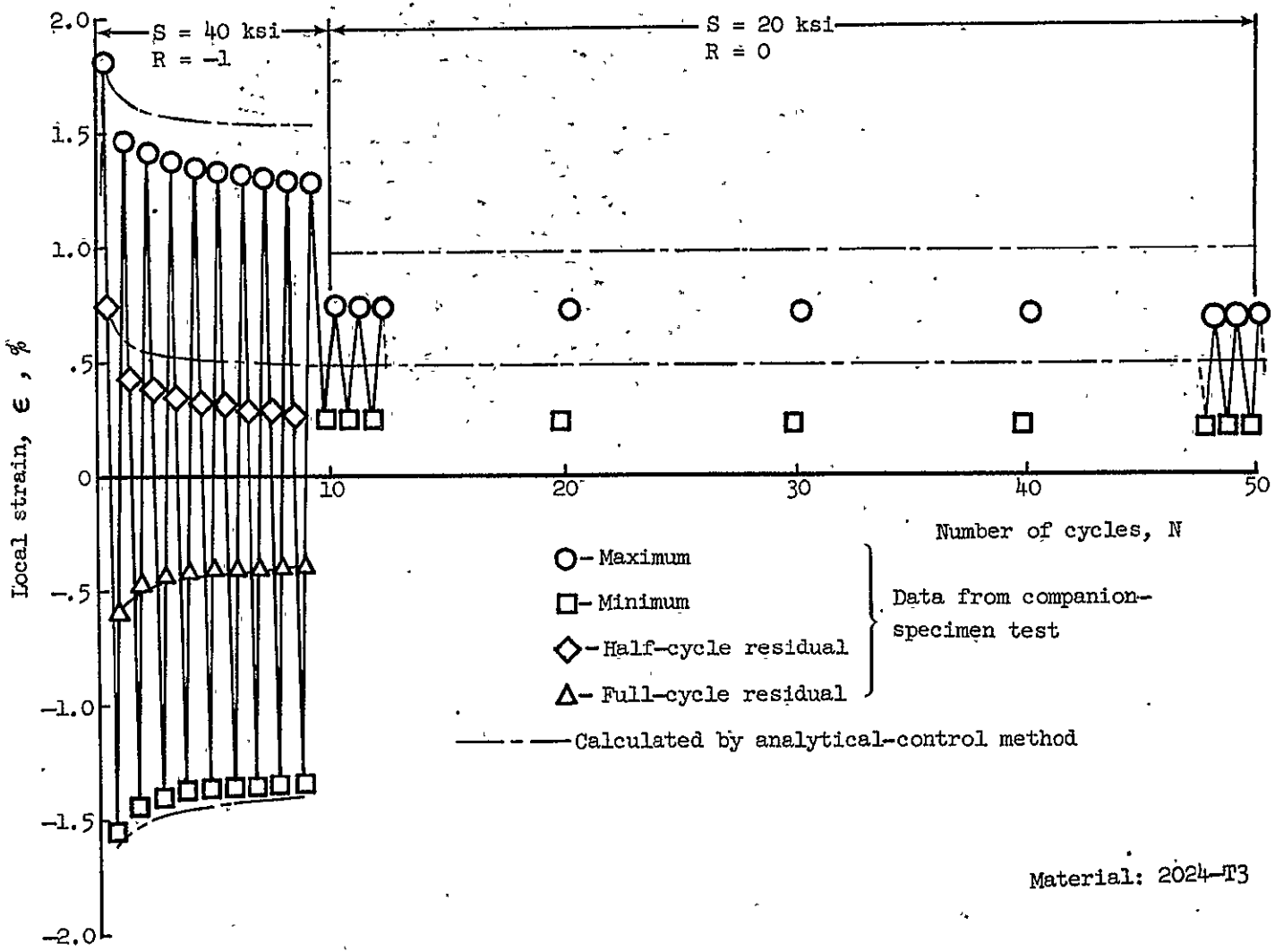

Figure 3.22 – Local strain history for beneficial prior loading.

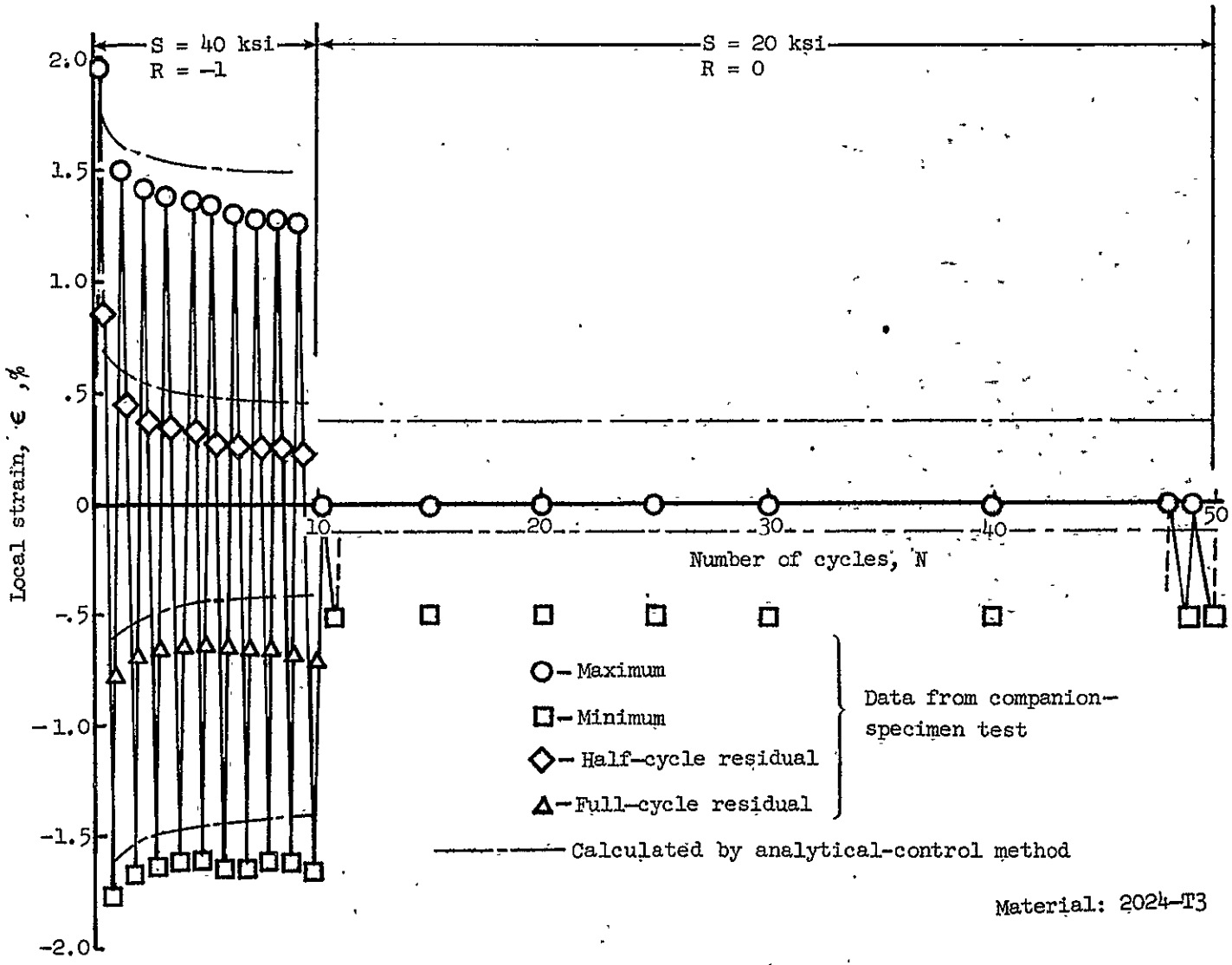

Figure 3.23 – Local strain history for detrimental prior loading.

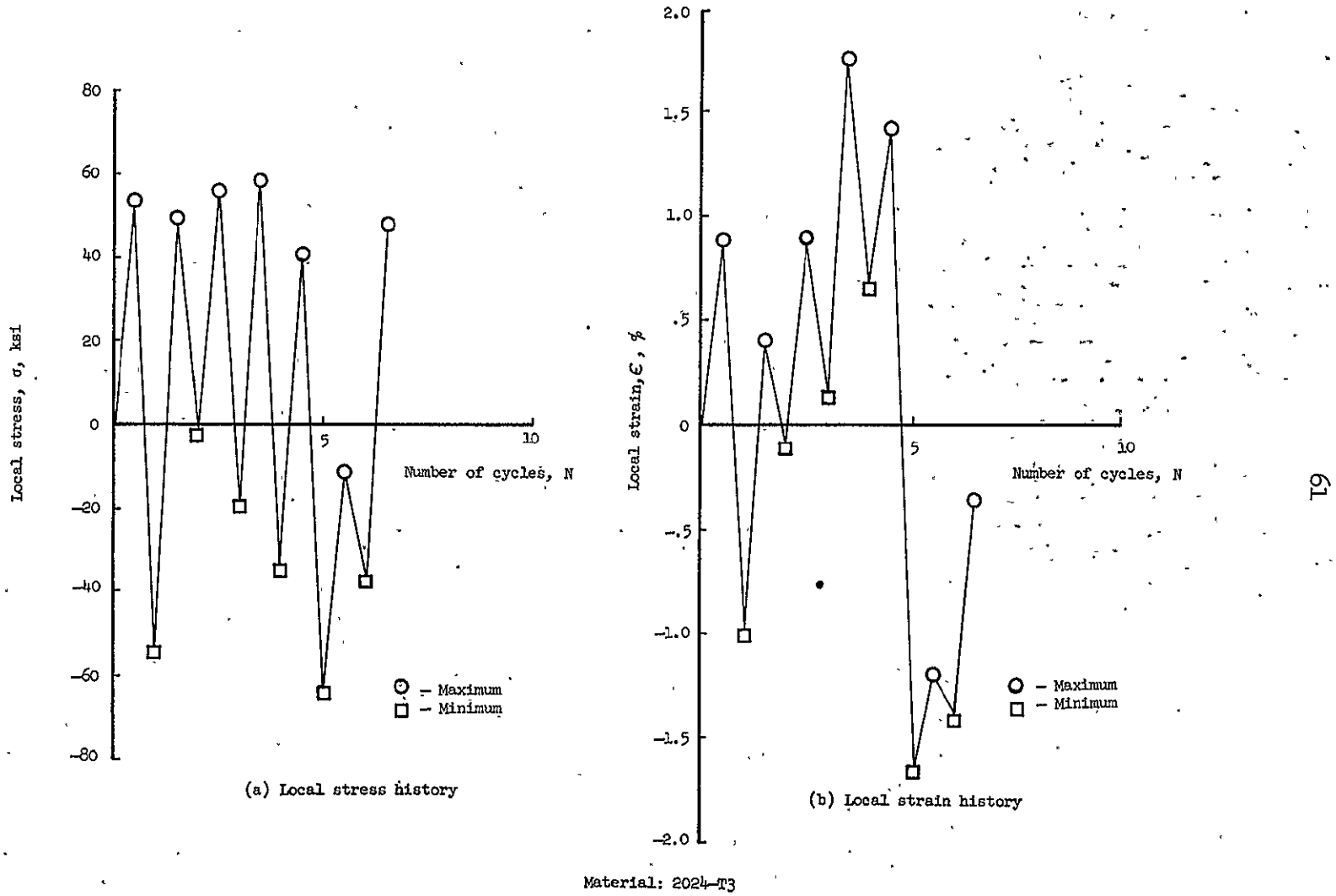

Figure 3.24 – Experimental local stress and strain histories for random nominal stress sequence.

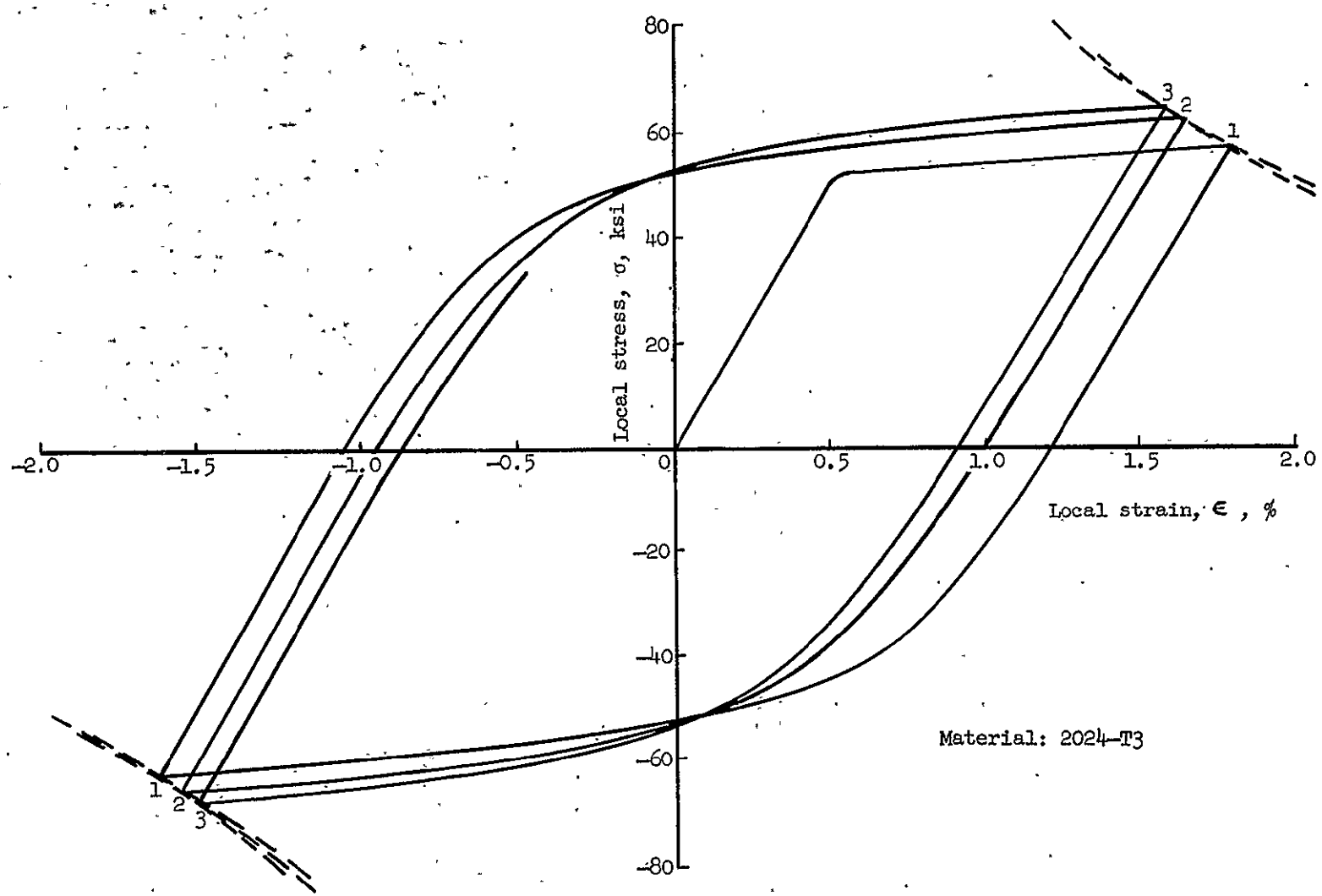

Figure 3.25 – Typical recording from analytical-control tests.

curves plotted together with the companion-specimen results in figures 3.15 and 3.17 through 3.23.

3.6.1 Constant-Amplitude Loading

The calculated local stress history for S = 20 ksi was entirely elastic, as expected, and agreed very closely with the corresponding experimental results in figure 3.15. This case, of course, did not represent a critical evaluation of the analytical-control method, but was studied to obtain a reference for local conditions for an evaluation of loading sequence effects during two-level loading. The constant-amplitude loading at S = 40 ksi provided a better test of the analytical-control approach. The calculated results for this case also correlate very well with data in figure 3.17. This correlation demonstrates the ability of the analytical-control method to account for local cyclic plasticity and to inherently incorporate the cyclic strain-hardening behavior in calculations of local cyclic stress.

As expected, the calculated and experimental strain histories for S = 20 ksi agreed closely, as illustrated in figure 3.18. In contrast, the calculated local strains in figure 3.19 for S = 40 ksi were somewhat in error.

3.6.2 Variable-Amplitude Loading

Local stress histories calculated for both types of two-level loading correlated remarkably well with the experimental results in figures 3.20 and 3.21. The stabilized calculated results for S = 20 ksi support the assumption that the slight decreases in local experimental stresses were due to small strain-gage errors. As in the case of

constant-amplitude loading, the calculated local strains were noticeably larger than the experimental values in figures 3.22 and 3.23. The maximum and minimum stresses and strains for the random loading sequence are presented in tables I and II. The corresponding experimental results from figure 3.24 are also listed in these tables and agree very well with the calculated results.

TABLE I.- COMPARISON OF CALCULATED AND EXPERIMENTAL LOCAL STRESSES FOR RANDOM NOMINAL STRESS SEQUENCE

Cycle Number	Maximum local stress, ksi		Minimum local stress, ksi	
	Analytical-control method	Companion-specimen method	Analytical-control method	Companion-specimen method
1	54.1	53.8	-55.3	-54.1
2	50.8	50.0	0.0	-2.0
3	56.1	55.8	-19.4	-19.8
4	58.1	58.6	-37.1	-34.8
5	38.7	41.2	-64.6	-63.9
6	-11.3	-10.9	-37.5	-37.7
7	48.8	48.3	-67.0	(specimen
8	55.6		-67.0	buckled)
9	11.7		-67.0	
10	21.0		-67.0	
11	65.0		-10.5	
12	15.3		-69.0	
13	58.1		-41.2	
14	63.0		-64.6	
15	67.0		-50.0	
16	50.0		-75.1	
17	69.4		-77.1	
18	58.1		-64.6	
19	67.0		-75.9	
20	47.2		+21.0	
21	70.2		-61.3	
22	70.2		-72.6	
23	69.4		-73.0	
24	29.9		+4.0	
25	71.0		-46.0	
26	29.9		-67.0	
27	70.2		-67.8	
28	52.5		+26.6	
29	70.2		-71.8	
30	48.4		-0.8	

TABLE II.- COMPARISON OF CALCULATED AND EXPERIMENTAL LOCAL STRAINS FOR RANDOM NOMINAL STRESS SEQUENCE

Cycle Number	Maximum local stress		Minimum local stress	
	Analytical-control method	Companion-specimen method	Analytical-control method	Companion-specimen method
1	1.07	0.89	-1.06	-1.01
2	0.47	0.40	-0.03	-0.11
3	1.00	0.89	0.25	0.13
4	1.57	1.75	0.49	0.65
5	1.24	1.42	-1.80	-1.66
6	-1.33	1.19	-1.56	-1.42
7	-0.38	-0.36	-2.37	(specimen
8	-0.50		-2.37	buckled)
9	-1.64		-2.37	
10	-1.55		-2.37	
11	1.54		0.75	
12	1.00		-1.71	
13	0.11		-0.95	
14	0.60		-1.23	
15	1.92		0.54	
16	1.57		-2.55	
17	1.94		-2.50	
18	-0.81		-2.11	
19	0.29		-2.60	
20	-1.31		-1.55	
21	1.67		-0.10	
22	1.67		-1.23	
23	1.69		-1.22	
24	-0.20		-0.45	
25	2.98		-1.61	
26	2.37		0.70	
27	2.99		0.73	
28	2.07		1.82	
29	3.13		0.28	
30	1.57		1.04	

4. CRACK INITIATION AT STRESS CONCENTRATIONS

4.1 General

The analysis of fatigue in service is usually extremely complex as a result of the very localized nature of fatigue. Fatigue cracks initiate at the most severely stressed area of a machine part or structure and this area of high stress concentration is characteristically very small. A prediction of fatigue behavior must be based upon the fatigue behavior of this highly stressed local zone. In addition, fatigue predictions must account for the growth behavior of cracks that originate and grow from this local zone, but in this chapter attention is focused on crack initiation.

In principle, fatigue crack initiation at a stress concentration can be predicted by calculating local stresses for each cycle of loading and by estimating the corresponding "local" fatigue damage from a cumulative damage theory and a fatigue crack-initiation diagram for unnotched specimens. This approach is complicated by local plasticity and attendant residual stresses, by interactions of one local stress level with the damage caused at another local stress level, and by a size effect.

Local plasticity and the resulting residual stress behavior were illustrated in figures 3.20 and 3.21 and discussed in the previous chapter. From a fatigue point of view, residual stresses influence local damage-accumulation rates by altering local mean stresses. Because fatigue damage increases with mean stress, the prior loading in figure 3.21 should have a detrimental influence on the local fatigue

behavior under S = 20 ksi loading. On the other hand, the prior loading for figure 3.20 should improve the fatigue performance under the low level. These nominal stress-interaction effects may be accounted for only by accurate calculations for local stresses. As indicated in Chapter 2, such calculations are quite complicated and, as a result, approximate methods are usually required.

In addition to the stress interaction due to residual stresses, a second type of stress interaction is produced by damage acceleration. Dolan and Corten [43] and Manson, Freche, and Ensign [44] described damage acceleration in terms of microscopic crack initiation caused by a high stress level that enabled low stress cycles to readily propagate the initiated microcrack. A considerable fraction of the life would be required in constant-amplitude cycling at the low stress level to create a similar microcrack. Consistent with this explanation, a few high stress cycles have been observed to noticeably accelerate the damage accumulation for subsequent cycling at a lower stress level. Freudenthal and Heller [45] described damage acceleration in terms of the increased crack-propagation rate at each stress level caused by interaction with all higher stress levels. In both explanations damage acceleration was related to microscopic plastic deformation at the high stress that enabled the lower stresses to do more damage than they could otherwise do.

Both types of stress interaction were simulated in unnotched specimens by the analytical-control procedure from Chapter 3. By continuing an analytical-control test until fatigue cracks initiate,

these interaction effects can be automatically incorporated into the resulting estimate for fatigue crack initiation. Furthermore, the fatigue damage accumulation in the unnotched specimen simulates that for the material at the notch root, eliminating the need for a cumulative fatigue damage theory. Estimates of crack-initiation periods were found by this analytical-control approach and are compared with data in this chapter.

The analytical-control procedure for estimating crack initiation does not account for the size effect that causes $K_f \leq K_T$. This size effect results from the fact that when local stress is simulated in unnotched specimens, a large volume of material is highly stressed, although only a small volume is similarly stressed at the actual stress-concentration site. From a statistical point of view, the large volume of material in the unnotched specimens contains a larger microscopic flaw than the smaller volume at the stress-concentration site. This larger flaw in the unnotched specimen grows to a macroscopic size faster than the smaller flaw at the stress concentration and, as a result, for the same stress history, the crack-initiation period for the unnotched specimen is shorter than for the stress concentration. Wetzel [24] replaced K_f by K_T in the Neuber equation (9) to account for this size effect and consequently, to improve fatigue estimates. Although for cases of constant-amplitude, Wetzel has improved estimates of crack initiation. This approach leads to large discrepancies between simulated and actual local stresses, especially for high stress-concentration factors where K_f is usually significantly smaller

than K_T. These discrepancies in local stress would alter both of the previously explained stress interactions for variable-amplitude loading. For this reason no correction was made for size effect in the present study.

4.2 Observed Crack-Initiation Periods

The sheet specimens containing a central hole from Chapter 3 were tested under fatigue loading until fatigue cracks developed at the stress-concentration site. Tests were conducted for the two levels of constant-amplitude loading and the two combinations of two-level loading considered in Chapter 3.

Microscopic cracks usually develop at an early stage of fatigue life. However, a considerable fraction of the total fatigue is often required to propagate these small cracks to a macroscopic size. From an engineering point of view, very small cracks (that do not alter the load carrying capacity of a structural member) may be ignored. From this point of view, the crack-initiation life is often defined as the number of cycles required to produce a macroscopic crack, detectable by conventional inspection methods. For the present study, crack-initiation life was defined as the number of cycles necessary to create a 0.03-inch crack at the stress-concentration site. This "initial" crack size of 0.03 inch was selected from crack propagation considerations (see section 5.2), but nevertheless, is representative of the minimum size detectable by inspection methods currently in service.

Because of difficulties in direct detection of small cracks (0.03 inch) at the stress-concentration site for each fatigue test, an

indirect approach was used to establish crack-initiation lives. The total fatigue life, N_f, of notched specimens was assumed to consist of two parts: the number of cycles required to produce the 0.03-inch crack, N_o, and the number of cycles necessary to propagate this crack to failure, N_{cp}. As part of the crack propagation study in Chapter 5, N_{cp} was experimentally determined for the notched specimen configuration for each loading sequence used in the present study of crack initiation. For each fatigue test in this chapter, the crack-initiation life, N_o, was found by subtracting the corresponding constant value of N_{cp} from the observed total life, N_f. These N_{cp} values were: 4000 cycles for the case of no prior loading (S = 20 ksi), 34,000 cycles for beneficial prior loading, and 3000 cycles for detrimental prior loading. Errors associated with the assumption of a constant N_{cp} value for each test condition were believed to be small, since for all test conditions these N_{cp} values were less than 5.6 percent of the corresponding geometric mean values of N_f.

Total fatigue lives and the corresponding crack-initiation periods are presented in table III and figure 4.1 for each of the four test conditions. In all tests cracks are initiated at the zone of highest stress concentration. In addition to 12-inch-wide specimens, 4-inch-wide specimens were used as indicated in table III and illustrated in figure 4.1 by open symbols. The constant-amplitude loading conditions resulted in initiation lives with geometric means of 331 cycles for S = 40 ksi and 129,000 cycles for S = 20 ksi. The high-low combinations of these two stress levels produced different fatigue lives.

TABLE III.- FATIGUE CRACK-INITIATION DATA FOR NOTCHED SPECIMENS

Test condition	Notched specimen number(a)	Fatigue life, N_f, cycles	Crack initiation life,(b) N_o, cycles	Geometric mean of crack initiation lives, N_o, cycles
S = 40 ksi R = -1 (N_{cp} = 12 cycles)	108-1 98 112-2	300 312 427	288 300 415	331
S = 20 ksi R = 0 (N_{cp} = 4000 cycles)	93 103 108 112 93-1 103-1 103-3	94,700 78,000 144,700 118,300 189,600 157,900 190,000	90,700 74,000 140,700 114,300 185,600 153,900 186,000	129,000
Beneficial prior loading (N_{cp} = 34,000 cycles)	100 102 93-3 112-3 93-4 97-4 108-2	267,300 303,100 590,200 910,000 1,003,100 1,063,000 1,071,000	233,300 269,100 556,200 876,000 969,100 1,029,000 1,037,000	610,000
Detrimental prior loading (N_{cp} = 3000 cycles)	97-1 109 108-4 112-1 93-3	54,200 65,000 66,000 77,300 78,000	51,200 62,000 63,000 74,300 75,000	65,400

(a)Hyphenated numbers indicate 4-inch-wide specimens with 0.672-inch-diameter hole.

(b)Crack-initiation lives found by subtracting crack propagation period N_{cp} (see first column) from total life N_f.

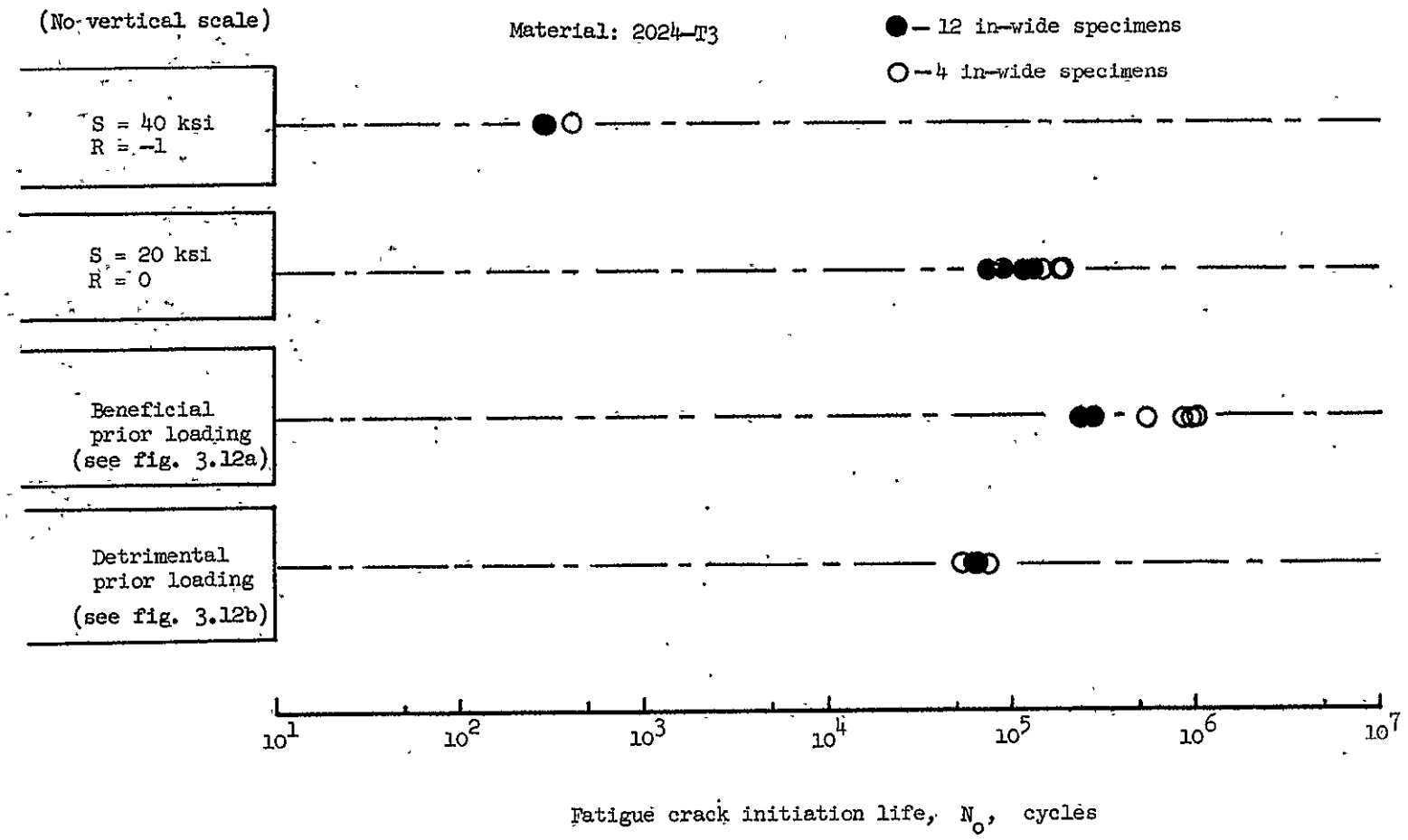

Figure 4.1 – Observed crack initiation behavior for notched specimens.

As expected from the analysis of local stress-strain conditions, the loading sequence in figure 3.12(a) resulted in a fatigue life larger than the reference case of constant-amplitude loading, while the sequence in figure 3.12(b) produced a shorter life. That is, the prior loading in figure 3.12(a) was beneficial and the prior loading in figure 3.12(b) was detrimental. To emphasize this stress interaction the linear cumulative damage rule (ref. 29)

$$\sum_{i=1}^{M} \frac{n_i}{N_i} = 1 \tag{18}$$

was applied where M is the number of stress levels, n_i is the number of applied cycles for the ith stress level, and N_i is the constant-amplitude fatigue life for that stress level. For the case of beneficial prior loading

$$\sum_{i=1}^{2} \frac{n_i}{N_i} = \frac{n_1}{N_1} + \frac{n_2}{N_2} = \frac{10}{331} + \frac{610,000}{129,000} = 4.77$$

and for detrimental prior loading

$$\frac{n_1}{N_1} + \frac{n_2}{N_2} = \frac{10}{331} + \frac{65,400}{129,000} = 0.53$$

These results illustrate the nonlinear damage accumulation caused by residual stresses not accounted for by the linear cumulative damage rule. The difference in the last half-cycle of prior loading for these two cases (compare figs. 3.12(a) and 3.12(b)) caused approximately an

order of magnitude difference in crack-initiation lives. For service loading sequences, which in many cases are similar to the random sequence of loads in figure 3.13, residual stresses are being created and eliminated throughout the entire crack-initiation life. Fatigue predictions for such cases must be based on the analysis of local stress-strain conditions to account for the complex residual stress effects. The application of the linear cumulative damage rule based on nominal stresses leads to meaningless results for these service loading conditions.

4.3 Prediction of Fatigue Crack Initiation

To obtain estimates of crack-initiation periods for the notched specimen, the analytical-control procedure presented in Chapter 3 was continued until the unnotched specimens failed in fatigue. As previously illustrated (figs. 3.17, 3.20, and 3.21), local stress-strain conditions stabilize for repeated load cycling. For convenience, after stabilization occurred the testing procedure was changed from analytical control to stress control and continued in the stress control mode until failure occurred. Since crack-initiation life for the notched specimens was defined as the number of cycles required to produce a 0.03-inch crack, these tests with unnotched specimens should have been continued until a crack of this same size developed. However, preliminary tests showed that these unnotched specimens failed statically for small crack lengths, comparable to the 0.03-inch "initial" size crack. Consequently, for convenience crack propagation was not monitored in these tests, and the estimates for crack-initiation lives

were taken as the number of cycles for complete failure of the unnotched specimens.

The errors introduced in N_o predictions by these simplifying assumptions were believed to be small compared to the effects of load interaction. Both the residual stress and the damage acceleration stress interactions were accounted for by the analytical-control fatigue tests. It is believed only the unaccounted for size effect resulted in significant errors.

Analytical-control tests were conducted for the four test conditions and resulting estimates for N_o are presented in table IV and figure 4.2. The beneficial and detrimental effects of residual stress are reflected by the results in figure 4.2. These results are further discussed in the next section and are compared with the observed crack-initiation periods.

4.4 Comparison of Predicted and Observed Results

For an assessment of the accuracy of the analytical-control method for estimating fatigue, the observed and predicted results from figures 4.1 and 4.2 were combined in figure 4.3. The predicted crack-initiation periods reflect the general trends displayed by the observed results, however, the previously mentioned size effect and stress interactions combine to produce conservative predictions. These effects are each briefly discussed in the following analysis of the discrepancies between predicted and observed crack-initiation periods.

The analytical-control method as presented in this report does not account for the size effect on the fatigue crack-initiation behavior.

TABLE IV.- PREDICTED CRACK-INITIATION PERIODS FROM ANALYTICAL-CONTROL TESTS WITH UNNOTCHED SPECIMENS

Test condition for notched specimen	Unnotched specimen number	Fatigue life from analytical-control tests, cycles	Geometric mean of fatigue lives, cycles
S = 40 ksi R = -1	B53 E51 D52	96 166 232	155
S = 20 ksi R = 0	G53 G51 N53 112-A L51	19,200 22,700 43,500 48,100 58,400	35,100
Beneficial prior loading	M51 A53 F53	140,000 181,000 273,300	191,000
Detrimental prior loading	C51 D51 F51	17,300 23,100 28,800	22,400

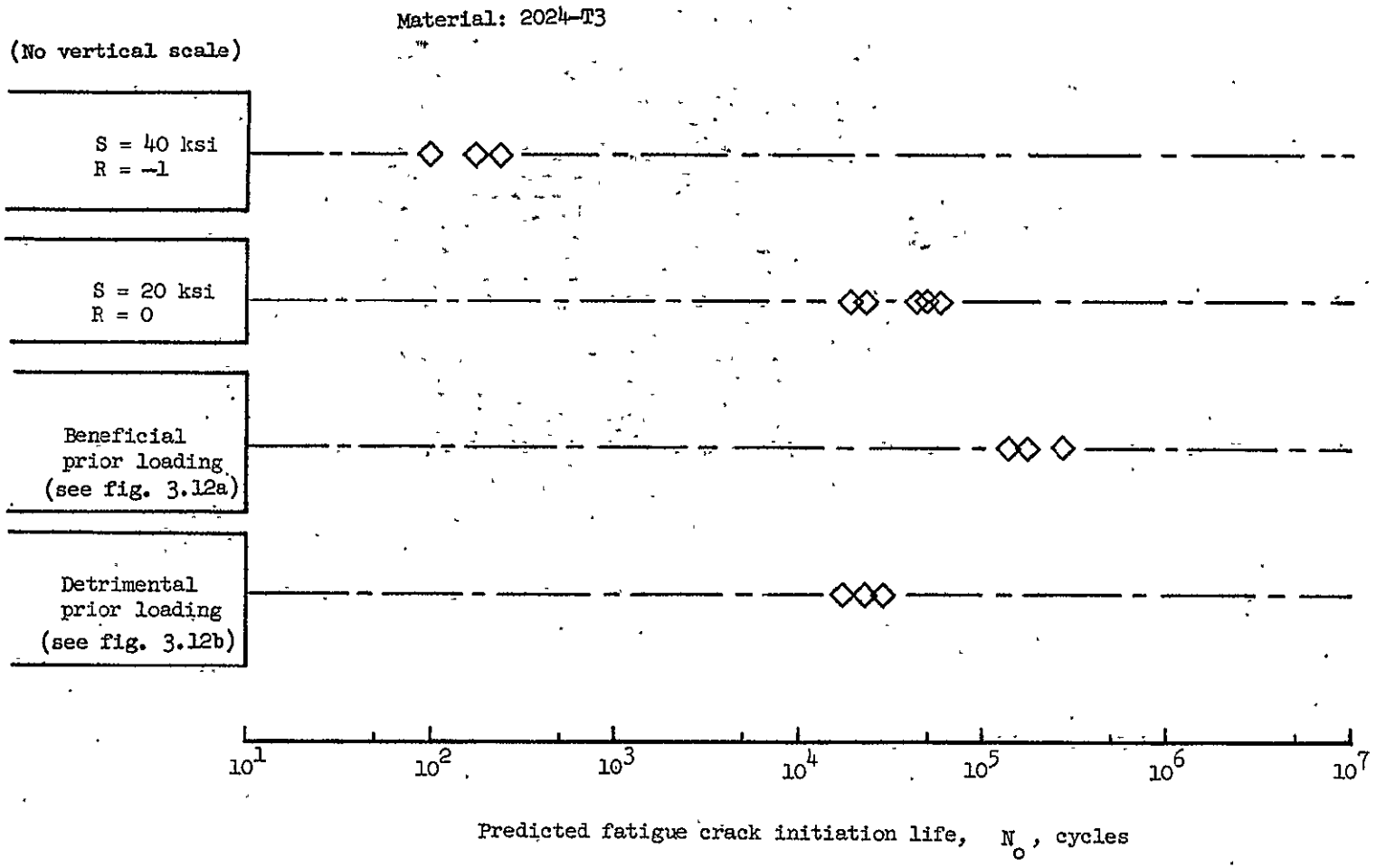

Figure 4.2 – Predicted fatigue crack initiation periods for notched specimens.

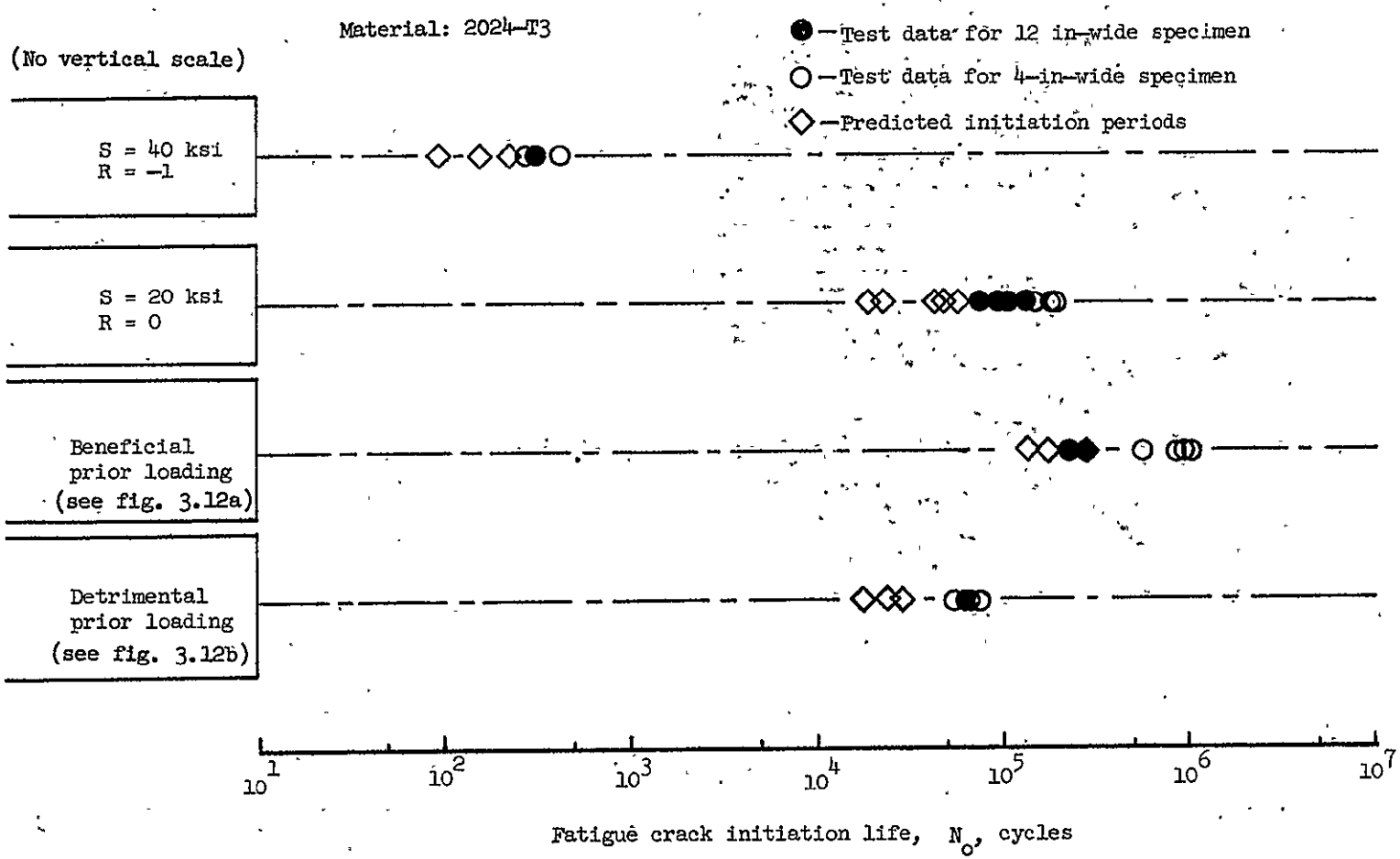

Figure 4.3 — Comparison of predicted and observed crack initiation periods.

The unnotched specimens used to estimate N_o contained a much larger volume of highly stressed material than notched specimens with the result that observable fatigue cracks initiated earlier in the unnotched specimens, as previously explained. This effect is attenuated somewhat by local plasticity because a larger volume of material (within the local plastic zone) experiences the high local stress. This trend was present in the predicted N_o values in figure 4.3 for constant-amplitude loading. The estimate of N_o for $S = 20$ ksi was approximately one-fourth the corresponding observed value (see tables III and IV for actual values). In contrast, the estimate for $S = 40$ ksi, which produced local plasticity, was nearly one-half the observed N_o. To illustrate the effect of plasticity on the size of the highly stressed local zone, the elastic stress distribution in figure 3.2 was used in equation (11) together with the stress-strain curve in figure 3.16 to obtain the stress distributions in figure 4.4. The stress distributions in figure 4.4 for prior loading show that the size effect should also be diminished for both cases of two-level loading. For these two test conditions the predicted N_o values were approximately one-third as large as the observed N_o values (see fig. 4.3 and tables III and IV).

The size effect is usually expressed in terms of K_f, the ratio of fatigue stresses for unnotched and notched specimens at a given fatigue life. Auxiliary fatigue tests were conducted with unnotched specimens to establish the value of K_f for this study. Results from these tests are listed in table V and are plotted in figure 4.5 to create a segment

TABLE V.- FATIGUE LIVES FOR CONSTANT-AMPLITUDE TESTS OF UNNOTCHED SPECIMENS

Constant-amplitude test conditions for unnotched specimens		Unnotched specimen number	Fatigue life, cycles	Geometric mean of fatigue lives, cycles
Maximum stress, ksi	Minimum stress, ksi			
40.0	0	C53 K52 112-B	166,600 187,000 293,200	211,000
45.0	0	M53 I53 103-B	83,800 128,800 137,000	115,000
51.5	0	G53 G51 N53 112-A L51	19,200 22,700 43,500 48,100 58,400	35,100
21.3	-30.1	K53 J53 I51	270,900 276,900 361,700	302,000
61.1	+10.5	H51 J51 I52	28,300 32,400 34,600	31,600

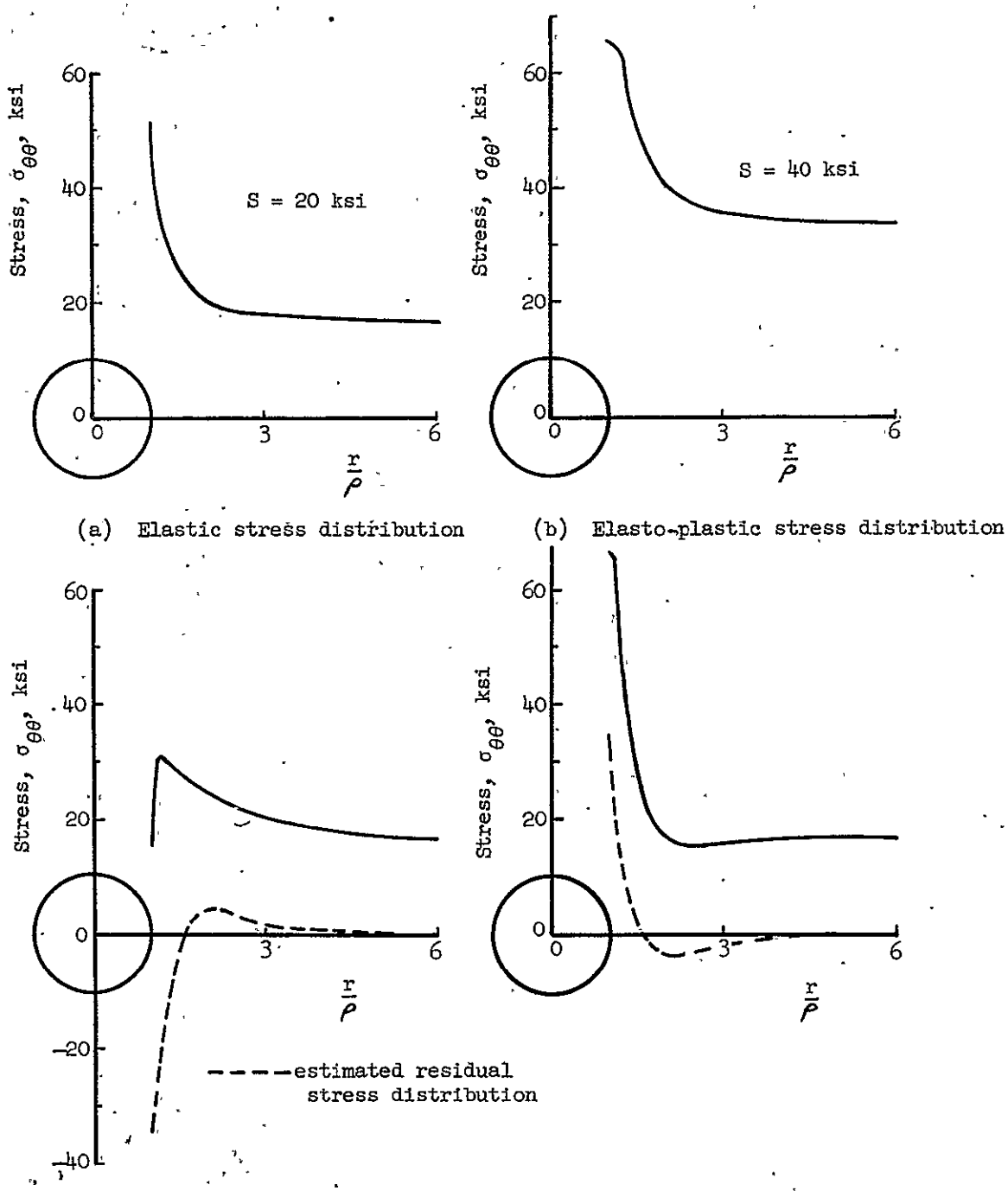

Figure 4.4 – Stress distributions on transverse axis.

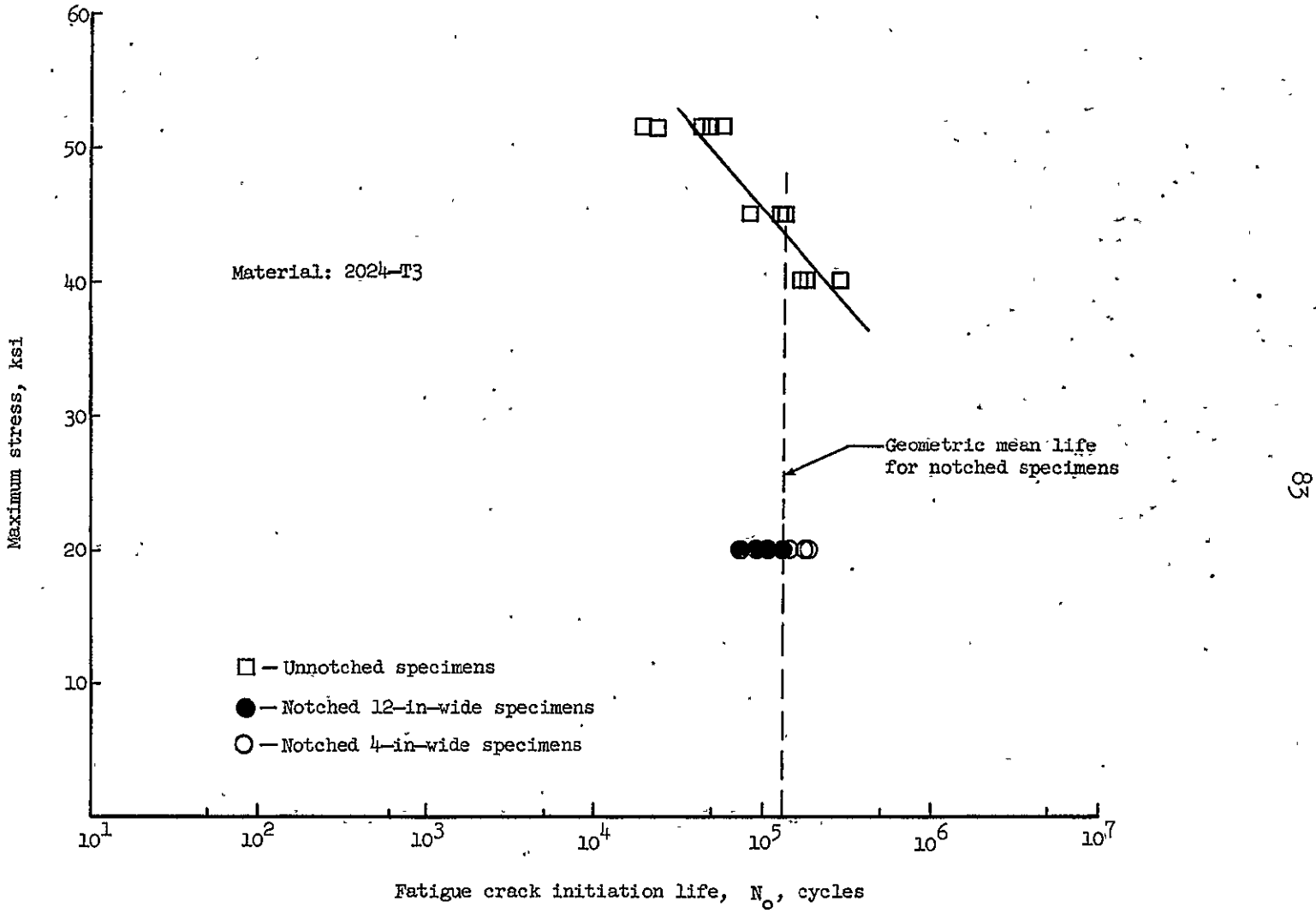

Figure 4.5 – Comparison of crack initiation lives for notched and unnotched specimens.

of the S-N curve for unnotched specimens. On this curve a stress of 43.5 ksi corresponds to the geometric mean of the lives for notched specimens at $S = 20$ ksi. The ratio of stresses at this life yields $K_f = 2.18$ in contrast to $K_T = 2.57$ from Chapter 3. This value of K_f could have been used in equation (10) in place of K_T to improve estimates of N_o for constant-amplitude tests as suggested by Wetzel [24], however, this substitution would have introduced noticeable errors in the local stress-strain calculations for the cases of two-level loading. These errors probably would not have seriously affected the N_o estimates for the present study because the above K_f is 85 percent of K_T. However, for high K_T values, the difference between K_f and K_T is usually quite large and Wetzel's approach would be unacceptable for variable-amplitude loading, because of inappropriate stress-interaction effects. A general correction procedure for the size effect must be accomplished through appropriate adjustments of the estimated N_o found by cycling unnotched specimens through the most accurate local stress (or strain) sequence obtainable.

To enable an evaluation of the effects of stress interactions on the analytical-control tests, additional constant-amplitude test results in table V and figure 4.6 were obtained. These tests were designed to illustrate separately the residual stress effect and the damage acceleration effect. Unnotched specimens were cycled between the constant-amplitude local stress limits corresponding to $S = 20$ ksi for the two-level tests to directly assess the effects of residual stress. These stress limits were determined from analytical-control

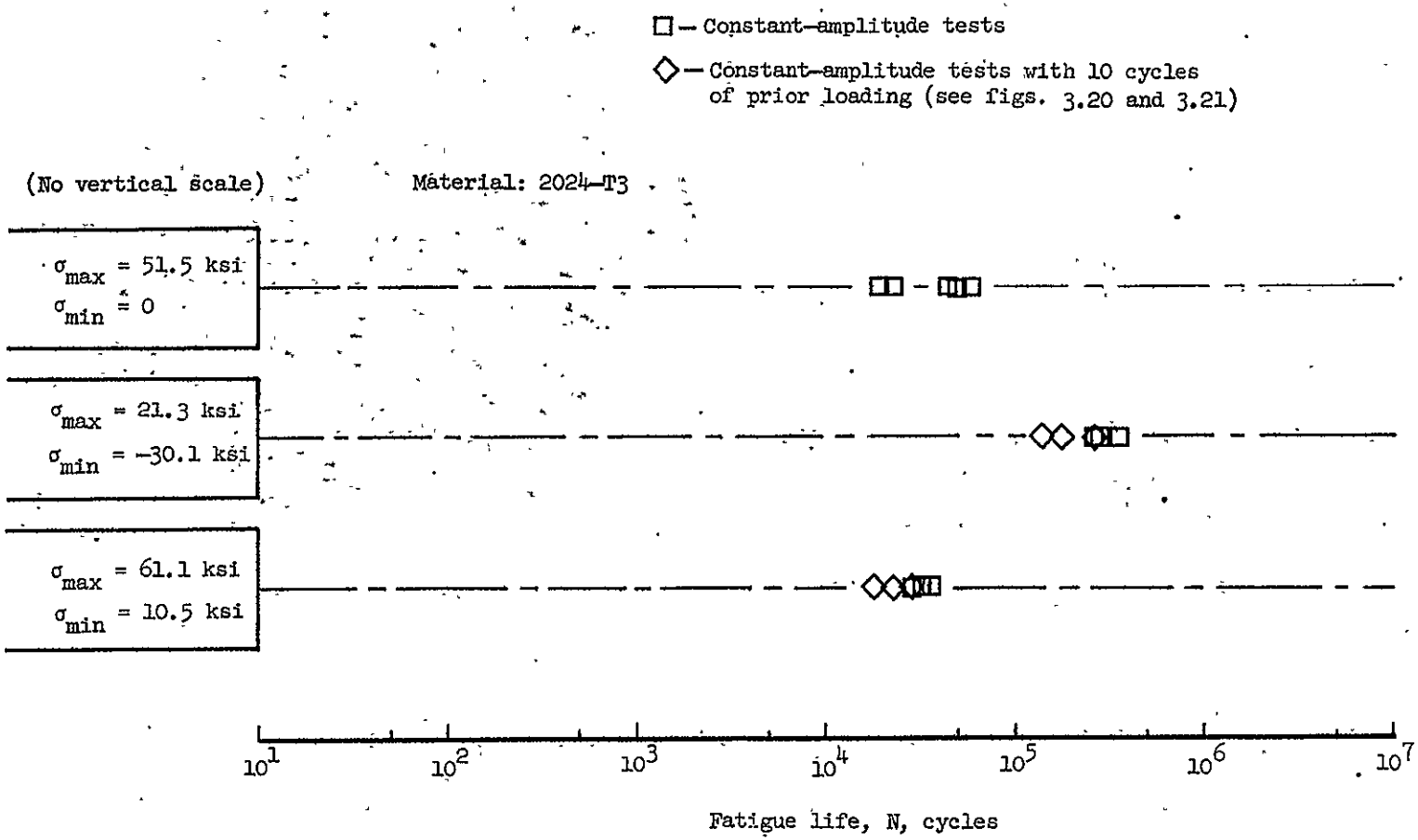

Figure 4.6 — Effects of mean stress and prior loading on fatigue of unnotched specimens.

results in figures 3.20 and 3.21. The analytical-control estimates for N_o from table IV were also presented in figure 4.6 for comparison. These analytical-control results reflect the effects of both types of stress interaction. Consequently, the difference between these results and the constant-amplitude results is a measure of the damage acceleration effect for each test condition. For comparison the analytical-control results corresponding to constant-amplitude S = 20 ksi are also presented in figure 4.6.

The residual stress effect increased the geometric mean of the estimate for N_o from 35,100 to 302,000 cycles in the case of beneficial prior loading. However, damage acceleration caused by the 10 cycles of high load reduced this estimate to 191,000 cycles as shown in figure 4.6. The net effect was an increase in life due to the decrease in local mean stress caused by the 10 cycles of prior loading. These effects agree generally with results obtained by Topper and Sandor [46] in a parametric study of the effects of mean stress and prestrain on fatigue damage accumulation in 2024-T4 aluminum alloy.

For the case of detrimental prior loading, corresponding constant-amplitude tests produced a mean life of 31,600 cycles and simulation tests resulted in a mean life of 22,400 cycles. The residual stress effect decreased the life estimated from 35,100 to 31,600 cycles, and damage acceleration further decreased the simulation results to a mean life of 22,400 cycles. These effects are also in general agreement with results obtained by Topper and Sandor [46] and, in addition, further illustrate the relative magnitudes of the two stress interactions.

In summary, the role of stress concentrations in stress-interaction effects has been demonstrated in this chapter by crack-initiation tests with notched specimens. The stress interactions considered in this study were shown to be the combined result of residual stress effects and damage acceleration caused by large excursions of local stress and strain. The procedure described for predicting crack-initiation lives accounted for both of these effects and produced estimates that reflected the general stress-interaction effects. However, these predictions were consistently shorter than experimentally determined crack-initiation lives for notched specimens. This trend was attributed to the large difference in volumes of highly stressed material for the notched specimens and the unnotched specimens used to obtain the predictions. Additional research is required to assess this size effect and to develop rational procedures for accurately predicting crack initiation at stress-concentration sites.

5. CRACK PROPAGATION NEAR STRESS CONCENTRATIONS

5.1 General

The role of a typical stress concentration in the fatigue crack-initiation process was introduced and discussed in Chapter 4. Local stresses at a stress-concentration site were calculated and used together with unnotched specimens to predict fatigue crack-initiation periods. To complete the fatigue analysis for this typical stress concentration, the behavior of these fatigue cracks was investigated as the cyclic loading was continued beyond that required for crack initiation. The initial stage of growth for a crack emanating from a stress-concentration site is influenced by the stress distribution caused by the stress concentration. However, for repeated loading the crack eventually attains a length for which the influence of the stresses due to the original stress concentration may be ignored, and the crack then may be assumed to propagate solely under the influence of the applied nominal stress. This phase of crack growth has received much attention in the literature (for example [47], [48], and [49]) and was not specifically investigated in this study. Emphasis was placed on crack growth under the influence of the stress concentration. This initial phase of crack growth from a stress-concentration site has received very limited coverage in the literature, as indicated in Chapter 2.

The present study was undertaken to provide an experimental and theoretical investigation of the initial stage of crack growth from a typical stress concentration. For this purpose, the notched specimen

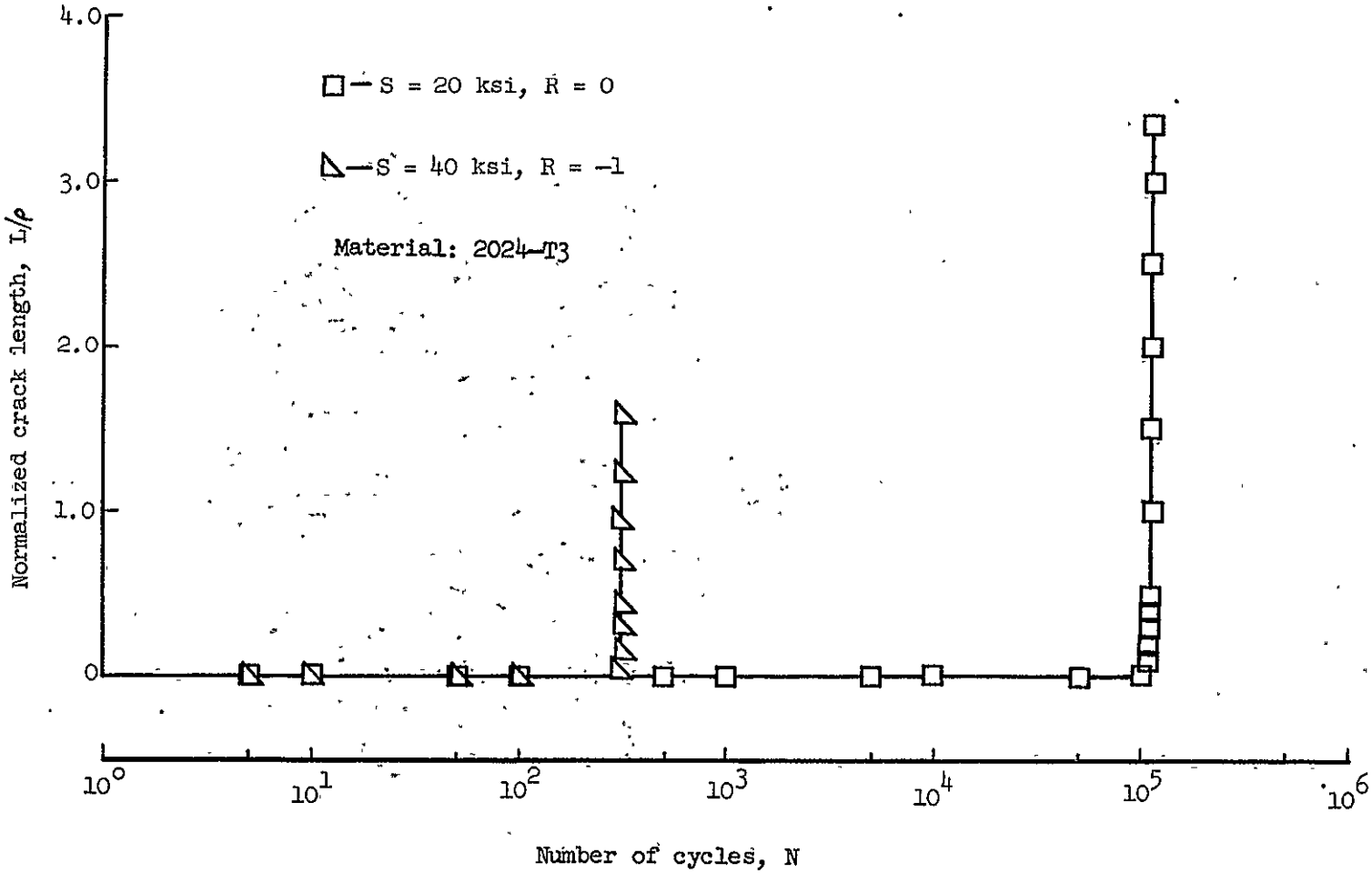

Figure 5.2 – Crack growth curves for constant-amplitude loading.

and the fatigue loading discussed in Chapter 3 (figs. 3.3, 3.11, and 3.12) were used for convenience and, as a result, the study of crack growth was a logical extension of the fatigue analysis presented in Chapter 4. The case of constant-amplitude loading for S = 20 ksi was studied to demonstrate the effect of stress concentrations on crack propagation for completely elastic local conditions and, in addition, this case served as a reference for this evaluation of the stress interaction effects on initial crack growth under two-level loading.

The theoretical phase of this study resulted in the development of a method for calculating initial crack growth for an arbitrary elastic stress distribution near the stress concentration. This method was applied for the reference case of constant amplitude, S = 20 ksi loading, and the calculated results were compared with observed crack-growth behavior. As a more critical evaluation of the method, calculated and experimental results were compared for beneficial two-level loading. These calculated and observed crack-growth results are presented and discussed in the following sections.

5.2 Observed Crack Propagation Behavior Near a Circular Hole

A specimen with a central hole containing cracks is presented in figure 5.1 to illustrate typical crack location and to indicate the two schemes for defining crack length. Crack propagation tests were conducted by continuing the crack initiation tests from Chapter 4 beyond the initiation phase. Crack lengths were measured during these tests with a machinist scale and a low magnification (10X) microscope. In most tests, cracks did not simultaneously initiate on both sides of

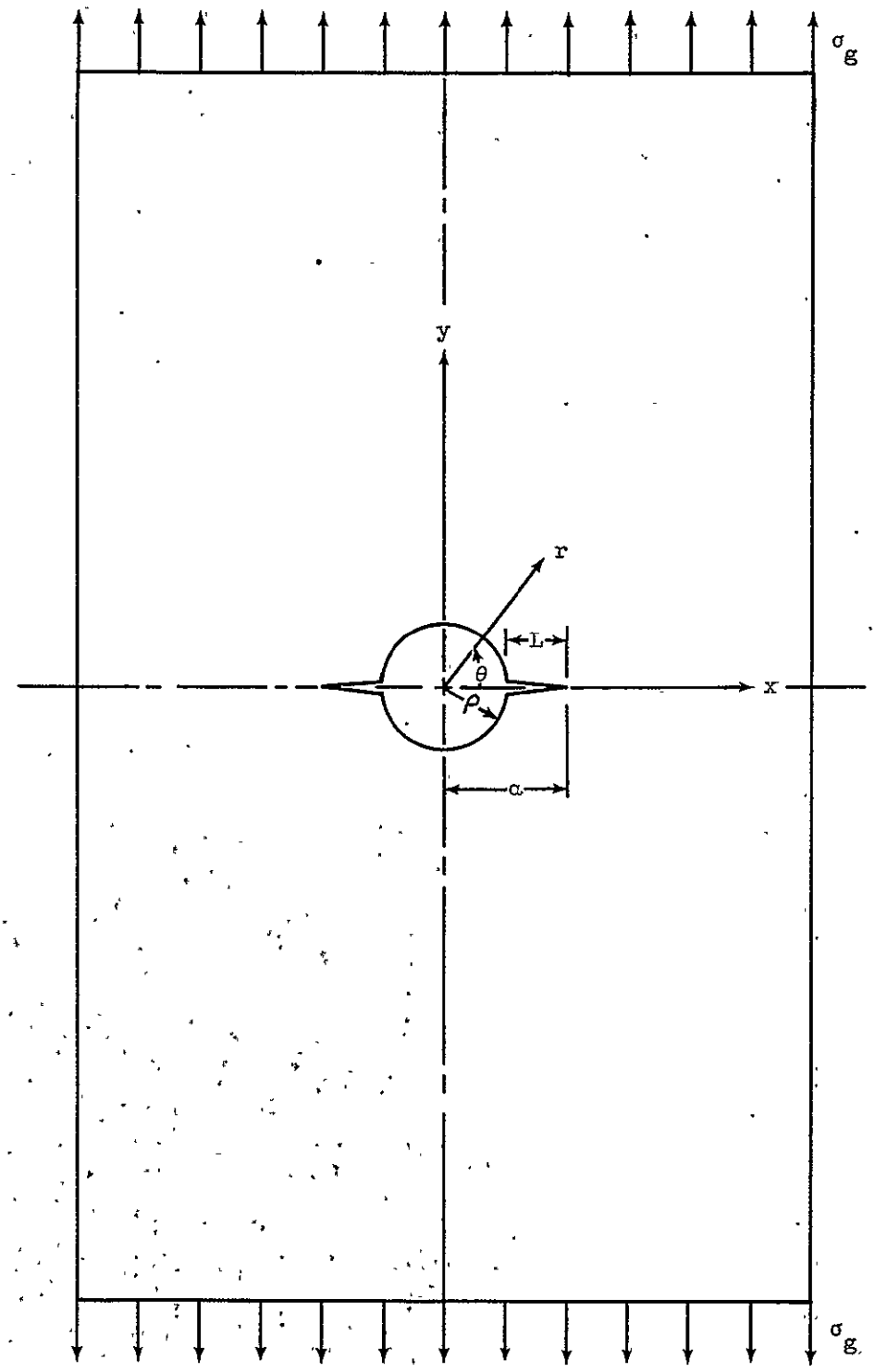

Figure 5.1 – Specimen configuration for crack propagation study.

the hole as shown in figure 5.1. To produce the desired symmetry, after one crack initiated a second crack was simulated on the other side of the hole by a small saw cut with a sharp nick at its root. A jeweler's saw and a sharp razor blade were used to produce this artificial crack. In all cases a fatigue crack promptly initiated at the root of the saw cut and symmetrical crack growth followed.

The crack-growth curves, including the initiation periods, are presented in figure 5.2 for the two constant-amplitude test conditions. For simplicity, a typical curve was plotted for each test condition. Local cyclic plasticity accompanied the initial crack growth for $S = 40$ ksi loading, precluding an analysis of this case. In contrast, local behavior at the hole was completely elastic during the cycling at $S = 20$ ksi, and enabled use of Fracture Mechanics theory. The crack-growth curve for $S = 20$ ksi was used as a reference for establishing the effects of two-level loading on initial crack propagation. For this purpose this curve will be subsequently replotted with an expanded cycles scale.

Prior loading was demonstrated in Chapter 4 to be either detrimental or beneficial to crack initiation, depending on the sense of the residual stress at the end of the prior loading. This behavior is again displayed by the typical crack-growth curves in figure 5.3 for two-level loading. To separate these curves into crack-initiation and propagation stages, the initiation period was assumed to equal the number of cycles required to produce a crack length of 0.03 inch (the smallest crack length for which crack propagation data were

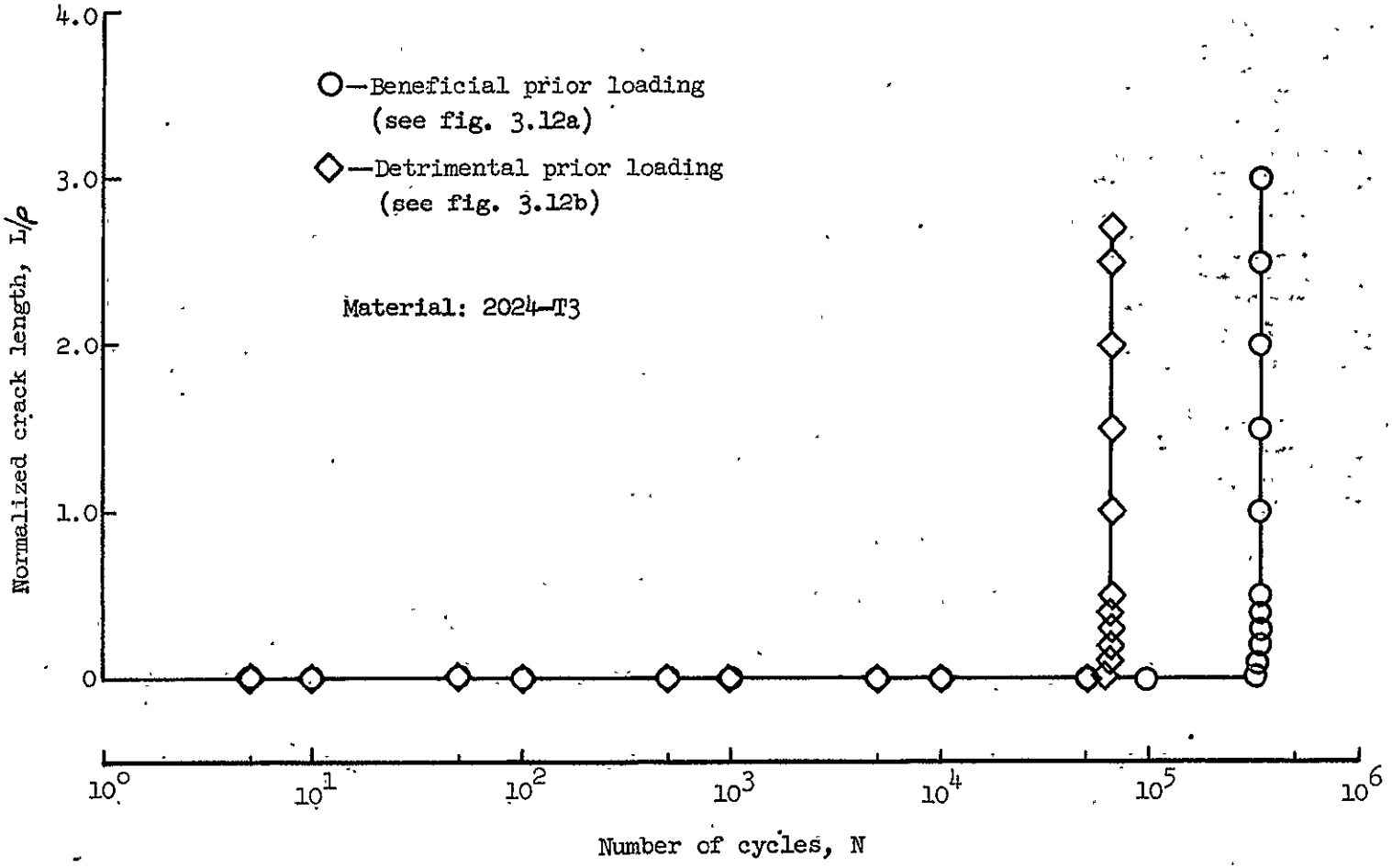

Figure 5.3 – Crack growth curves for beneficial and detrimental prior loading.

obtained for all three loading conditions). The crack lengths beyond this initial value were plotted in figure 5.4 against the number of cycles for crack propagation N_{cp}. Starting at the same initial length, the beneficial prior loading decreased the initial crack-growth rates as compared to the reference case of constant-amplitude loading. The detrimental prior loading caused the crack-growth rates to increase. Beyond a crack length of approximately 0.7 inch, crack growth was nearly identical for all three cases, indicating the localized nature of the influence of the stress concentration. A procedure is presented in the next section for evaluating this influence.

5.3 Procedure For Calculating Crack Propagation Behavior Near a Circular Hole

Paris, Gomez, and Anderson [49] postulated the existence of a unique relationship between stress-intensity factor and rate of crack propagation. Thus crack growth could be predicted from calculated stress-intensity factors and "master" crack propagation rate curves, characterizing the crack-growth properties of the material. Stress-intensity factors can be calculated from elastic analyses of bodies containing cracks. The "master" crack-growth rate curve can be established by measuring crack-growth rates corresponding to known stress-intensity values using simple laboratory specimens. This general approach was followed by Figge and Newman [50] to predict crack growth for complex specimen configurations and loadings. A generally close correlation was found between predicted and experimental results.

In the present study, this general stress-intensity approach was used to predict crack-growth curves corresponding to the

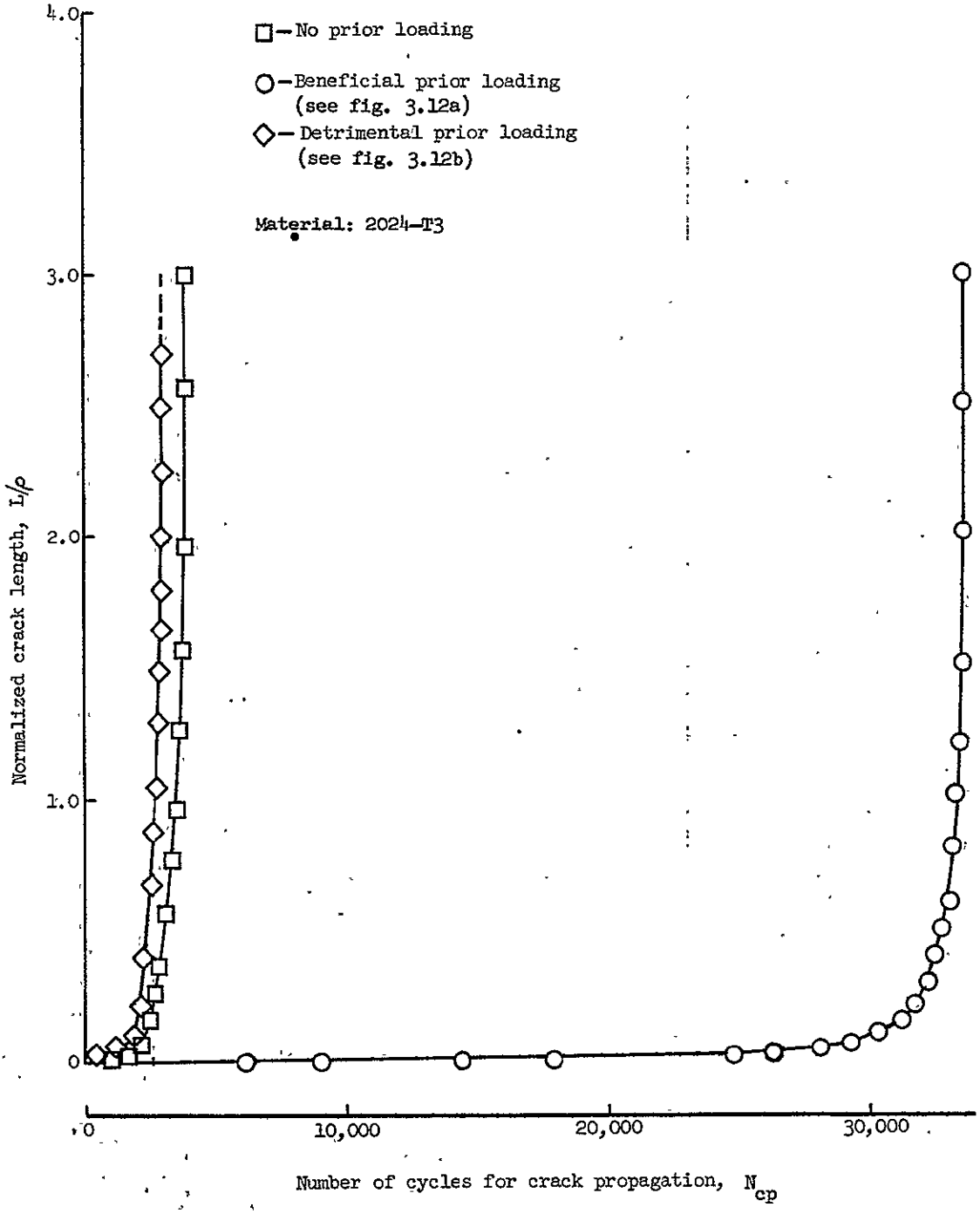

Figure 5.4 — Comparison of crack growth curves for S = 20 ksi loading with and without prior loading.

constant-amplitude loading for $S = 20$ ksi and the case of beneficial prior loading.

5.3.1 Calculation of Stress-Intensity Factor For Crack Emanating From a Circular Hole

Bowie [51] developed polynomial mapping functions for use with the complex stress function technique to solve the problem of cracks emanating from a circular hole in an infinite sheet. For the case of two cracks emanating from a circular hole (see fig. 5.1) Paris and Sih [52] presented Bowie's solution in the form

$$k = \sigma_g \sqrt{L}\, F\left(\frac{L}{\rho}\right) \tag{19}$$

where σ_g is the gross nominal stress and L is crack length. This stress intensity is plotted in figure 5.5. The stress-intensity solution

$$k = \sigma_g \sqrt{a} = \sigma_g \sqrt{L + \rho} \tag{20}$$

for a crack of length $2a$, without the circular hole, is also plotted in figure 5.5 for comparison. Beyond $L/\rho = 0.25$, the curves for equations (19) and (20) are in rather close agreement. Consequently for $L/\rho \geq 0.25$ the presence of the hole may be ignored and the crack-growth behavior approximated by that of a simple crack with $a = \rho + L$, again illustrating the localized effect of stress concentrations.

Bowie's solution could have been used to predict the crack growth for the reference case of $S = 20$ ksi constant-amplitude loading, because the local conditions at the hole were elastic. However, for

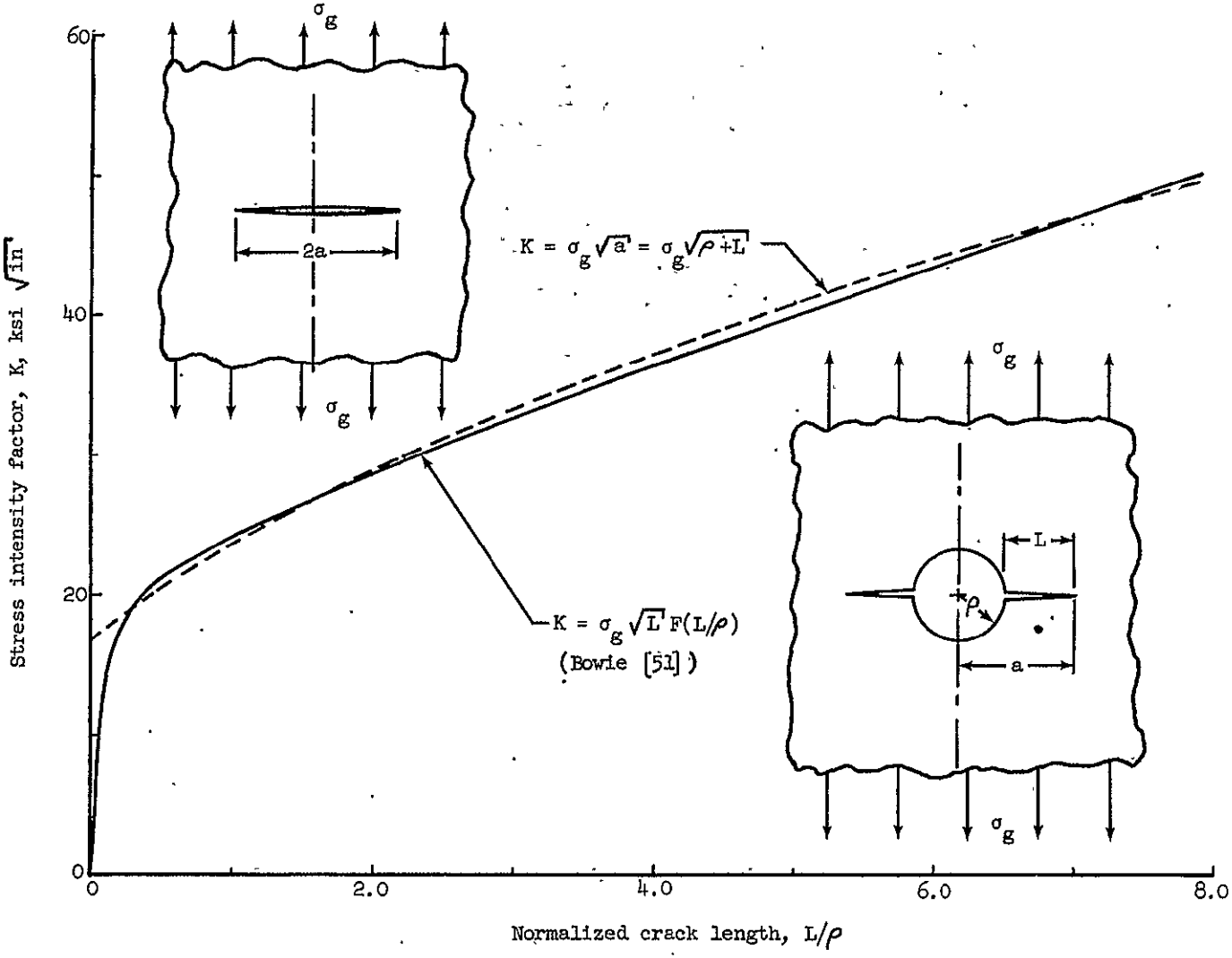

Figure 5.5 – Stress intensity factors for cracks emanating from a circular hole.

the two-level loading sequence, residual stresses altered the stress distribution around the circular hole, and consequently changed the stress-intensity factors for the cracks growing from the hole, as evidenced by the crack-growth curves in figure 5.4. To account for the effects of residual stresses on crack growth from circular holes, a general stress-intensity solution was developed for an arbitrary stress distribution $\sigma(x)$ along the plane of the crack. This stress-intensity analysis is presented in the following development and is specialized in the next section for the elastic reference case and for the case of beneficial prior loading.

The analysis of stress intensity for the cracked specimen and loading in figure 5.6(a) was based on the separation of this problem into those given in figure 5.6(b) and fig. 5.6(c). The stress distribution in figure 5.6(b) along the plane of the crack was designated $\sigma(x)$. The superposition of this internal stress $\sigma(x)$ from figure 5.6(b) and the $-\sigma(x)$ shown in figure 5.6(c), acting on the crack boundary, resulted in the stress-free crack surface shown in figure 5.6(a). Because the specimen in figure 5.6(b) did not contain a crack, the stress-intensity factor for figure 5.6(a) was equal to that for figure 5.6(c). The stress-intensity factor for figure 5.6(c) was found by an additional superposition scheme used together with a boundary collocation technique. Irwin [53] presented the Westergaard stress function

$$Z_1(z) = \frac{2Pz}{\pi t(z^2 - b^2)}\left[\frac{a^2 - b^2}{z^2 - a^2}\right]^{1/2} \qquad (21)$$

for the problem shown in figure 5.7 for symmetrical concentrated loads on a crack surface. This solution was used to represent the $\sigma(x)$ from figure 5.6(c) by a statically equivalent system of forces shown typically in figure 5.8. The radial stresses σ_{rr} and shear stress $\tau_{r\theta}$ along the circle of unit radius were found for each concentrated force from the following equations, developed in Appendix A.

$$\left.\begin{aligned} \sigma_{rr} &= \left[\mathrm{Re}Z_1 - yI_mZ_1'\right]\cos^2\theta + \left[\mathrm{Re}Z_1 + yI_mZ_1'\right]\sin^2\theta \\ &\quad - 2y\mathrm{Re}Z_1' \sin\theta\cos\theta \\ \text{and} \\ \tau_{r\theta} &= y\left[2I_mZ_1' \sin\theta\cos\theta - \mathrm{Re}Z_1'(\cos^2\theta - \sin^2\theta)\right] \end{aligned}\right\} \quad (22)$$

The σ_{rr} and $\tau_{r\theta}$ stress components for all concentrated forces were summed to obtain the stress distributions along the unit circle, corresponding to the $\sigma(x)$ in figure 5.6(c). Following a boundary collocation procedure presented by Newman [54] a second set of σ_{rr} and $\tau_{r\theta}$ was expressed as (see Appendix B)

$$\begin{aligned} \sigma_{rr} = \sum_{n=1}^{M} \Bigg\{ & 2A_n\left[\frac{1}{r^{2n-1}\sqrt{r_1r_2}}\cos\left[(2n-1)\theta + \beta_1\right]\right. \\ & \left. - \frac{(2n-1)y}{r^{2n}\sqrt{r_1r_2}}\sin\left[(2n-2)\theta + \beta_1\right] - \frac{y}{r^{2n-2}\sqrt{(r_1r_2)^3}}\sin\left[(2n-4)\theta + \beta_2\right]\right] \\ & + 2B_n\left[\frac{1}{r^{2n}}\cos 2n\theta - \frac{2ny}{r^{2n+1}}\sin(2n-1)\theta + \frac{1}{r^{2n}}\cos(2n-2)\theta\right]\Bigg\} \end{aligned} \quad (23)$$

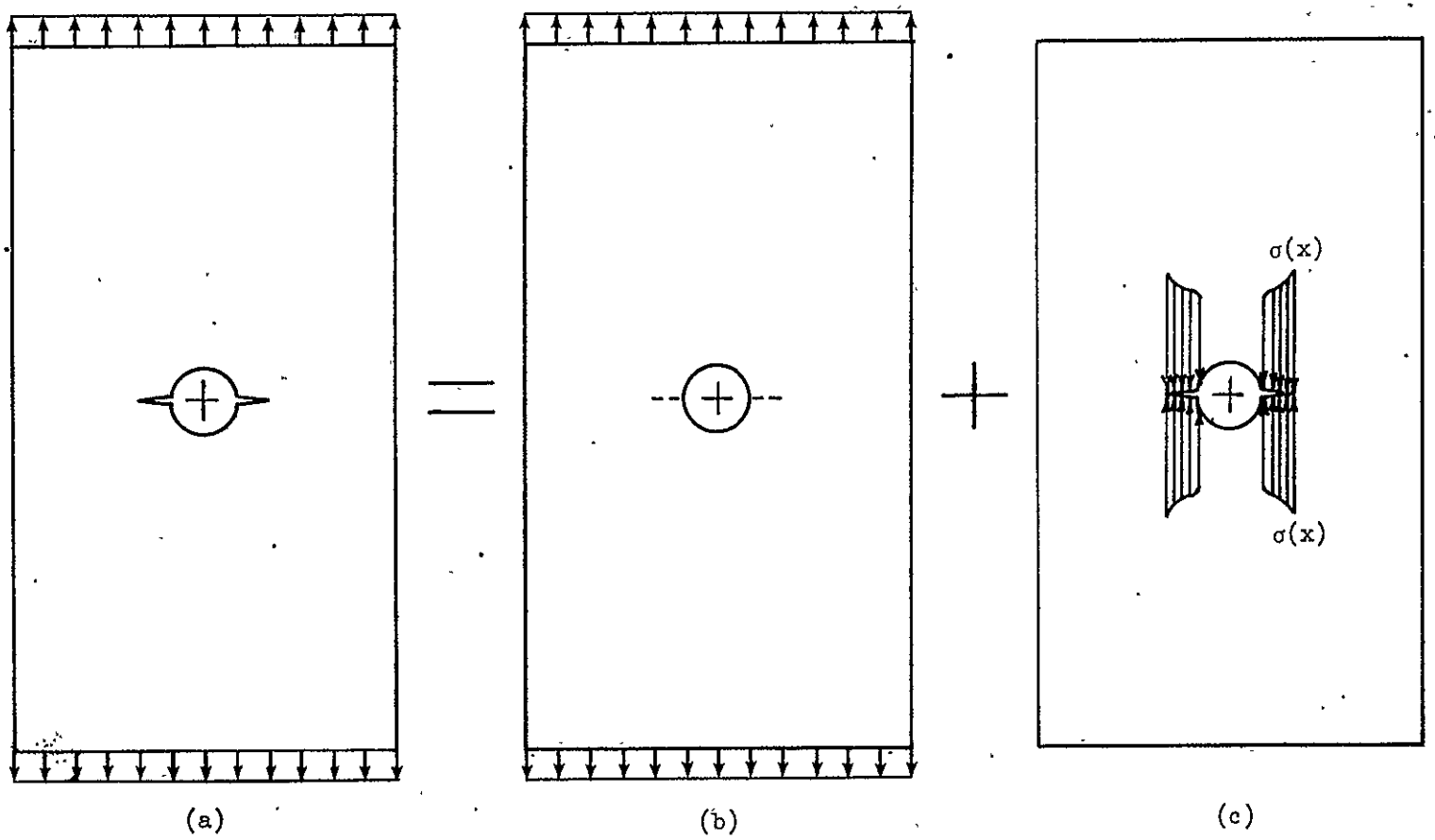

Figure 5.6 – Superposition of loading systems.

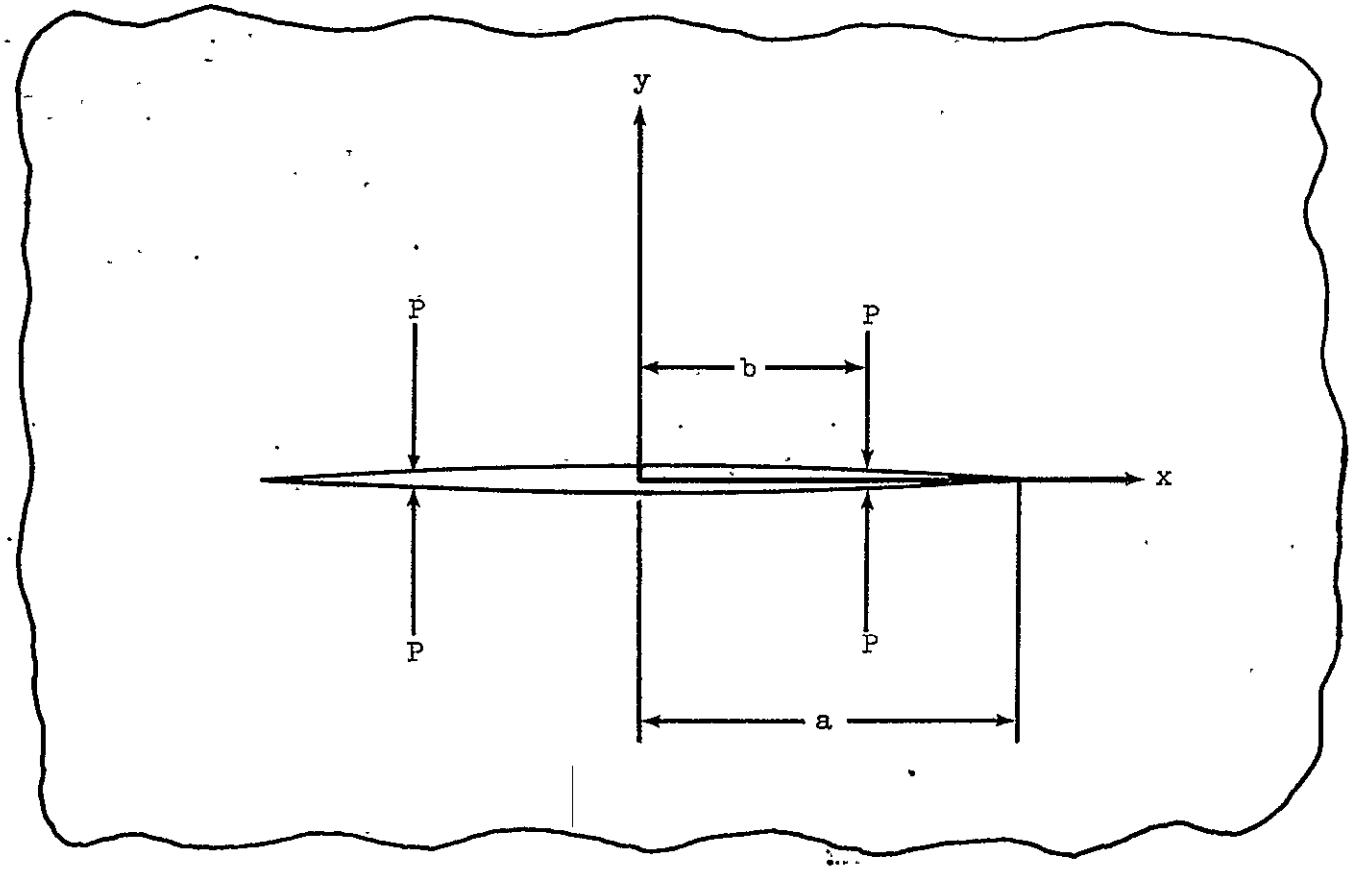

Figure 5.7 – Concentrated forces on crack surface.

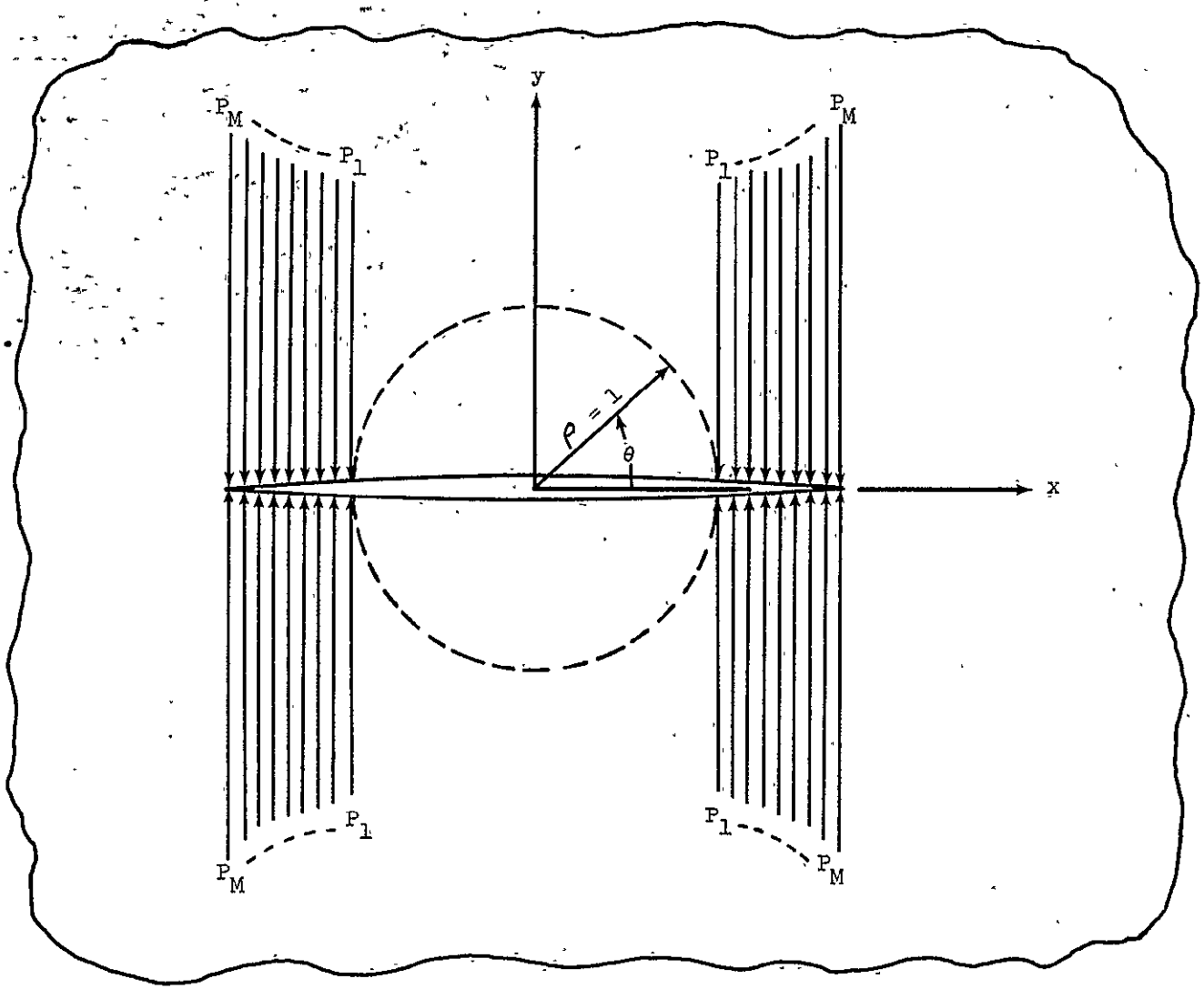

Figure 5.8 – Simulation of $\sigma(x)$ on crack surface using concentrated forces.

and

$$\tau_{r\theta} = \sum_{n=1}^{M} \left\{ 2A_n \left[\frac{(2n-1)y}{r^{2n}\sqrt{r_1 r_2}} \cos\left[(2n-2)\theta + \beta_1\right] \right.\right.$$

$$\left. + \frac{y}{r^{2n-2}\sqrt{(r_1 r_2)^3}} \cos\left[(2n-4)\theta + \beta_2\right] \right] + 2B_n \left[\frac{2ny}{r^{2n+1}} \cos(2n-1)\theta \right.$$

$$\left.\left. + \frac{1}{r^{2n}} \sin(2n-2)\theta \right] \right\} \qquad (24)$$

The σ_{rr} and $\tau_{r\theta}$ from equations (23) and (24) were equated to corresponding sum of the stresses from equation (22) at discrete points on the circular arc and coefficients A_n and B_n were determined from the resulting set of equations. Thus by superposition, the two sets of radial and tangential stresses cancelled each other at intervals along the circular arc of unit radius to effectively create a stress-free boundary. This superposition is illustrated in figure 5.9. The σ_{rr} and $\tau_{r\theta}$ on the unit circle in figure 5.9(b), due to the concentrated loads, opposed the σ_{rr} and $\tau_{r\theta}$ in figure 5.9(c) from equations (23) and (24), and, as a result, the stress-free hole with cracks in figure 5.9(a) was simulated.

The stress-intensity factor for the case presented in figure 5.6(c) and again in figure 5.9(a) was found by superposition of the stress-intensity factors for figures 5.9(b) and 5.9(c). The stress-intensity factor for each concentrated force was given by Paris [57] as

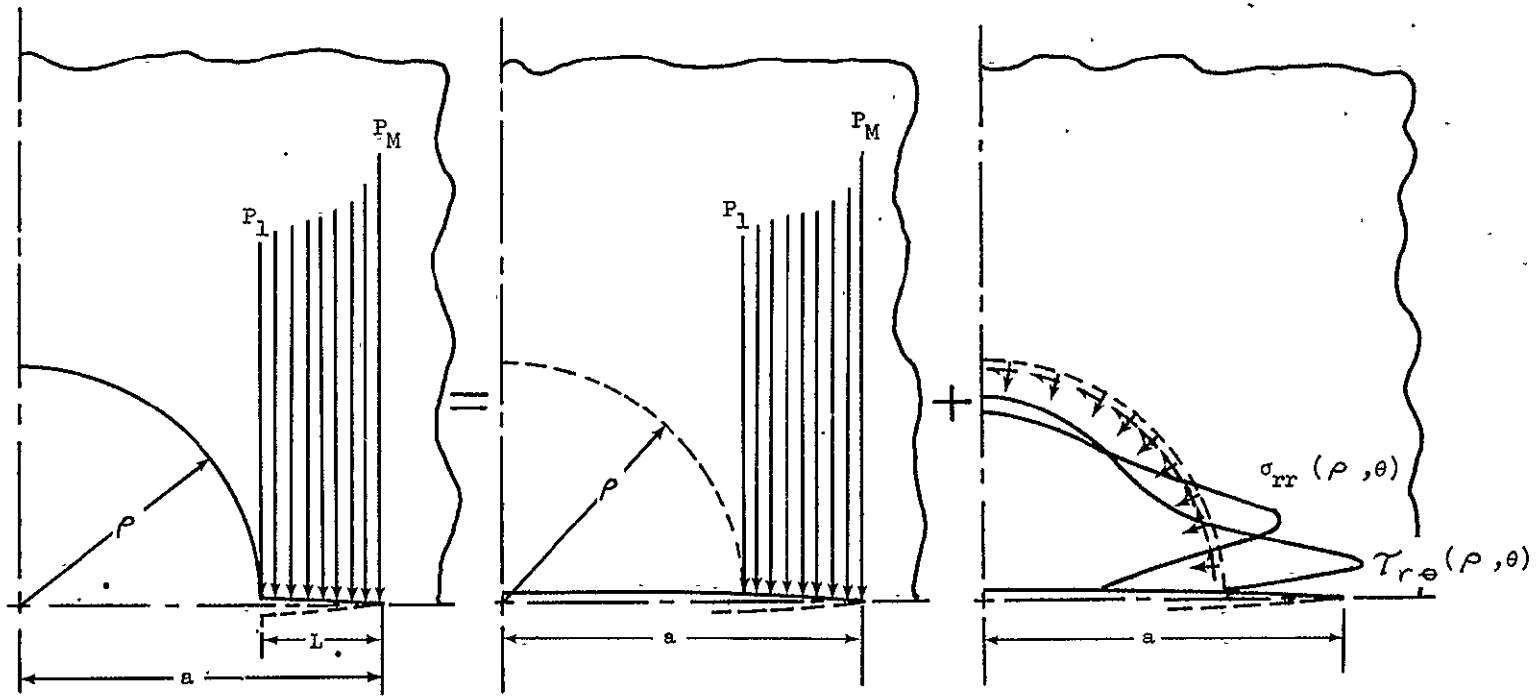

(a) Simulation of $\sigma(x)$ using concentrated forces

(b) Central-crack with array of concentrated forces from (a)

(c) Central crack with $\sigma_{rr}(\rho,\theta)$ and $\tau_{r\theta}(\rho,\theta)$ equal and opposite to those in (b)

Figure 5.9 – Superposition of $\sigma_{rr}(\rho,\theta)$ and $\tau_{r\theta}(\rho,\theta)$ to create stress-free boundary at $r = \rho$.

$$k = \frac{2P\sqrt{a}}{\pi t\sqrt{a^2 - b^2}} \tag{25}$$

therefore the stress-intensity factor for figure 5.9(b) was

$$k = \sum_{i=1}^{M} \frac{2P_i\sqrt{a}}{\pi t\sqrt{a^2 - b_i^2}} \tag{26}$$

where M was the number of concentrated loads. The stress-intensity factor for the loading shown in figure 5.9(c) was written in terms of $\Phi(z)$ by Paris and Sih [52] as

$$k = 2\sqrt{2} \lim_{z \to a} \sqrt{z - a}\,\Phi(z) \tag{27}$$

Therefore from equations (26) and (27) we obtain,

$$k = \sum_{i=1}^{M} \frac{2P_i\sqrt{a}}{\pi t\sqrt{a^2 - b_i^2}} + 2\sqrt{2} \lim_{z \to a} \sqrt{z - a}\,\Phi(z) \tag{28}$$

which represents the stress-intensity factor for the case shown in figures 5.9(a) and 5.6(c) and consequently for the original case, illustrated in figures 5.6(a) and 5.1.

Equation (28) was evaluated with the aid of a digital computer for discrete crack lengths and for the corresponding values of $\sigma(x)$. The stress-intensity factor was plotted for each crack length and a curve was drawn through these points to obtain a curve similar to that presented in figure 5.5 but for a general stress distribution, $\sigma(x)$, along the crack plane. For an evaluation of this general approach

$\sigma(x)$ was specialized for the elastic distribution and the stress-intensity results were compared with the curve from figure 5.5. The close correlation in figure 5.10 between these results from equation (28) and Bowie's solution demonstrated the adequacy of the superposition and boundary collocation techniques applied in the development of equation (28).

These results, also presented in table VI, show that beyond a crack length of 0.7 inch less than 6 percent difference exists between the stress-intensity factors for the two cases. Consistent with these results, for all loading conditions nearly identical crack-growth behavior was observed for cracks larger than 0.7 inch, as shown previously in figure 5.4.

5.3.2 Calculation of Crack-Growth Curves From Stress-Intensity Solutions

The correspondence between stress-intensity factor and crack-growth rate demonstrated by Figge and Newman [50] was utilized to calculate crack propagation curves. The basic crack-growth behavior of 2024-T3 aluminum alloy was experimentally established through laboratory tests of centrally cracked sheet specimens for which crack-growth rates were measured and the corresponding stress-intensity factors calculated from equation (20) using the Irwin-Westergaard finite width correction from [52]. Experimental results are presented in figure 5.11 to characterize the crack-growth behavior for this material. This curve in figure 5.11 together with the stress-intensity solution for a given $\sigma(x)$ were used to calculate crack length against cycles curves as follows. Stress-intensity factors were found for crack lengths a

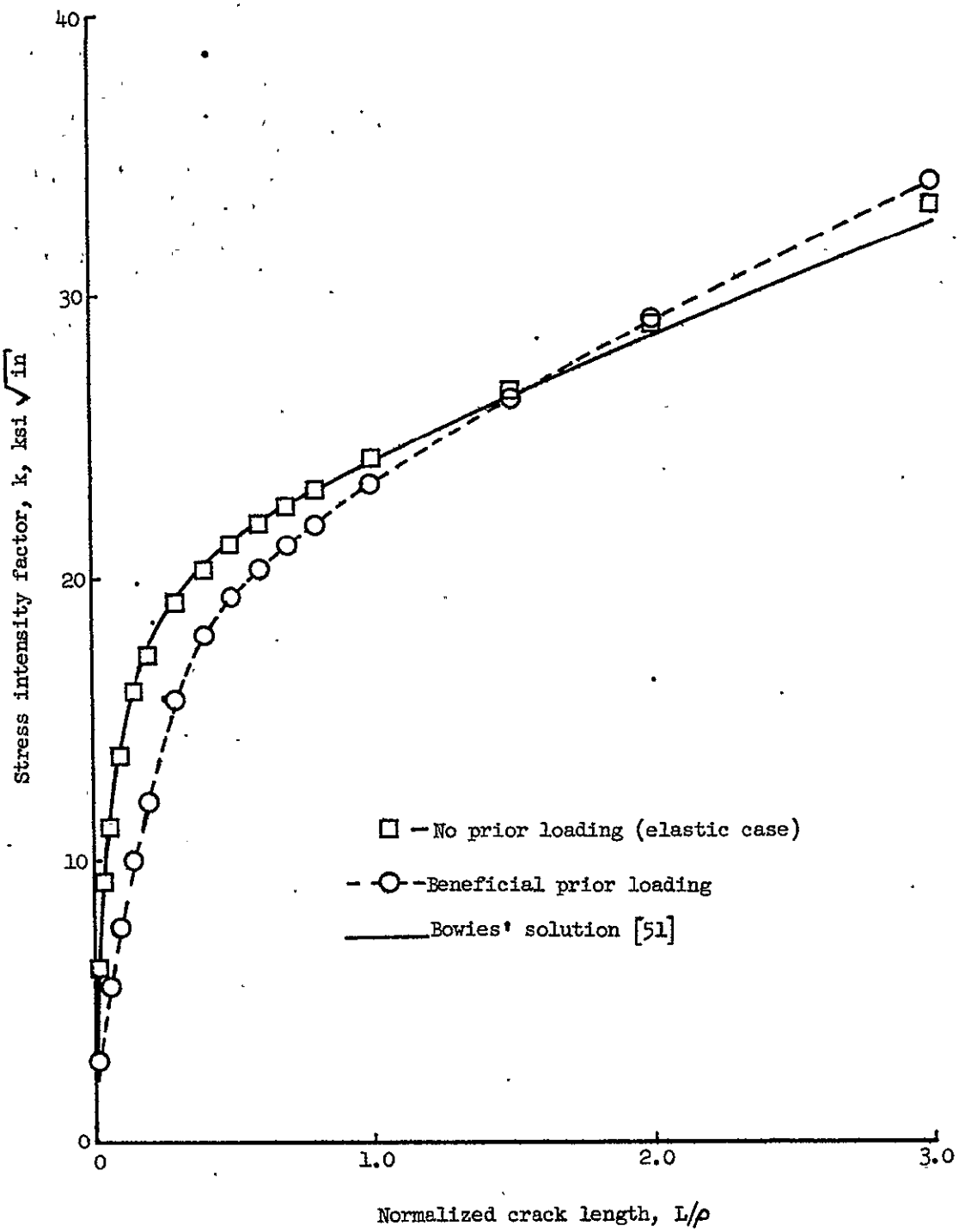

Figure 5.10 – Comparison of calculated stress intensity factors with Bowie's solution [51].

TABLE VI.- CALCULATED STRESS-INTENSITY FACTORS

Crack length L/ρ	Stress intensity factors, k, ksi $\sqrt{in.}$	
	Constant-amplitude S = 20 ksi	Beneficial prior loading
0	0	0
0.01	5.970	2.523
0.02	6.683	2.917
0.03	8.008	3.611
0.04	9.284	4.319
0.06	11.30	5.578
0.08	12.80	6.684
0.10	13.78	7.694
0.15	16.04	10.01
0.20	17.30	12.12
0.30	19.21	15.79
0.40	20.36	18.02
0.50	21.21	19.40
0.60	21.93	20.37
0.70	22.56	21.20
0.80	23.14	21.97
1.00	24.32	23.38
1.50	26.74	26.54
2.00	29.07	29.28
3.00	33.33	34.19
4.00	37.17	38.39
5.00	40.68	42.14

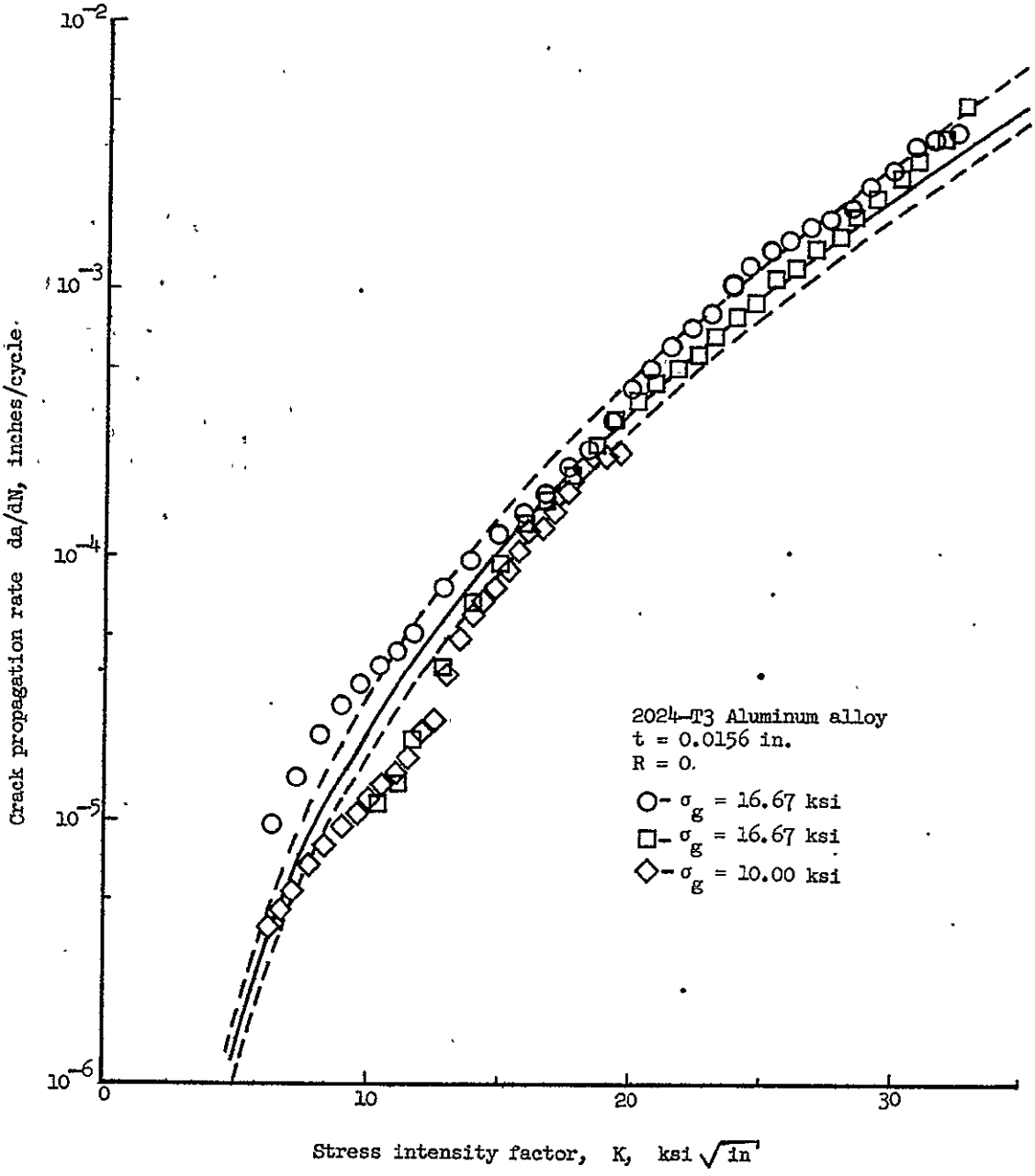

Figure 5.11 – Master crack propagation curve for 2024-T3 aluminum alloy.

and $a + \Delta a$ and corresponding crack-growth rates were found from the master curve in figure 5.11. The number of cycles required to extend the crack by Δa was determined from

$$\Delta N = \frac{2\Delta a}{\left.\frac{da}{dN}\right|_a + \left.\frac{da}{dN}\right|_{a+\Delta a}} \tag{29}$$

The total number of cycles required to grow the crack to a given length was found by dividing the crack into intervals Δa, and by summing the ΔN from equation (29) associated with each Δa. For the present study, a digital computer was used in this procedure to calculate curves for crack length against cycles. These results are presented in the next section and are compared with observed results of Section 5.2.

5.4 Comparison of Calculated and Observed Crack Propagation Behavior

Comparisons are made in this section between calculated and observed crack-growth results for the reference case of constant-amplitude, S = 20 ksi, loading and for the case of two-level beneficial prior loading. The stress distributions, $\sigma(x)$, on the transverse axis were found, respectively, by elastic and elastoplastic analyses for these two cases, and the methods from Section 5.3.1 were used to develop stress-intensity factor solutions. These stress-intensity results were then utilized together with the master crack propagation curve in figure 5.11 to calculate crack length against cycles curves similar to the experimental curves in figure 5.4.

5.4.1 Constant-Amplitude (S = 20 ksi) Loading

A system of concentrated forces was developed to simulate the elastic stress distribution on the transverse axis by the procedure presented in Appendix C. This force system was used to develop the stress-intensity curve previously presented in figure 5.10 for an evaluation of the accuracy of the stress-intensity analysis. This stress-intensity solution led to the crack length against cycles curve presented in figure 5.12. Because of the inherent scatter in crack propagation data in figure 5.11 upper and lower limits were used to characterize this crack propagation behavior as shown. These limits were used to calculate the corresponding range of crack-growth behavior for the case of constant-amplitude, S = 20 ksi loading. This expected range of behavior is indicated by the shaded zone in figure 5.12. The solid curve within this shaded zone represents average behavior found from the corresponding average curve in figure 5.11.

The symbols in figure 5.12 represent test data. For the two tests conducted with no prior loading (constant-amplitude) one set of test results fall slightly outside of the range of calculated behavior. The second set of results is within this range and the average of these two sets of data was within the shaded zone. Because of large errors in crack length against cycles behavior that may result from rather small errors in stress-intensity factors (and therefore crack propagation rates) for short crack lengths, the correlation between experimental and calculated results in figure 5.12 is exceptionally close.

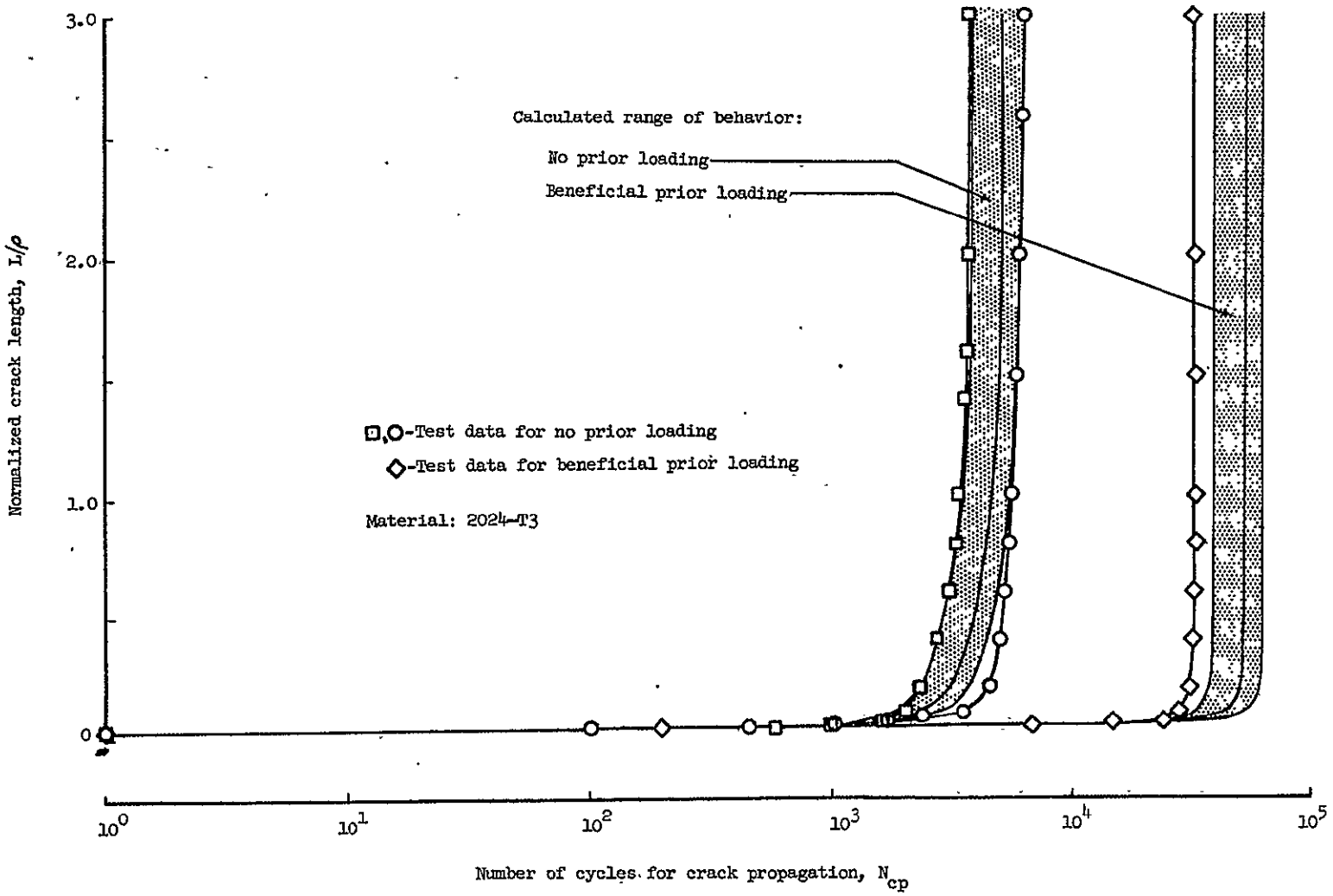

Figure 5.12 – Comparison of calculated and observed crack growth curves.

5.4.2 Beneficial Two-Level Loading

An approximate analysis is presented in Appendix C for the stress distribution corresponding to beneficial two-level loading. This stress distribution was discretized and also simulated by a system of concentrated forces. This force system together with the procedures outlined in Section 5.3.1 resulted in the stress-intensity solution listed in table VI and plotted in figure 5.10. The low stresses calculated in Appendix C for small values of x produced stress-intensity factors that were lower than those for the constant-amplitude case.

As expected, these low values of stress intensity created a large crack propagation life, as shown in figure 5.12. Again the results are presented as a range of calculated behavior. For this case, however, the single experimental crack length against cycles curve did not lie within the calculated range. This discrepancy may have been the result of scatter in material behavior (note that data points fall outside of the limits used in figure 5.11 to characterize the assumed scatter). Additional tests are required for a critical assessment of this analytical approach, however, the single experimental curve in figure 5.12 illustrates reasonable agreement between calculated and observed results. As previously mentioned, small variations in stress-intensity values for short cracks produce significant changes in predicted crack propagation lives. For this reason, minor refinements in the elastoplastic analysis of the stress distribution or in the simulation of this stress distribution by concentrated forces could noticeably improve the correlation between experimental and calculated results in figure 5.12.

3

6. CONCLUDING REMARKS

An analysis of the role of a typical stress concentration in structural fatigue has been presented. The analysis considers the cyclic stress-strain behavior at stress-concentration sites, the initiation of fatigue cracks, and the initial stage of propagation for cracks growing from the stress-concentration site. The stress concentration dealt with in this study was that produced by a circular hole in a sheet specimen under remote load. The behavior of this specimen was investigated for constant-amplitude loading and two-level loading, that created stress interactions typical of those experienced by structures in service.

For the analysis of stress-strain conditions at the stress-concentration site, attention was focused on the point of maximum stress concentration, and conditions at this point were referred to as "local" conditions. Cyclic local stress and strain were simulated in simple unnotched specimens by loading these specimens between calculated limits for local behavior. This simulation was performed on a cycle-by-cycle basis and, as a result, residual stress effects and cyclic variations in material behavior, that generally complicate local conditions, were automatically accounted for in quantitative estimates of local stress and strain. For an evaluation of the simulation procedure, local cyclic stress-strain behavior was experimentally determined by a companion-specimen method and the two sets of results were compared.

The simulation procedure was continued until the unnotched specimens failed by fatigue. Because the stress-strain conditions in these unnotched specimens were assumed to be identical to the conditions at the stress-concentration site, these fatigue lives were used as estimates for fatigue crack-initiation lives for notched specimens. Notched specimens were tested in fatigue to obtain observed crack-initiation lives which were used for quantitative assessment of stress-interaction effects predicted by the simulation procedure.

The effects of prior high loading on cracks growing from stress concentrations were demonstrated by tests with notched specimens. Crack length against cycles curves were experimentally determined from these tests and were compared with similar predicted curves. Predicted curves were calculated by expressing the state of stress near the crack tip in terms of stress-intensity factors and by using these stress-intensity factors together with an experimental curve generally characterizing the crack propagation behavior of the specimen material.

Based on analytical and experimental results presented in this study, the following conclusions are presented.

1. Prior high loading on a notched specimen may dramatically alter the local mean stress corresponding to subsequent loading. Prior loading may be selected to either increase or decrease this local mean stress.

2. The companion-specimen method together with the strain-coupled servo-control system presented in this study provide means for experimentally investigating local cyclic stress and strain.

3. The simulation procedure for approximating local cyclic stress-strain behavior adequately accounts for local plasticity. Furthermore, changes in stress-strain properties due to cycling are inherently incorporated in the calculations of local behavior.

4. The increase in crack-initiation lives for tensile prior loading on notched specimens is the result of the net effect of beneficial compressive residual stresses and the detrimental effect of damage acceleration caused by large excursions of local strain at the stress-concentration site during prior loading. For compressive prior loading, detrimental tensile residual stresses and damage acceleration combine to decrease crack-initiation lives.

5. The simulation procedure for estimating crack-initiation lives for stress concentrations using unnotched control specimens accounted for the effects of stress interactions and, as a result, yielded reasonable estimates. These estimates were, however, conservative for both constant-amplitude and two-level loading due to a size effect not accounted for in this simulation procedure.

6. The initial stage of crack propagation for cracks emanating from a stress-concentration site may be altered by prior loading during the crack-initiation phase. Prior tensile loading decreases initial crack propagation rates and compressive prior loading increases propagation rates.

7. Reasonable predictions of crack length against cycles were obtained for the initial stage of crack growth when the stress state near the crack tips were defined by stress-intensity factors which were used to establish crack propagation rates.

Although the procedures and conclusions in this study are applicable only for sheet specimens with stress concentrations, it is possible that they will prove useful in fatigue analysis of more complicated configurations and loading.

7. REFERENCES

1. Aeronautical Systems Division, Wright-Patterson Air Force Base, Ohio: "Effect of Compressive Loads on Structural Fatigue at Elevated Temperature." ASD-TDR-62-488, October 1962.

2. Ibrahim, S. M., McCallion, H., and Dudley, B. R.: "Elastic-Plastic Deformation Around a Circular Hole in a Plate Under Cyclic Loading." Proc. Instn. Mech. Engrs., vol. 180, pt. 31, 1965-1966, pp. 438-447.

3. Isakson, G., Armen, H., and Pifko, A.: "Discrete-Element Methods For the Plastic Analysis of Structures." NASA CR-803, October 1967.

4. Crews, J. H., Jr.: Private communication with Grumman Aircraft Engineering Corp. (reported in [3] above), 1965.

5. Jordan, W. B.: "A Program to Solve Elastic Structures By the Use of Finite Elements." Knolls Atomic Power Lab, General Electric Co., KAPL-M-6582 (WBJ-4), December 1966.

6. Mowbray, D. F., and Slot, T.: "A Note on Stress and Strain Redistribution in Notched Specimen During Cyclic Loading." To be published by ASTM, 1968.

7. Blatherwick, A. A., and Olson, B. K.: "Stress Redistribution in Notched Specimens During Fatigue Cycling." Presented at the 1968 Spring Meeting, Albany, N. Y. To be published in Proc. of SESA, 1968.

8. Stowell, E. Z.: "Stress and Strain Concentration at Circular Hole in an Infinite Plate." NACA TN 2073, April 1950.

9. Neuber, H.: "Theory of Stress Concentration For Shear-Strained Prismitical Bodies With Arbitrary Nonlinear Stress Strain Law." Jour. of Applied Mechanics, vol. 28, series E, no. 4, 1961, pp. 544-550.

10. Griffith, G. E.: "Experimental Investigation of the Effects of Plastic Flow in a Tension Panel With a Circular Hole." NACA TN 1705, September 1948.

11. Hardrath, H. F., and Ohman, L.: "A Study of Elastic and Plastic Stress Concentration Factors Due to Notches and Fillets in Flat Plates." NACA TR 1117, 1953.

12. Box, W. A.: "The Effect of Plastic Strains on Stress Concentrators." Proceeding of SESA, vol. 8, no. 2, 1951, pp. 99-110.

13. Crews, J. H., Jr.: "Local Plastic Stresses in Sheet Aluminum Alloy Specimens With Stress-Concentration Factor of 2 Under Constant-Amplitude Loading." NASA TN D-3152, December 1965.

14. Crews, J. H., Jr., and Hardrath, H. F.: "A Study of Cyclic Plastic Stresses at a Notch Root." Proceedings of SESA, vol. 6, no. 6, June 1966, pp. 313-320.

15. Crews, J. H., Jr.: "Elasto-Plastic Stress-Strain Behavior at Notch Roots in Sheet Specimens Under Constant-Amplitude Reversed Loading." NASA TN (in preparation).

16. Neuber, H.: "Stress and Strain Concentration at Nonlinear Elastic and Plastic Deformation." Recent Progress in Applied Mechanics. Edited by Brobery, B., Hult, J., and Niordson, F., John Wiley and Sons, 1967, pp. 367-372.

17. Neuber, H.: "Notch Stress Theory." Air Force Systems Command Tech. Rpt. No. AFML-TR-65-225, July 1965.

18. Nadai, A.: The Theory of Flow and Fracture of Solids. Vol. I, McGraw-Hill Book Company, Inc., New York, 1950.

19. Budiansky, B., and Mangasarian, O. L.: "Plastic Stress Concentration at a Circular Hole in an Infinite Sheet Subjected to Equal Biaxial Tension." Jour. of Applied Mechanics, vol. 27, 1960, pp. 59-64.

20. Peterson, R. E.: "Fatigue of Metals, Part 3 - Engineering and Design Aspects." Materials Research and Standards, vol. 3, no. 2, February 1963, pp. 122-139.

21. Dolan, T. J.: "Nonlinear Response Under Cyclic Loading Conditions." Proceedings of the Ninth Midwestern Mechanics Conf., August 1965.

22. Manson, S. S., and Hirschberg, M. H.: "Crack Initiation and Propagation in Notched Fatigue Specimens." Proceedings of the First International Conf. on Fracture, vol. 1, 1965, pp. 479-498.

23. Topper, T. H., Wetzel, R. M., and Morrow, J.: "Neuber's Rule Applied to Fatigue of Notched Specimens." Naval Air Engineering Center, Phila., Pa., Rpt. No. NAEC-ASL-1114, June 1967.

24. Wetzel, R. M.: "Smooth Specimen Simulation of Fatigue Behavior of Notches." ASTM Jour. of Materials, vol. 3, no. 3, September 1968, pp. 646-657.

25. Dixon, J. R., and Strannigan, J. S.: "Strain Distributions Around Cracks in Ductile Sheets During Loading and Unloading." Jour. Mech. Engr. Science, vol. 7, no. 3, 1965, pp. 312-317.

26. Dixon, J. R.: "Stress and Strain Distributions Around Cracks in Sheet Material Having Various Work-Hardening Characteristics." International Jour. of Fracture Mechanics, vol. 1, no. 3, 1965, pp. 224-249.

27. Gunn, K.: "Effect of Yielding on the Fatigue Properties of Test Pieces Containing Stress Concentrations." The Aeronautical Quarterly, November 1955, pp. 277-294.

28. Smith, C. R.: "Prediction of Fatigue Failures in Aluminum Alloy Structures." Proc. of SESA, vol. 12, no. 2, 1955, pp. 21-28.

29. Miner, M. A.: "Cumulative Damage in Fatigue." J. Appl. Mech., vol. 12, no. 3, 1945, pp. A-159-A-164.

30. Smith, C. R.: "Linear Strain Theory and the Smith Method For Predicting Fatigue Life of Structures For Spectrum Type Loading." USAF Office of Aerospace Research Report No. ARL 64-55, 1964.

31. Ripp, F., Gomza, A., and Adee, T. C.: "Calculation of Fatigue Life By Grumman Method and Comparison With Test Data." Grumman Aircraft Engr. Corp. Rpt. No. GE-168, February 1959.

32. Neuber, H.: Theory of Notch Stresses; Principles For Exact Stress Calculation. J. W. Edwards, Ann Arbor Michigan, 1946.

33. Illg, W.: "Fatigue Tests on Notched and Unnotched Sheet Specimens of 2024-T3 and 7075-T6 Aluminum Alloys and of SAE 4130 Steel With Special Consideration of the Life Range From 2 to 10,000 Cycles." NACA TN 3866, December 1956.

34. Manson, S. S.: "Interfaces Between Fatigue, Creep, and Fracture." Proceedings of the First International Conf. on Fracture, vol. III, September 1965, pp. 1387-1432.

35. Silverman, B. S., Hooson, R. E., and Saleme, E.: "Fatigue Prediction Methods Based on Strain Cycling." Grumman Aircraft Engr. Corp. Rpt. No. FSR-AD2-01-683, May 1968.

36. McEvily, A. J., Jr., and Illg, W.: "The Rate of Fatigue Crack Propagation in Two Aluminum Alloys." NACA TN 4394, September 1958.

37. Paris, P. C., Gomez, M. P., and Anderson, W. E.: "A Rational Analytical Theory of Fatigue." The Trend in Engineering, vol. 13, no. 1, January 1961, p. 9.

38. Hardrath, H. F., and McEvily, A. J.: "Engineering Aspects of Fatigue Crack Propagation." Proceedings of the Crack Propagation Symposium, vol. II, Cranfield, England, October 1961.

39. Rosenthal, D., and Sines, G.: "Effect of Residual Stress on the Fatigue Strength of Notched Specimens." ASTM Proceedings, vol. 51, 1951, pp. 593-610.

40. Heller, R. A., Seki, M., and Freudenthal, A. M.: "The Effects of Residual Stress on Random Fatigue Life." Proceedings of ASTM, vol. 64, 1964, pp. 516-536.

41. Taira, S., and Murakami, Y.: "Residual Stresses Produced By Plastic Tension in Notched Plate Specimens and Fatigue Strength." Bulletin of JSME, vol. 4, no. 5, 1961, pp. 453-460.

42. Howland, R. C. J.: "On the Stresses in the Neighborhood of a Circular Hole in a Strip Under Tension." Transactions of the Royal Society of London, vol. A229, 1929-1930, pp. 49-86.

43. Dolan, T. J., and Corten, H. T.: "Progressive Damage Due to Repeated Loading." Wright Air Development Center Symposium on Fatigue of Aircraft Structures, WADC TR 59-507, 1959, pp. 598-625.

44. Manson, S. S., Freche, J. C., and Ensign, C. R.: "Application of a Double Linear Damage Rule to Cumulative Fatigue." Fatigue Crack Propagation. ASTM STP 415, 1967, pp. 384-412.

45. Freudenthal, A. M., and Heller, R. A.: "On Stress Interaction in Fatigue and a Cumulative Damage Rule." Journal of the Aerospace Sciences, vol. 26, no. 7, 1959, pp. 431-442.

46. Topper, T. H., and Sandor, B. I.: "Effects of Mean Stress and Prestrain on Fatigue Damage Summation." Univ. of Illinois T. and A.M., Rept. No. 318, August 1968.

47. Head, A. K.: "The Growth of Fatigue Cracks." The Philosophical Magazine, vol. 44, series 7, 1953, p. 925.

48. McEvily, A. J., and Illg, W.: "The Rate of Fatigue Crack Propagation in Two Aluminum Alloys." NACA TN 4394, September 1958.

49. Paris, P. C., Gomez, M. P., and Anderson, W. E.: "A Rational Analytical Theory of Fatigue." The Trend in Engineering, vol. 13, no. 1, January 1961, p. 9.

50. Figge, I. E., and Newman, J. C.: "Fatigue Crack Propagation in Structures With Simulated Rivet Forces." Fatigue Crack Propagation, ASTM STP 415, 1967, pp. 71-93.

51. Bowie, O. L.: "Analysis of an Infinite Plate Containing Radial Cracks Originating From the Boundary of an Internal Circular Hole." Journal of Mathematics and Physics, vol. 35, no. 1, 1956, pp. 60-71.

52. Paris, P. C., and Sih, G. C.: "Stress Analysis of Cracks." Fracture Toughness Testing and Its Applications, ASTM STP 381, 1965, pp. 30-83.

53. Irwin, G. R.: "Analysis of Stresses and Strains Near End of a Crack. Journal of Applied Mechanics." Trans. of ASME, vol. 24, no. 3, 1957, pp. 361-364.

54. Newman, J. C.: "Stress Analysis of Simply and Multiply Connected Regions Containing Cracks By the Method of Boundary Collocation." M. S. Thesis, Virginia Polytechnic Institute, 1969 (in preparation).

55. Muskhelishvili, N. I.: Some Basic Problems of Mathematical Theory of Elasticity. P. Noordhoff, 1953.

56. Erdogan, F.: "On the Stress Distribution in Plates With Colinear Cuts Under Arbitrary Loads." Proc. Fourth U.S. National Congress of Applied Mechanics, 1962, pp. 547-553.

57. Paris, P. C.: A Short Course in Fracture Mechanics. The Boeing Company, March 1960.

58. Sokolnikoff, I. S.: Mathematical Theory of Elasticity. McGraw-Hill Book Co., Inc., 1956.

8. APPENDIX A - DEVELOPMENT OF STRESS EQUATIONS FOR CONCENTRATED FORCES ON A CRACK BOUNDARY

Irwin [53] presented the Westergaard stress function

$$Z_1(z) = \frac{2P_z}{\pi t(z^2 - b^2)}\left[\frac{a^2 - b^2}{z^2 - a^2}\right]^{1/2} \tag{A1}$$

for the problem shown in figure 5.7. The stress components in Cartesian coordinates were written as

$$\left.\begin{aligned} \sigma_{xx} &= \mathrm{Re}Z_1 - y\mathrm{I_m}Z_1' \\ \sigma_{yy} &= \mathrm{Re}Z_1 + y\mathrm{I_m}Z_1' \end{aligned}\right\} \tag{A2}$$

and

$$\tau_{xy} = -y\mathrm{Re}Z_1'$$

For the purpose of calculating stresses along the circle of unit radius equation (A2) was transformed to polar coordinates by

$$\left.\begin{aligned} \sigma_{rr} &= \cos^2\theta\sigma_{xx} + 2\sin\theta\cos\theta\tau_{xy} + \sin^2\theta\sigma_{yy} \\ \text{and} \\ \tau_{r\theta} &= -\sin\theta\cos\theta\sigma_{xx} + (\cos^2\theta - \sin^2\theta)\tau_{xy} + \sin\theta\cos\theta\sigma_{yy} \end{aligned}\right\} \tag{A3}$$

The substitution of equation (A2) into equation (A3) yielded

$$\left.\begin{aligned}\sigma_{rr} &= \left[\mathrm{Re}Z_1 - yI_mZ_1'\right]\cos^2\theta - 2y\mathrm{Re}Z_1' \sin\theta\cos\theta \\ &\quad + \left[\mathrm{Re}Z_1 + yI_mZ_1'\right]\sin^2\theta \\ &\text{and} \\ \tau_{r\theta} &= y\left[2I_mZ_1' \sin\theta\cos\theta - \mathrm{Re}Z_1'(\cos^2\theta - \sin^2\theta)\right]\end{aligned}\right\} \quad (A4)$$

9. APPENDIX B - DEVELOPMENT OF STRESS EQUATIONS FOR BOUNDARY COLLOCATION PROCEDURE

Muskhelishvili [55] expressed stress components in Cartesian coordinates in terms of the stress functions $\phi(z)$ and $\psi(z)$ by the equations

$$\left.\begin{aligned} \sigma_{11} + \sigma_{22} &= 2\left[\phi'(z) + \overline{\phi'(z)}\right] \\ \text{and} \\ \sigma_{22} - \sigma_{11} + 2i\tau_{12} &= 2\left[\bar{z}\phi''(z) + \psi'(z)\right] \end{aligned}\right\} \quad (B1)$$

or with

$$\Phi(z) \equiv \phi'(z), \quad \Psi(z) \equiv \psi'(z) \quad (B2)$$

Muskhelishvili rewrote equations (B1) as

$$\left.\begin{aligned} \sigma_{11} + \sigma_{22} &= 2\left[\Phi(z) + \overline{\Phi(z)}\right] \\ \text{and} \\ \sigma_{22} - \sigma_{11} + 2i\tau_{12} &= 2\left[z\Phi'(z) + \Psi(z)\right] \end{aligned}\right\} \quad (B3)$$

The introduction of $\Omega(z)$ also from [55]

$$\Omega(z) \equiv \overline{\Phi}(z) + z\overline{\Phi}'(z) + \overline{\Psi}(z) \quad (B4)$$

yields

$$\left.\begin{aligned} \sigma_{11} + \sigma_{22} &= 2\left[\Phi(z) + \overline{\Phi(z)}\right] \\ \text{and} \\ \sigma_{22} - \sigma_{11} + 2i\tau_{12} &= 2\left[(\bar{z} - z)\Phi'(z) - \Phi(z) + \overline{\Omega}(z)\right] \end{aligned}\right\} \quad (B5)$$

In cylindrical coordinates equations (B5) become

$$\left.\begin{aligned} \sigma_{rr} + \sigma_{\theta\theta} &= 2\left[\Phi(z) + \overline{\Phi(z)}\right] \\ \text{and} \\ \sigma_{\theta\theta} - \sigma_{rr} + 2i\tau_{r\theta} &= 2\left[(\bar{z} - z)\Phi'(z) - \Phi(z) + \overline{\Omega}(z)\right]e^{2i\theta} \end{aligned}\right\} \quad (B6)$$

Subtracting equations (B6) yields

$$\sigma_{rr} - i\tau_{r\theta} = \Phi(z) + \overline{\Phi(z)} - \left[(\bar{z} - z)\Phi'(z) - \Phi(z) + \overline{\Omega}(z)\right]e^{2i\theta} \quad (B7)$$

Newman presented expressions for $\Phi(z)$ and $\Omega(z)$ in reference [54] following a general form developed by Erdogan [56] for a plate containing a crack. From [54]

$$\left.\begin{aligned} \Phi(z) &= \sum_{n=1}^{M}\left\{\frac{A_n}{z^{2n-1}\sqrt{z^2 - a^2}} + \frac{B_n}{z^{2n}}\right\} \\ \text{and} \\ \Omega(z) &= \sum_{n=1}^{M}\left\{\frac{A_n}{z^{2n-1}\sqrt{z^2 - a^2}} - \frac{B_n}{z^{2n}}\right\} \end{aligned}\right\} \quad (B8)$$

where a is the half crack length and A_n and B_n are arbitrary constants. For the present study these Muskhelishvili stress functions were substituted into equations (B7) and real and imaginary parts were separated to obtain expressions for σ_{rr} and $\tau_{r\theta}$.

Equations (B8) were rewritten in exponential form using a change of variables.

$$\left.\begin{aligned} z &= re^{i\theta} \\ z - a &= r_1 e^{i\theta_1} \\ z + a &= r_2 e^{i\theta_2} \end{aligned}\right\} \tag{B9}$$

as illustrated in figure B1. From equations (B8) and equations (B9) one obtains

$$\Phi(z) = \sum_{n=1}^{M} \frac{A_n \exp\left\{-i\left[(2n-1)\theta + \frac{\theta_1}{2} + \frac{\theta_2}{2}\right]\right\}}{r^{2n-1}\sqrt{r_1 r_2}} + \frac{B_n e^{-2in\theta}}{r^{2n}} \tag{B10}$$

Differentiating $\Phi(z)$ from equations (B8) and substituting from equations (B9) yields

$$\Phi'(z) = \sum_{n=1}^{M}\left[\frac{A_n(-2n+1)}{r^{2n}\sqrt{r_1 r_2}} \exp\left\{-i\left(2n\theta + \frac{\theta_1}{2} + \frac{\theta_2}{2}\right)\right\}\right.$$

$$\left. - \frac{A_n \exp\left\{-i\left[(2n-2)\theta + \frac{3\theta_1}{2} + \frac{3\theta_2}{2}\right]\right\}}{r^{2n-2}\sqrt{(r_1 r_2)^3}} - \frac{2nB_n}{r^{2n+1}} \exp\left\{-i(2n+1)\theta\right\}\right] \tag{B11}$$

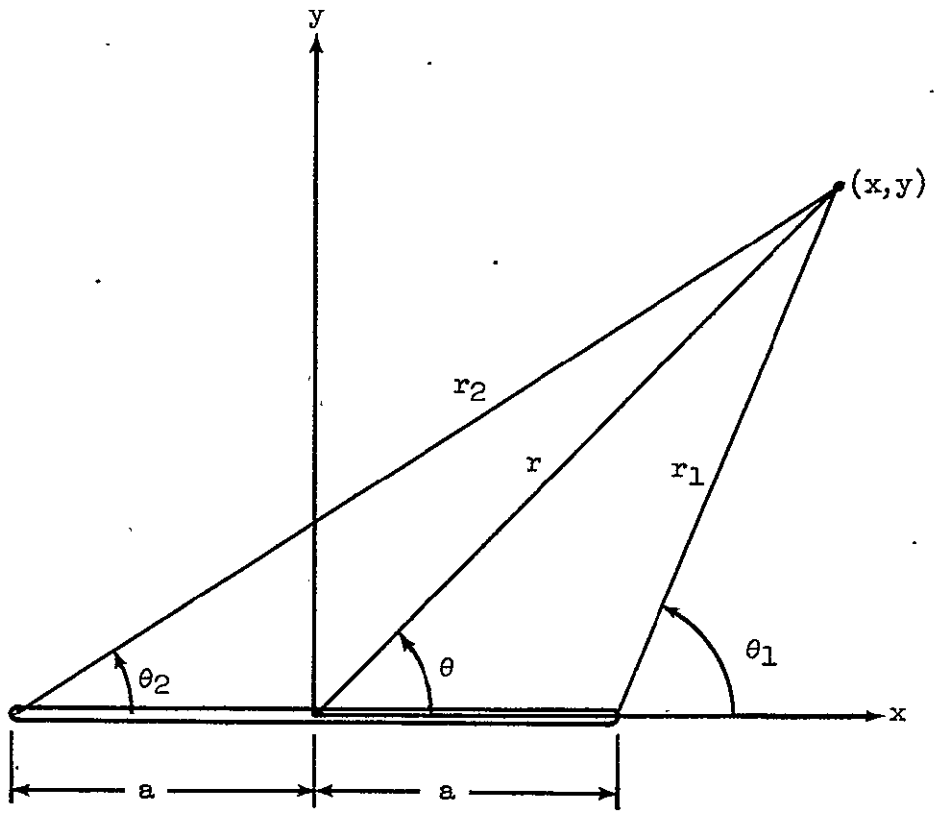

Figure B1 – Illustration of coordinate system referenced to crack tips.

The conjugate $\overline{\Phi(z)}$ is

$$\overline{\Phi(z)} = \sum_{n=1}^{M}\left[\frac{A_n}{r^{2n-1}\sqrt{r_1 r_2}} \exp\left\{i\left[(2n-1)\theta + \frac{\theta_1}{2} + \frac{\theta_2}{2}\right]\right\} + \frac{B_n e^{2in\theta}}{r^{2n}}\right] \tag{B12}$$

and

$$\overline{\Omega}(z) = \Omega(z) \tag{B13}$$

By substitution from equations (B8), (B10), (B11), (B12), and (B13) into equation (B7) with the introduction of β_1 and β_2

$$\left.\begin{aligned} \beta_1 &\equiv \frac{\theta_1}{2} + \frac{\theta_2}{2} \\ \text{and} \\ \beta_2 &\equiv \frac{3\theta_1}{2} + \frac{3\theta_2}{2} \end{aligned}\right\} \tag{B14}$$

one obtains

$$\sigma_{rr} - i\tau_{r\theta} = \sum_{n=1}^{M} A_n \left\{ \frac{1}{r^{2n-1}\sqrt{r_1 r_2}} \left[\exp\left\{-i\left[(2n-1)\theta + \beta_1\right]\right\} \right.\right.$$

$$\left. + \exp\left\{i\left[(2n-1)\theta + \beta_1\right]\right\} \right] - \frac{2iy(2n-1)}{r^{2n}\sqrt{r_1 r_2}} \exp\left\{-i\left[(2n-2)\theta + \beta_1\right]\right\}$$

$$\left. - \frac{2iy}{r^{2n-2}\sqrt{(r_1 r_2)^3}} \exp\left\{-i\left[(2n-4)\theta + \beta_2\right]\right\} \right\}$$

$$+ \sum_{n=1}^{M} B_n \left\{ \frac{1}{r^{2n}}\left[e^{-2in\theta} + e^{2in\theta}\right] - \frac{4iny}{r^{2n+1}} \exp\left\{-i(2n-1)\theta\right\} \right.$$

$$\left. + \frac{2}{r^{2n}} \exp\left\{-i(2n-2)\theta\right\} \right\} \qquad \text{(B15)}$$

Separation of real and imaginary parts of equation (B15) leads to the following trigometric forms for σ_{rr} and $\tau_{r\theta}$.

$$\sigma_{rr} = \sum_{n=1}^{M} \left\{ 2A_n \left[\frac{1}{r^{2n-1}\sqrt{r_1 r_2}} \cos\left[(2n-1) + \beta_1\right] - \frac{(2n-1)y}{r^{2n}\sqrt{r_1 r_2}} \sin\left[(2n-2) + \beta_1\right] \right.\right.$$

$$\left. - \frac{y}{r^{2n-2}\sqrt{(r_1 r_2)^3}} \sin\left[(2n-4)\theta + \beta_2\right] \right] + 2B_n \left[\frac{1}{r^{2n}} \cos 2n\theta \right.$$

$$\left. \left. - \frac{2ny}{r^{2n+1}} \sin\,(2n-1)\theta + \frac{1}{r^{2n}} \cos(2n-2)\theta \right] \right\} \qquad \text{(B16)}$$

and

$$\tau_{r\theta} = \sum_{n=1}^{M} \left\{ 2A_n \left[\frac{(2n - 1)y}{r^{2n}\sqrt{r_1 r_2}} \cos\left[(2n - 2)\theta + \beta_1\right] \right.\right.$$

$$\left. + \frac{y}{r^{2n-2}\sqrt{(r_1 r_2)^3}} \cos\left[(2n - 4)\theta + \beta_2\right] \right] + 2B_n \left[\frac{2ny}{r^{2n+1}} \cos(2n - 1)\theta \right.$$

$$\left.\left. + \frac{1}{r^{2n}} \sin(2n - 2)\theta \right] \right\} \qquad \text{(B17)}$$

Equations (B16) and (B17) are the expressions for σ_{rr} and $\tau_{r\theta}$ used in the boundary collocation procedure.

10. APPENDIX C - CALCULATION OF CONCENTRATED FORCE SYSTEMS SIMULATING STRESS DISTRIBUTIONS ON TRANSVERSE AXIS OF SPECIMEN

10.1 Elastic Distribution for S = 20 ksi

The elastic stress distribution for the specimen configuration used in this study was nearly identical to that for an infinite sheet as illustrated previously in figure 3.2. Therefore, for convenience the elastic solution [58]

$$\sigma_{\theta\theta_o} = \frac{\sigma_g}{2}\left\{1 + \left(\frac{\rho}{r}\right)^2 + \left[1 + 3\left(\frac{\rho}{r}\right)^4 \cos 2\theta\right]\right\} \qquad (C1)$$

for an infinite sheet with a circular hole of radius ρ was used. Equation (C1) was evaluated for $\sigma_g = 20$ ksi and $\theta = 0$, and $\sigma_{\theta\theta}$ was plotted for the full width of the specimen. As typically illustrated in figure C1, this stress distribution was divided into discrete segments. The average stress $(\sigma_{\theta\theta})_i$ for each segment was used to calculate a statically equivalent concentrated force P_i from

$$P_i = \Delta b t (\sigma_{\theta\theta})_i \qquad (C2)$$

where t is specimen thickness and $\Delta b = 0.0025$ inch. By this procedure a system of concentrated forces was developed to approximate the elastic stress distribution for S = 20 ksi.

10.2 Elastoplastic Distribution For Beneficial Prior Loading

The prior loading produced localized plasticity as previously illustrated in figure 4.4. The procedure used to calculate the stress

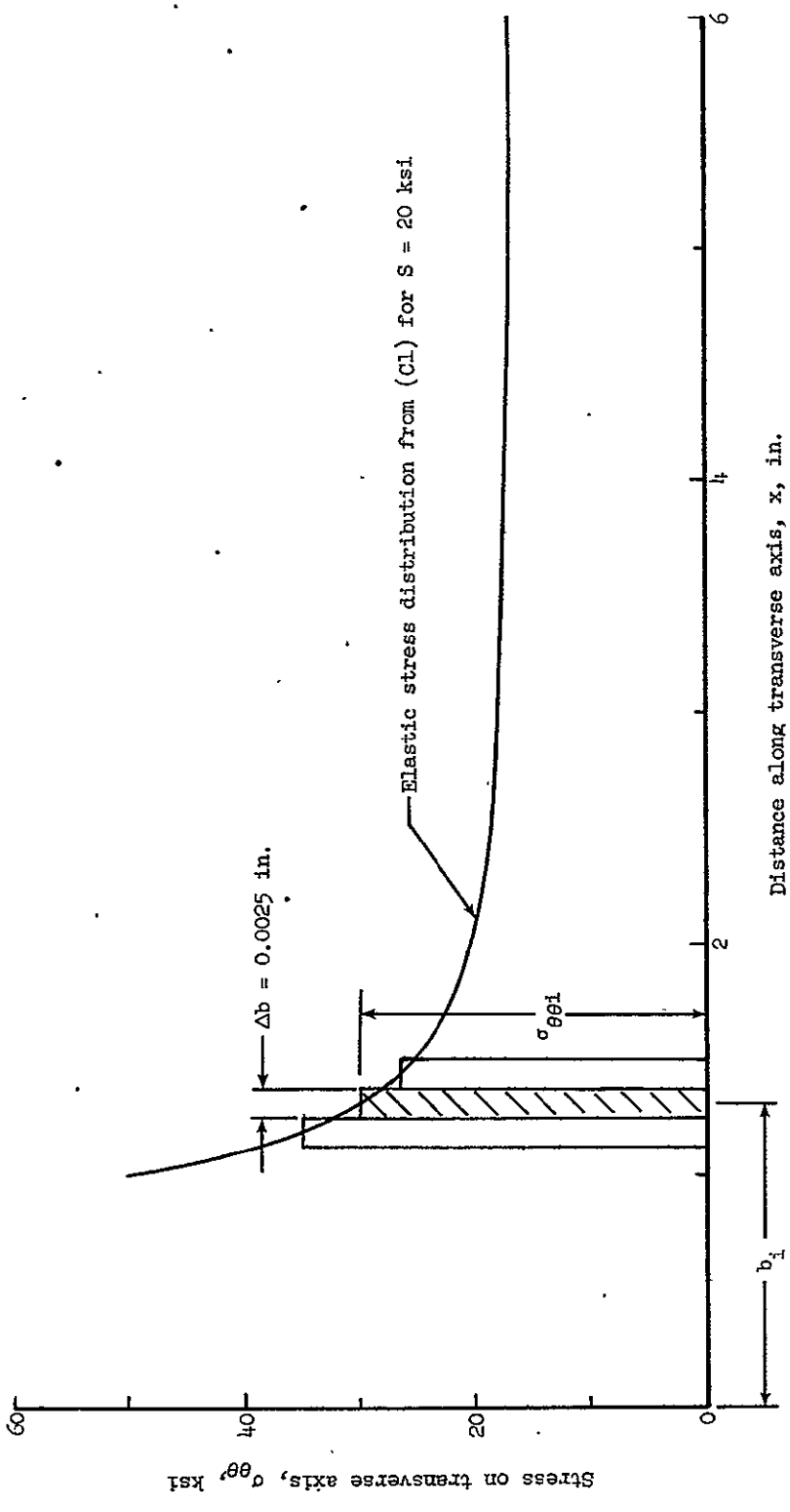

Figure C1 -- Typical discretization of stress distribution on transverse axis of specimen.

distribution in figure 4.4 is described in this section. The elastic stresses corresponding to the prior loading stress level (S = 40 ksi) were determined from equation (C1) and

$$\sigma_{rr_o} = \frac{\sigma_g}{2}\left\{1 - \left(\frac{\rho}{r}\right)^2 - \left[1 - 4\left(\frac{\rho}{r}\right)^2 + 3\left(\frac{\rho}{r}\right)^4\right]\cos 2\theta\right\} \tag{C3}$$

along the transverse axis. The effective stress σ_{e_o} corresponding to this elastic solution was found from

$$\sigma_{eo} = \left[\sigma_{rr_o}^2 - \sigma_{rr_o}\sigma_{\theta\theta_o} + \sigma_{\theta\theta}^2\right]^{1/2} \tag{C4}$$

An approximate elastoplastic analysis was based on these elastic stresses using the approach presented by Dixon and Strannigan [25]. From equation (11) in Chapter 2 an expression for $\sigma_{\theta\theta}$ was written as

$$\sigma_{\theta\theta} = \sigma_{\theta\theta_o}\sqrt{\frac{E_s}{E}} \tag{C5}$$

where E_s is the secant modulus from the uniaxial stress-strain curve corresponding to the effective stress σ_e. This effective stress σ_e was found from

$$\sigma_e = \sigma_{eo}\sqrt{\frac{E_s}{E}} \tag{C6}$$

The elastic effective stress σ_{eo} was found from equation (C4), but because E_s depended on σ_e, equation (C6) could not be solved directly for the E_s required in equation (C5). A graphical procedure

was used to obtain E_s, as illustrated in figure C2. The curve of σ against $\sqrt{E_s/E}$ was constructed from the uniaxial stress-strain curve for 2024-T3, and equation (C6) was plotted for a given σ_{eo}. The intersection of these two curves represents a simultaneous graphical solution for equation (C6) and the stress-strain relationship. This value of $\sqrt{E_s/E}$ and $\sigma_{\theta\theta_o}$, corresponding to the σ_{eo} used in figure C2, were substituted into equation (C5) to obtain $\sigma_{\theta\theta}$. To account for the cyclic strain hardening displayed by 2024-T3 (see for example fig. 3.20), the cyclic stress-strain curve from figure 3.16 was used in this graphical procedure.

The above procedure was repeatedly applied to construct the plastic portion of the stress distribution in figure C3 for S = 40 ksi. Because plasticity was accounted for by attenuating elastic stresses this procedure made no correction to the elastic portion of the elastoplastic stress distribution. To satisfy equilibrium the elastic portion of this stress distribution must be altered to account for the decrease in area under the curve caused by the attenuation of stresses due to plasticity. For the present analysis the elastic portion of the curve was raised uniformly until the increase in area under this part of the curve was approximately equal to the above mentioned decrease in area. This minor alteration to the stress distribution is shown in figure C3.

The residual stress distribution in figure C3 was found by subtracting stress range values corresponding to elastic unloading from the elastoplastic stress distribution, and by applying the above

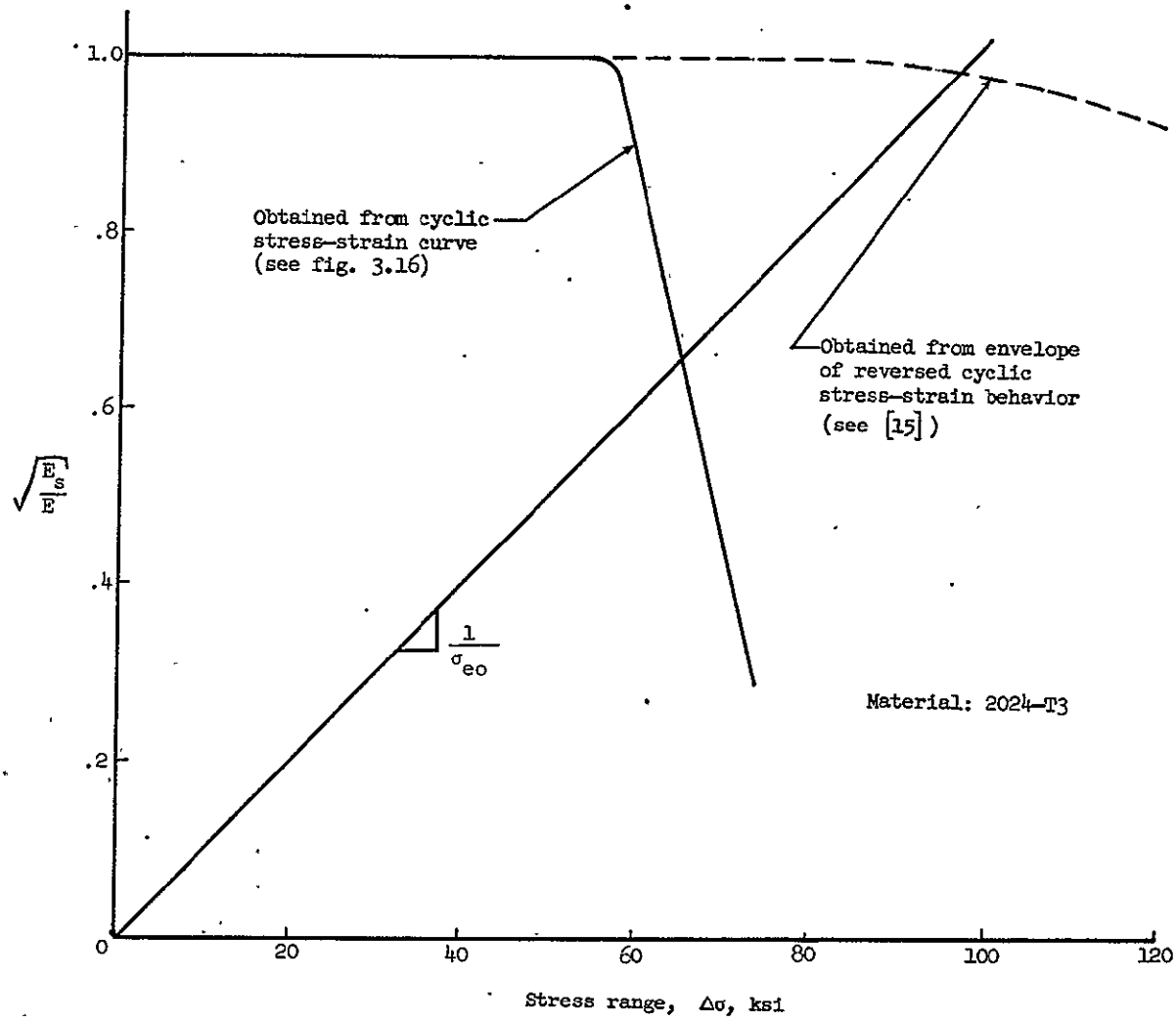

Figure C2 – Graphical procedure for obtaining $\sqrt{E_s/E}$.

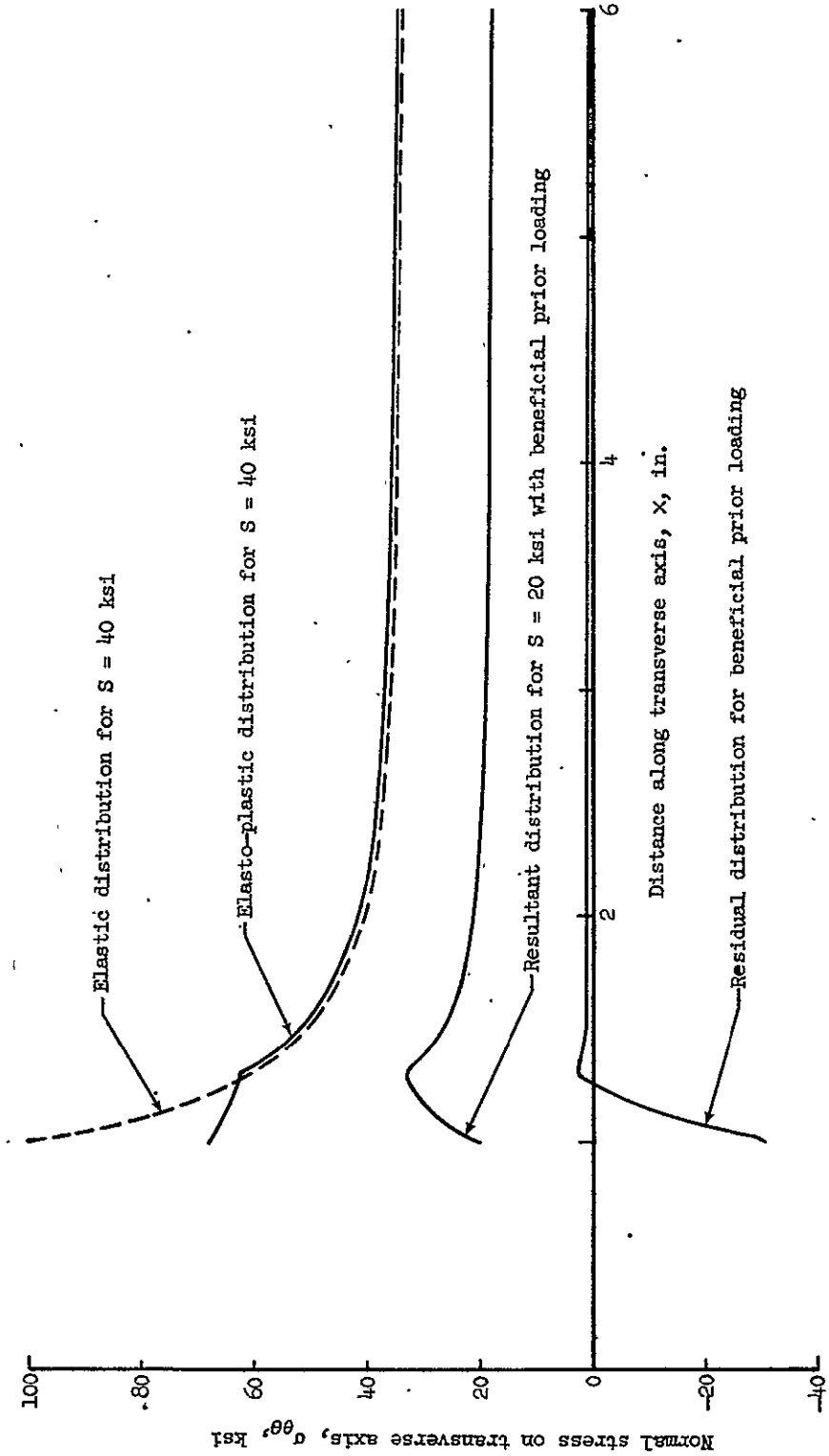

Figure C3 – Stress distribution on transverse axis for beneficial prior loading.

procedure to make a small correction for reversed yielding. The resultant stress distribution (for application of S = 20 ksi, following the unloading from S = 40 ksi) was obtained by adding elastic stress range values for S = 20 ksi to the residual stress distribution.

The system of concentrated forces simulating this stress distribution was calculated using equation (C2) and the procedure in figure C1.

11. VITA

The author was born in [redacted], on [redacted]. He received a B.S. degree in Mechanical Engineering from Virginia Polytechnic Institute in 1961. The author was employed by Bell Telephone Laboratories in Burlington, North Carolina, during 1961 and 1963. Also during this time he attended North Carolina State University at Raleigh, where he received a M.S. degree in Engineering Mechanics in 1963. Since 1963 the author has been employed by the Langley Research Center of the National Aeronautics and Space Administration. During this time he has been engaged in research in the area of structural fatigue.

John H. Crews, Jr.